Department of Physics
Indian Institute of Technology Guwahati
Ph.D. Thesis

First principles study of phase stability, electronic structure and magnetism in Mn_2YZ systems with multiple functionalities

Ashis Kundu

Supervisor: Prof. Subhradip Ghosh
January, 2018.

First principles study of phase stability, electronic structure and magnetism in Mn$_2$YZ systems with multiple functionalities

A thesis submitted by

Ashis Kundu

to

Indian Institute of Technology Guwahati
in partial fulfillment of the requirements
for the award of the degree of
Doctor of Philosophy in Physics

Department of Physics
Indian Institute of Technology Guwahati
Guwahati - 781039, Assam, India

Statement

The work contained in the thesis entitled "*First principles study of phase stability, electronic structure and magnetism in* Mn_2YZ *systems with multiple functionalities*" has been carried out at the Department of Physics, Indian Institute of Technology Guwahati, India by me under the supervision of Prof. Subhradip Ghosh. The material of this thesis has not been has been submitted elsewhere for any other degree. Works presented in the thesis are all my own unless referenced to the contrary in the text.

(Ashis Kundu) Date:
Roll No. - 126121009
Department of Physics
Indian Institute of Technology Guwahati
Guwahati - 781039, India

Disclamer

The bibliography included in this thesis is, by no means complete but contains the ones which are consulted thoroughly by me. I apologize for inadvertently missing out some of the research papers, review articles and other scientific documents pertaining to the focus of this thesis which should also have been cited. For illustration purpose some of the figures in this thesis are taken from other sources and properly cited.

Certificate

It is certified that the work contained in the thesis entitled "*First principles study of phase stability, electronic structure and magnetism in* Mn_2YZ *systems with multiple functionalities*" by Mr. Ashis Kundu, a Ph.D. student of the Department of Physics, Indian Institute of Technology Guwahati is carried out under my supervision and has not been submitted elsewhere for the award of any other degree.

(Prof. Subhradip Ghosh) Date:
Department of Physics
Indian Institute of Technology Guwahati
Guwahati - 781039, India

Dedicated to

my parents and my sister and brother

Acknowledgement

First of all, I express my sincere gratitude to my thesis supervisor Prof. Subhradip Ghosh for his continuous support during my Ph.D programme. I have been always motivated by his expert supervision and dedication for work. I am also thankful to him for giving me the opportunity to be involved in different types of problems and collaborations that helped me a lot to increase my experience and knowledge.

I would like to thank Dr. Biplab Sanyal, one of my collaborators and grateful to him for hosting a visit to Uppsala University. I would also like to thank my other collaborators Dr. Markus E. Gruner and Prof. A Srinivasan. I have learned many theoretical and experimental aspects of the subject from them.

I would like to acknowledge my doctoral committee members - Prof. Saurabh Basu, Prof. Perumal Alagarsamy and Dr. Atanu Banerjee for their useful suggestions during the yearly assessments of my research work. I thank to all HODs(Prof. Saurabh Basu and Prof. Poulose Poulose) during my Ph.D study. I would like to thank all the technical assistants, academic and non-academic staff of the department who helped me in various ways during my research period. I specially thank Basab-da for his support in different computer related issues. I am thankful to SINC-HPC2N, Sweden and CDAC, Pune, India for the allocation of supercomputing time. I am also thankful to Param Ishan, IIT Guwahati for the supercomputer facility. I thank the department of Physics IIT Guwahati, India for allowing me to utilize Newton cluster, funded under the FIST programme by DST, India.

I would like to thank my senior group members, Dr. Biswanath Dutta, Dr. Souvik Paul and Dr. Debashish Das. My special thanks go to Souvik-da and Debashishs-da for their continuous support to make me familiar with different electronic structure packages. I would also like to thank my colleague Srikrishna Ghosh and Sheuly Ghosh with whom I have shared my research experiences.

I am fortunate enough to have a great friend circle, seniors and juniors who stay very close to my heart. Among seniors I would like to thank Biswajit-da, Himangsu-da, Tapas-da, Bappaditya-da, Kartik-da, Arnab-da, Ramesh-da. I am extremely lucky to have my friends like Sourav, Abhijit, Koushik, Ramiz, Kallol, Sudin-da, and Anabil-da. I had lot of great moments with them which I will never forget. I get a lot of inspiration and motivation from Himangsu-da and Tapas-da for working hard and independently. My special thanks goes to Sourav who brought my interest in the field of computational physics. I would like to thank my batchmates Rahul, Shibananda, Venkanna, Bibhuti, Ram Kumar, Prahlad and my juniors Noor, Sanjib, Srimoy, Krisnanjan, Basabendu and Sayandeep. I would also like to thank Sunando-da and Ashmita-di. I would like to thank Kartik and Atanu for having lot of useful discussions related to my research.

I would like to thank my elder brother Pintu-da for motivating me to study science after class-X and constant support during tough times. I would like to thank my uncle Ananta Kundu for his financial support during class-XII. My special thanks goes to my uncle Swapan Betal for his support and motivation in many ways. I would also like to thank my grandfather Samir Kundu and my uncle cum teacher Sanat Kundu. I am also thankful to late Shiv Sankar Kundu.

Most importantly, I would like to thank my family, my parents and my brother and sister for their unconditional love, support, and sacrifices for me. I owe everything to them.

Abstract

Heusler compounds are a remarkable class of intermetallics which possess many functionalities including magnetic shape memory effect(MSME), half-metallicity, magnetocaloric effect and magnetoresistance with many possible applications. In the family of Heusler compounds, Mn_2YZ compounds have attracted considerable attention due to their interesting structure-magnetism relations leading to applications in magnetomechanical devices, magnetic sensors, spintronics, and energy technology. In this thesis, we investigate the phase stability, structural, electronic, elastic and magnetic properties of several Mn_2YZ systems from first-principles electronic structure calculations. The primary motivation is to explore and understand the possibility of martensitic phase transformation leading to magnetic shape memory effect and its origin in several pristine and substituted Mn_2YZ systems. In this thesis we investigate Mn_2NiGa, Fe and Co substituted Mn_2NiGa, Mn_2FeGa and $Mn_2Ni_{1+x}Sn_{1-x}$ compounds. The choice of the systems is motivated by the interesting experimental results obtained in each case. A complete picture of martensitic phases and the path of phase transformation in magnetic shape memory alloy Mn_2NiGa is explained from the electronic structure, phonon dispersion, and electronic susceptibility. The effect of Fe and Co substitution on the martensitic phase transformation, mechanical stability, magnetization and the magnetic ordering temperature of Mn_2NiGa is investigated extensively, leading to establishing several important differences in physical properties with well known magnetic shape memory system Ni_2MnGa and the promise of obtaining multiple functionalities in the same system depending upon the degree of substitution. The origin of different structural phases and complex magnetic orders resulting out of it in Mn_2FeGa is investigated leading to the knowledge of the ground state spin structures in each structural phase which was hitherto unknown. Finally, the effect of compositional changes along with different atomic and magnetic ordering on martensitic transformations is investigated for Ni-excess, Sn-deficient Mn_2NiSn which have experimentally observed to exhibit magnetic shape memory effect. In a nutshell, the results presented in this thesis provide us with significant insights into the fundamentals of Mn_2YZ systems and demonstrate how functionalities can be manipulated in these systems by changing compositions and/or by substitution.

Contents

Acknowledgement xi

Abstract xii

1 Introduction 1

1.1 Martensitic transformation . . . 2
1.2 Magnetic shape memory effect(MSME) . . . 4
1.3 Spintronics . . . 6
1.4 Exchange bias . . . 8
1.5 Mn_2YZ systems: Experimental and theoretical background . . . 10
1.6 The importances of first-principles electronic structure calculations towards inquiring into material properties . . . 13
1.7 Outline of the thesis . . . 14

2 Methodology 19

2.1 The many-body Hamiltonian . . . 19
2.2 The Born-Oppenheimer approximation . . . 20
2.3 Density Functional Theory (DFT) . . . 21
2.4 Pseudopotential method . . . 23
  2.4.1 Norm-Conserving Pseudopotentials (NCPP) . . . 24
  2.4.2 Ultrasoft Pseudopotentials (USPP) . . . 24
2.5 Projector Augmented Wave (PAW) method . . . 25
2.6 Korringa, Kohn and Rostoker (KKR) Green's Function method . . . 27
2.7 Coherent Potential Approximation (CPA) . . . 30
2.8 Calculation of elastic moduli . . . 32
  2.8.1 Bulk Modulus . . . 32
  2.8.2 Elastic Constants . . . 32
    2.8.2.1 Elastic moduli in a cubic lattice . . . 33

2.9 Calculation of the magnetic exchange interactions and the magnetic transition temperatures . . . 35
  2.9.1 The magnetic exchange interactions (J_{ij}) . . . 35
  2.9.2 The Curie temperature (T_c) . . . 36
    2.9.2.1 Mean field approximation (MFA) . . . 36
    2.9.2.2 Monte Calro simulation (MCS) . . . 37
2.10 Calculation of phonon dispersion relations . . . 38
2.11 Summary . . . 40

3 Investigation of the modulated martensites in Mn_2NiGa 41
3.1 Introduction . . . 41
3.2 Computational Details . . . 42
3.3 Results and Discussions . . . 43
  3.3.1 Structural properties of cubic, non-modulated, and different modulated phases . . . 43
  3.3.2 Energetics of the modulated structures . . . 49
  3.3.3 Electronic structures of the modulated phases . . . 52
  3.3.4 Phonon instability, Fermi Surface Nesting and Generalised Susceptibility . . . 55
3.4 Conclusions . . . 62

4 Effect of Fe and Co substitution on the martensitic stability and the elastic, electronic, and magnetic properties of Mn_2NiGa 65
4.1 Introduction . . . 65
4.2 Computational Methods . . . 68
4.3 Results and Discussions . . . 69
  4.3.1 Site preferences, stability and structural parameters . . . 69
  4.3.2 Martensitic phase transformation . . . 74
  4.3.3 Elastic properties . . . 77
  4.3.4 Electronic structure . . . 81
  4.3.5 Total and atomic magnetic moments . . . 85
  4.3.6 Magnetic exchange interactions and Curie temperature . . . 88
4.4 Conclusions . . . 92

5 Structural phase stability and magnetic order in various structural phases of Mn_2FeGa 97
5.1 Introduction . . . 97

5.2 Calculational details . . . 99
5.3 Results and Discussions . . . 100
5.3.1 Structural parameters and magnetic structures in various crystallographic phases . . . 100
5.3.2 Stabilities of various phases: analysis from energetics, electronic structure and elastic constants . . . 107
5.3.3 Magnetic exchange interactions . . . 112
5.4 Conclusions . . . 115

6 Site occupancy, composition and magnetic structure dependencies of martensitic transformation in $Mn_2Ni_{1+x}Sn_{1-x}$ 117
6.1 Introduction . . . 117
6.2 Computational Methods . . . 119
6.3 Results and Discussions . . . 120
6.4 Conclusions . . . 129

7 Conclusions and scopes for future work 131
7.1 Conclusions . . . 131
7.2 Scopes for future work . . . 134

Bibliography 135

List of publications 147

Chapter 1

Introduction

Development of materials with functional properties is very crucial in the modern era. Much effort is currently devoted to the exploration of functional materials from among different class of materials such as metals, semiconductors, ceramics, polymers, and composites. Among different classes, the metals are known for their high electrical and thermal conductivity along with high strength and plasticity. The functional materials among metals are of great interest because one can realize adjustable and optimisable application-specific properties upon variations in external stimuli, such as stress, temperature, electric and magnetic field in them. Among the metallic systems, the magnetic materials received a considerable attention after the discovery of new and novel functionalities like spintronics applications, magnetic shape memory applications, and magnetocaloric applications. These functionalities driven by magnetism have gained currency due to the fact that the response of the spin degrees of freedom is much faster than the charge degrees of freedom, and hence are more desirable in device applications. Functionalities of these devices are further boosted up if the material exhibits more than one such properties.

Functionalities like magnetic field assisted shape memory effect, half-metallicity and exchange bias leading to various spintronics applications have been in the forefront of technological importances of magnetic materials in recent days. The coupling between structural phases, magnetic phases, the atomic ordering and the chemical properties of elements is the driving force behind such fascinating properties. In this thesis, we present materials which undergo structural phase transformations which are often coupled with their magnetic structures. Majority of the materials presented here fall into the category of magnetic shape memory alloys. Large spin polarizations making them useful as spintronics materials are found in some cases. The competing magnetic interactions influencing the phase stability are found in some others. In the next few subsections we briefly describe the phenomena associated with these followed by the importances of the materials chosen for the thesis, and the outline of the thesis.

1.1 Martensitic transformation

Martensitic transformation (MT) is a first order solid-solid phase transition with displacive nature (without atomic diffusion) achieved by a homogeneous lattice deformation, leading to a new crystal structure. The term "martensite" is named in the honour of the German metallographer A. Martens [1]. Initially, the term was used to describe the hard microstructure of quenched steels [2]. But over the years, it has been gradually clarified and extended to other alloys for better representation of the microstructures [2]. The martensitic transformations are diffusionless and often associated with phonon anomalies in the parent phase and related precursor phenomena. Sometimes, the martensitic transformation is called a shear or displacive transformation. Due to the diffusionless character of the martensitic transformation, the martensites can form at very low temperatures, where diffusion, even of interstitial atoms, is not conceivable over the time period of the experiment. The temperature at which the martensites start to form, in a material, is known as the martensitic-start temperature (M_s). Subsequently, the high-temperature parent phase, known as the austenite phase, becomes mechanically unstable. When the parent phase completely transforms to the martensite phase, the corresponding temperature is called the martensitic-finish temperature (M_f).

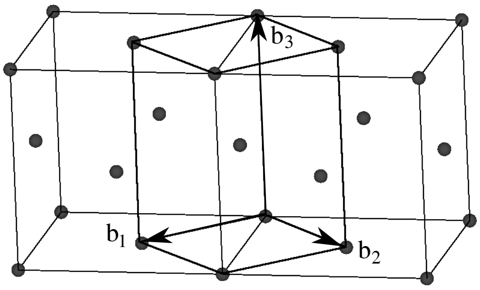

Figure 1.1: Relationship between fcc and bct cells in the austenite phase

Crystallographically the martensitic transformation is related to two important things: (1) the presence of invariant plane in the austenitic phase and (2) the presence of a habit plane with specific (Kurdjumov-Sachs) orientation relationships [3].

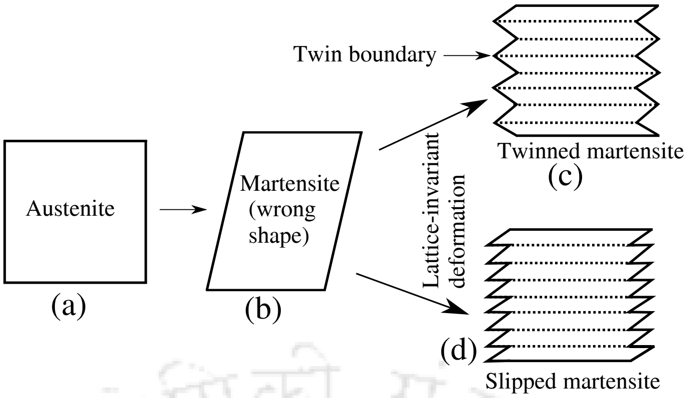

Figure 1.2: Schematic representation of the theory of martensite crystallography; (a) Austenite structure, (b) Martensite structure after Bain strain. This is a "wrong" martensite structure which is never observed in experiment, (c) Twinned, (d) Slipped martensite with correct structure and correct microscopic shape after lattice invariant deformation.

In 1924, Bain proposed the mechanism of structural transformation in iron from fcc to bcc phase which can represent all the martensitic transformations, as shown in Fig. 1.1 [4]. This transformation is a simple homogeneous deformation of the crystal structure. It is also easy to see from Fig. 1.1, that the body centred tetragonal(bct) cell of austenite can be deformed to produce the required bcc cell. Thus, the Bain strain consists of a contraction along the z axis and identical expansion along the x and y axes. In the Bain strain mechanism, the orientational relationships between the parent and the product lattices are

$$[001]_{fcc} \mid\mid [001]_{bcc}, \quad [1\bar{1}0]_{fcc} \mid\mid [100]_{bcc}, \quad [110]_{fcc} \mid\mid [010]_{bcc}$$

but the experimentally observed orientational relationships are irrational, e.g., close to the Kurdjumov-Sachs orientation:

$$\left\{111\right\}_{fcc} \mid\mid \left\{011\right\}_{bcc}, \quad \left\langle 10\bar{1}\right\rangle_{fcc} \mid\mid \left\langle 11\bar{1}\right\rangle_{bcc}$$

So, the Bain strain alone is not sufficient to explain the presence of an invariant plane as it gives a "wrong shaped" martensite as shown in Fig. 1.2 (b). Hence, the theory of martensite crystallography needs Bain strain in combination with certain shears and lattice rotations to explain the observed invariant planes. In order to incorporate the shear, the martensite either slips or undergoes a transformation to

---

The Martensitic transformation is described in H. K. D. H. Bhadeshia, *Martensite in steels*, http://www.msm.cam.ac.uk/phase- trans/2000/C9/lectures45.pdf a twinned structure as shown in 1.2 (c) and (d). Crystal twinning occurs when two separate crystals share some of the same crystal lattice points in a symmetrical manner. The result is an inter-growth of two crystals in a variety of specific configurations separated by a twin boundary. The atoms residing on the boundary are connected with the same number of bonds in both directions of the twinned crystals. The important features of the twin boundary planes are that they are very low in energy and quite mobile; therefore, the relative stability of the martensite phase is not strongly affected by the number or location of these boundaries. The most important difference between slip and twinning is that the former requires the breaking of atomic bonds, while all bonds remain intact in the twinned structure. In fact, under applied stress, the twin boundaries can easily move to produce a deformed shape and the procedure is called detwinning. Although, the Bain strain generates a wrong crystal structure, the combined effect of Bain strain and the lattice invariant shear converts the macroscopic strain into shear and thus, produces the correct martensite shape [5].

1.2 Magnetic shape memory effect(MSME)

The shape memory effect describes restoring the original shape of an elastically deformed sample when heated. This phenomenon is a result of structural phase change, known as thermoelastic martensitic transformation [6]. The very first step towards the discovery of shape memory effect (SME) came off in 1930 [7]. In 1932, A Ölander discovered the pseudoelastic behaviour of Cu-Au alloys [8]. Later, in 1938, Greninger and Mooradian observed a displacive and diffusionless phase transformation from high-temperature phase to low-temperature phase in Cu-Zn alloys [9, 10]. Shape memory effect was first observed for Au-Cd alloys in 1951 [11]. However, the first breakthrough towards engineering applications occurred when Buehler and co-workers discovered the shape memory effect in an equiatomic alloy of Nickel and Titanium in the early 1960s at U.S. Naval Ordance Laboratory [12, 13]. Following this discovery, the name NiTiNOL(Nickel Titanium Naval Ordance Laboratory) was proposed for this new Ni-Ti alloys in the honour of Naval Ordance Laboratory, U.S. The discovery of NiTiNOL spearheaded the research interest into shape memory alloys(SMAs). The use of NiTiNOL was fascinating due to its special functional properties, which was completely new to the field of metal alloys. So the effect of heat-treatments, compositions and microstructures was widely investigated in Ni-Ti and related alloys and understanding of the system begun during this period [14].

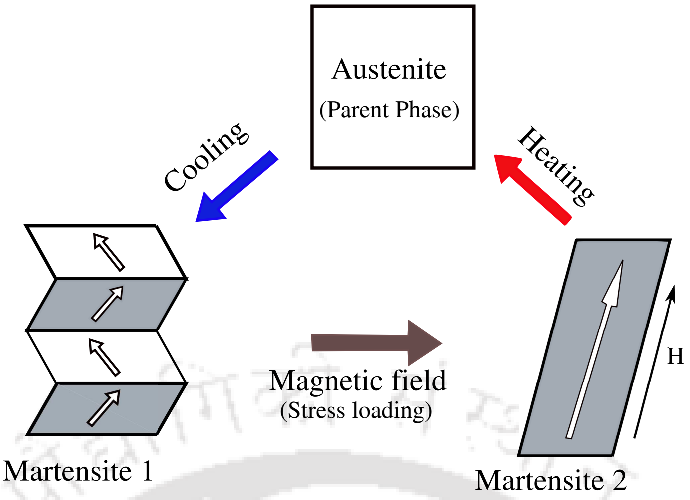

Figure 1.3: A schematic representation of variant conversion in shape memory alloys

Today, these Ni-Ti based alloys are widely used shape memory and superelastic alloys combining shape memory and superelastic effect for many superior engineering properties. Many other Copper based alloys like Cu-Zn-Al and Cu-Ni-Al are commercially available but these alloys are less stable and more brittle than Ni-Ti [15]. There are many applications of these alloys with temperature-pressure controlled shape memory effect. However, in many cases, the application is hindered due to the slow response of shape memory effect with temperature and pressure. Hence it is desirable to control the shape memory effect by other means.

Recently, a new type of material has been found which shows shape memory property along with ferromagnetism [16, 17]. These materials are promising and have vastly increased the range of applications. A unique feature of these materials is that the magnetic field can influence the martensitic transformation and thus the possibility of controlling the shape memory properties. Following this martensite transformation, a key property of this material is the structural deformation induced by magnetic field i.e. the magnetic field induced strain (MFIS) [17]. The first shape memory effect was observed in Ni-Mn-Ga alloy in which a 0.2% of MFIS was observed by Ullako and co-workers in 1996 [18]. Later, the improvement on the material production process and on the subsequent treatment of the alloys has led to MFIS upto 6-10% in the single crystal of Ni-Mn-Ga alloys [19–21].

The mechanism giving rise to shape memory effect in magnetic shape memory alloys is presented in Fig. 1.3. In most of the cases, the high-temperature phase has cubic structure which transforms to a low-symmetry structure in the low-temperature phase, the martensite phase. These low-temperature phases are composed of several regions with different crystallographic orientations, called variants (structural domains). Below Curie temperature, these martensite variants remain magnetically ordered [22]. The magnetic domains within those martensite variants align themselves in such a way that it minimizes the magnetostatic energy [22–24]. If the magnetic anisotropy is weak, the magnetic moments will rotate within each martensite variant which results in very small changes in dimensions corresponding to conventional magnetostriction. However, when the magnetic anisotropy is high and rotation of magnetic domains significantly increases the magnetic energy, the magnetic field orients the structural domains such that their magnetization axis becomes aligned with the externally applied field. In this case, the rotation of the variants is controlled by the difference in Zeeman energy [25] between variants and results in a significant change in the dimension of the sample [26]. The Zeeman energy is the product of applied magnetic field and the magnetization difference between the martensitic variants. So the magnetic field plays an important role in the deformation of the sample like mechanical stress in the conventional shape memory alloys. In general, the deformation caused by induced strain is not restorable after the removal of the magnetic field. Reversibility in shape changes can only be achievable for small deformation. Besides heating the material, other possibilities to recover the induced strain are: rotation of the magnetic field and application of stress perpendicular to the magnetic field [17]. However, the main difference between thermally and magnetic-field-induced pseudoelasticity is that the later does not rely on the twin boundary motion, but on the coupling of structural and magnetic parameters at microscopic level leading to the possibility of inducing martensitic transformation upon application of a magnetic field. Applied magnetic field triggers the forward or reverse martensitic transformation depending upon whether the austenite or the martensite possesses higher magnetization. Similar to thermally induced pseudoelasticity, the forward and the reverse transitions in presence of magnetic field generate hysteresis loop [17].

1.3 Spintronics

Spintronics, or spin-electronics is associated with the study of the role of the electron spin in solid state devices that exploits the spin properties instead of or in addition to the electronic charge degrees of freedoms in metals and semiconductors [27]. In

---

The details of spintronics are given in *Spintronics: from materials to devices*, by Felser, Claudia, and Gerhard H. Fecher, Springer Science & Business Media, 2013.

the spintronics devices, an external magnetic field is used to polarize the electrons by aligning their spins. These polarized electrons are used to control the electric current, known as spin current [28, 29]. There is an enormous number of applications which are possible with spintronics materials. So far, these materials are being effectively used for magnetic memory (data storage) [30, 31] and magnetic recording (read, write head) [32]. The property used for the above applications in these materials is the magnetoresistance (MR) [33] which is the change of resistance of a conductor in an external magnetic field. In the late 1980s, the discovery of the "giant magnetoresistance (GMR)" [34, 35] spearheaded active research interest in the spintronics materials. A GMR device, also known as 'spin valve' consists of different layers of ferromagnetic materials separated by a non-magnetic material. In a GMR device, the large change in resistance takes place due to the application of an external magnetic field by aligning the spins in the materials used. When both the ferromagnetic layers are aligned along the field direction, the electronic resistance becomes lower. If the layers are aligned in opposite directions, the electrical resistance becomes higher. There are two variants of GMR which have been applied in the devices: (1) current-in-plane (CIP), where the electric current flows parallel to the layers and (2) current-perpendicular-to-plane (CPP), where the electric current flows in a direction perpendicular to the layers.

Recently, the spin-valve engineering concept has been used with the phenomenon of spin-dependent tunnelling which allows for the further development of even more sensitive recording read heads. The Magnetic tunnel junction (MTJ) [36, 37] read heads have completely replaced sensors based on the phenomenon of GMR. For further advances in MTJs, new materials with inter-dependent multiple properties are required. Hence, spintronic materials are the suitable candidates for engineering in this field. The interesting thing about MTJs is that it can be upgraded to magnetoresistive random access memory (MRAM) [38, 39] which are non-volatile in nature. The first MTJ based MRAM was demonstrated by IBM in 1999. Nowadays, the active research for MRAM is going on due to its high-density applications [40]. The MRAM devices are suitable for replacing the conventional charge-based memory devices such as Dynamic-RAM(DRAM), Embedded-DRAM and even Static-RAM. In MRAM, the possibility of using spin-transfer-torque (STT) is fascinating along with its high tunneling magnetoresistance [41, 42]. The Spin-transfer-torque (STT) is an effect in which the orientation of the magnetic layers in the MTJ can be adjusted using a spin-polarized current. When the current passes through a thick magnetic layer (usually called the fixed layer), it becomes spin-polarized current which consists of mainly one type of spin (spin-up or spin-down). If the spin-polarized current is directed onto a second thinner layer (the free layer), then the angular moment transfers to this layer by changing its orientation. This is used to oscillate the orientation of the magnet. The STT along with MRAM is called STT-MRAM which has the advantage of low power consumption, more scalability, and unlimited endurance compared to MTJ device [27].

1.4 Exchange bias

Exchange bias (EB) is a property of a coupled antiferromagnetic (AFM) and ferromagnetic (FM) system that occurs due to magnetic interface effects [43]. It was discovered in 1956 by Meiklejohn and Bean while studying Co particles embedded in their native AFM oxide CoO [44]. They observed a displacement of the hysteresis loop which resulted due to the magnetic interactions across the common interface between the oxide layers and the ferromagnetic Co. As the exchange bias was believed to be an interface effect, so the investigations were made mainly on the thin films consisting of a FM layer in contact with an AFM one.

In Fig. 1.4, a phenomenological model of exchange bias has been shown. Consider a system where a FM layer is in close contact with an AFM layer which should satisfy the condition of critical temperatures: $T_C > T_N$, where T_C is the Curie temperature of FM layer and T_N Néel temperature of the AFM layer. In the temperature range $T_N < T < T_C$, the FM spins align in the direction of the applied field, whereas the AFM spins remain randomly oriented in a paramagnetic state. The hysteresis curve of the ferromagnet is centered around zero and not being affected by the presence of the AFM layer(Fig. 1.4 (1)). After achieving the saturation in magnetization, the temperature is being decreased to a finite value without changing the applied magnetic field. During this process, each layer of the AFM spins align antiparallel to the consecutive layer to compete for the AFM order as shown in Fig. 1.4 (2). Hereafter, the AFM spins are uncompensated at the interface which leads to a finite net magnetization of this monolayer. However, it is assumed that both the ferromagnet and the antiferromagnet are in a single domain state and they will remain in a single domain during the remagnetization process. During reversing the field, the FM spins try to rotate in-plane in the opposite direction(Fig. 1.4 (3)). As

---

The fundamental aspects of exchange bias effect are described in *Fundamental Aspects of Exchange Bias Effect in AF/F Bilayers and Multilayers*, by F. Radu, Ph.D. thesis, Ruhr-Universit t Buchum, 2005.

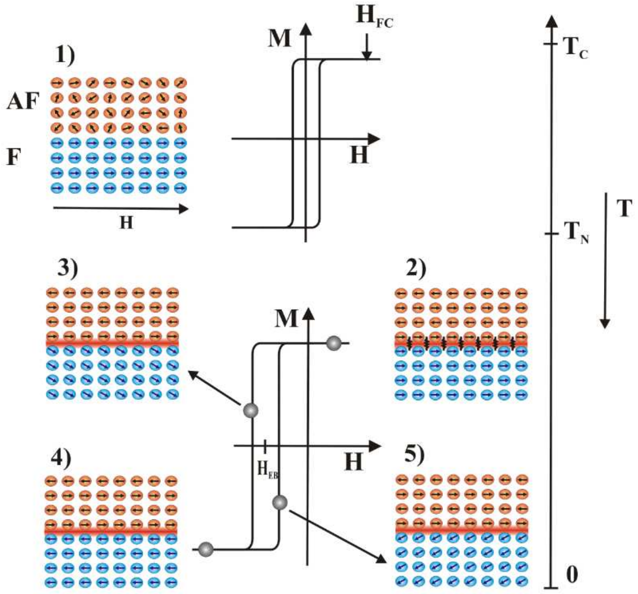

Figure 1.4: Phenomenological model of exchange bias at AFM and FM interface. H_{FC} is the applied magnetic field and H_{EB} is the exchange bias field. The figure is taken form Ref. [43].

the FM spins at the interface are coupled with the AFM spins, a stronger external field is needed to rotate the FM spins. As a result, the first coercive field is higher than the similar one at T > T_N when the coupling between AFM and FM layers was not active. For the reverse process(Fig. 1.4 (4)), the FM spins need a smaller external force in order to rotate along the field direction(Fig. 1.4 (5)). A torque acts on the FM spins for all other directions, except the stable one which is along the field cooling direction (unidirectional anisotropy). Thus, the magnetization curve is shifted towards the negative values of the applied field. This shift in the hysteresis loop is called exchange bias field and the sign of it depends on the orientation of FM spins.

Up to now, it has been discussed that in the exchange bias effect, part of AFM bulk is restricted to pining the interfacial magnetic moment. So the effect is related to the magnetic state at the interface in the AFM bulk. This implies that it is not an entirely interfacial phenomenon but it can also occur in the bulk systems if there is a competing interaction between FM and AFM phase [45, 46]. Eventually, the exchange bias is reported in many different bulk systems in which both FM and AFM magnetic phases are present [47, 48].

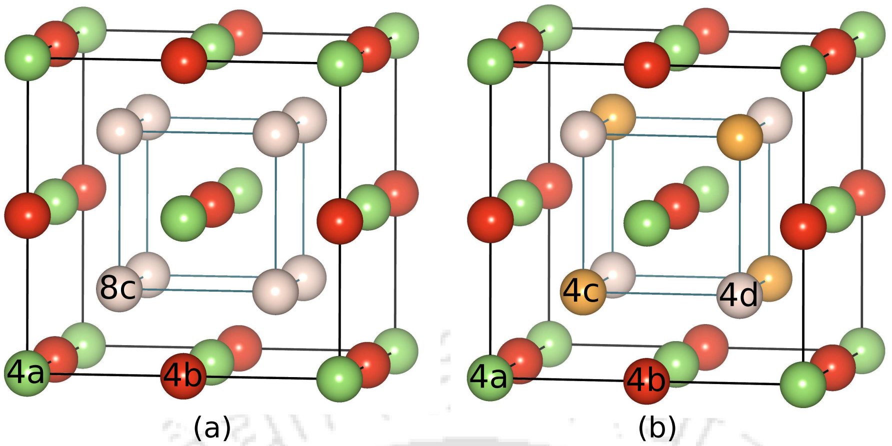

Figure 1.5: (a) Regular Heusler structure (b) Inverse Heusler structure; 4a, 4b, 8c, 4c, and 4d are the Wyckoff positions in their respective structure.

1.5 Mn_2YZ systems: Experimental and theoretical background

Mn_2YZ systems where Y is an element with 3d electrons and Z is an element from Group III or IV of the periodic table, by and large, belong to the family of Heusler compounds. These compounds have attracted considerable attention due to their multifunctional properties. Many compounds in this series show magnetic shape memory effect and magnetocaloric effect, useful for magnetomechanical actuators [20, 49] and magnetic refrigeration [17]. On the other hand, few compounds are promising for spintronics applications such as STT-MRAM [50], spin-valves [51], magnetic tunnel junction [52] and spin-gapless semiconductor [53].

In general, the Heusler compound X_2YZ, crystallizes in the cubic $L2_1$ (Space group no. 225; $Fm\bar{3}m$) structure where the X atoms occupy the Wyckoff position 8c(1/4, 1/4, 1/4), the Y and Z atoms occupy the positions 4b(1/2, 1/2, 1/2) and 4a(0, 0, 0) respectively [54]. In X_2YZ, X and Y are transition metal elements and Z is the main group element. The crystal structure of cubic $L2_1$ is shown in Fig.1.5 (a). Another prototype of Heusler compound, called "inverse" Heusler, is formed in Hg_2CuTi (space group no. 216; $F\bar{4}3m$) structure. In the inverse Heusler structure, the atom at 4b site gets interchanged with one of the atoms at 8c site of regular Heusler alloy. Thus, the X atoms of X_2YZ compounds occupy the Wyckoff positions 4c(3/4, 3/4, 3/4) and 4b(1/2, 1/2, 1/2) whereas the Y and the Z atoms occupy the 4c(1/4, 1/4, 1/4) and 4a(0, 0, 0) positions respectively [54]. The corresponding crystal structure is shown in Fig.1.5 (b). An alternative arrangement of the atoms can also be made as the 4a site is symmetric with 4b and 4c with 4d. Depending on the number of valence electrons of the constitute elements, a system crystallizes in the regular or inverse Heusler structure. If the number of valence electrons of the transition metal element Y is larger than that of the transition metal element X, the system crystallizes in the inverse Heusler structure [54–58]. Experimental and theoretical studies on numerous Heusler compounds established the above rules for site occupancies of X_2YZ Heusler compounds with few exceptions. Another structural phase in the Heusler compounds is the tetragonal derivative of the cubic structure which has been widely reported in magnetic shape memory alloys. The tetragonal structure can be generated through a rotation of the cubic structure by 45° along [110] direction. The cubic unit cell can also be described in terms of tetragonal cell with c/a ratio of $\sqrt{2}$ and the corresponding relations between the cell parameters are c_{tet}=c_{cub} and a_{tet}=$a_{cub}/\sqrt{2}$. Recently, other structural phases such as different modulated structures representing the microstructures of the sample during martensitic transformation, cubic Cu_3Au-like structure and hexagonal structure have been reported [59–62]. The details of these structural phases have been described later for different compounds.

Heusler alloys received a tremendous attention when magnetic shape memory effect was observed in Ni_2MnGa which undergoes a martensitic phase transformation at 202 K and has a Curie temperature of 380 K [63]. Ni_2MnGa crystallizes in a highly ordered $L2_1$ type crystal structure, where Ni, Mn and Ga atoms occupy the 8c, 4b and 4a Wyckoff positions respectively. However, active research started in late 1996 when a 0.2% of MFIS was observed by Ullako and co-workers [18]. Since then, the Heusler Ni-Mn-Ga system has been explored extensively. The reason was that several modulated martensite phases were observed in this system with the composition ratio of Ni, Mn and Ga near 2:1:1. A 6% strain was obtained in the martensitic phase of Ni-Mn-Ga alloy with a five-layered modulated (10M) structure [19, 21]. A MFIS of 10% was also observed in the same system with a seven-layered modulated structure (14M) [20, 21]. In spite of having large MFIS, a martensitic transformation temperature (T_m) below the room temperature and a relatively low Curie temperature (T_c) were serious hindrances in exploiting the functionalities of Ni_2MnGa. This is because of the fact that the T_m being lower than the room temperature makes the commercial realization of the material for shape memory applications difficult. As an alternative, many off-stoichiometric materials were investigated with high content of Ni and low content of Mn or with high content of Mn and low content of Ga with mixed outcomes.

In Mn_2YZ series, Mn_2NiGa is the well studied compound as it is directly related with Ni_2MnGa. It was synthesized during the ongoing process of functionality improvement of Ni_2MnGa by varying the composition of Ni and Mn. Liu *et al.* were the first to synthesize the Mn_2NiGa which crystallized in inverse Heusler structure at high temperatures [64]. As was described earlier, the two Mn atoms occupy the 4a and 4c Wyckoff positions in the Hg_2CuTi lattice; we denote them as MnI and MnII respectively throughout the thesis. Ni and Ga occupy the 4b and 4d sites respectively. Mn_2NiGa exhibits a martensitic transformation around room temperature (T_m=270 K) and has a quite high Curie temperature of 588 K [64]. A MFIS of 4% was also observed in the non-modulated (NM) tetragonal structure [64]. The large values of T_m and T_c compared to the prototype Ni_2MnGa make this material promising for better practical applications. In Mn_2NiGa, the Mn atoms are ferrimagnetically coupled resulting in a low saturation magnetization compared to Ni_2MnGa [65, 66]. Inspite of low magnetization, the ferrimagnetic coupling between two Mn atoms gives rise to a plethora of interesting physical properties in Mn_2NiGa [66]. Singh *et al.* reported spin-valve-like magnetoresistance in Mn_2NiGa at room temperature [51]. Recently, a notable inverse magnetocaloric effect (MCE) was reported in Mn_2NiGa [67]. Experimentally, the existence of few modulated martensite phases has been also reported which can further improve the MFIS in Mn_2NiGa [68, 69].

Another compound in this series, Mn_3Ga, a promising material for spintronics applications, has also been studied extensively. Mn_3Ga crystallizes in cubic, tetragonal and hexagonal structures as reported by different experiments [59, 60, 70, 71]. In the tetragonal and hexagonal phases, a high perpendicular magneto-crystalline anisotropy and a large Exchange Bias are observed, which are useful for STT-MRAM [70] and magnetic tunnel junction [60] applications, respectively. These studies on Mn_2NiGa and Mn_3Ga, motivate the researchers to explore Mn_2YZ systems with different Y and Z elements. For example, Mn_2FeGa has been synthesized in similar crystallographic phases like Mn_3Ga [61, 62, 72]. In the tetragonal phase, Mn_2FeGa behaves like an exchange spring which is useful for magnetic storage technology [61]. A giant exchange bias has also been reported in both tetragonal and hexagonal phases [61, 62]. Another compound, Mn_2CoGa, a high spin-polarized material, has been studied in bulk and thin films and its possible applications have been explored [73, 74]. Recently, Mn_2CoAl has been realized as a spin-gapless semiconductor [53]. From DFT calculations Mn_2NiAl, Mn_2NiSn and Mn_2NiIn are predicted to be magnetic shape memory materials [75–78]. However, the shape memory effect in these materials has been reported experimentally in the off-stoichiometric compositions and a large exchange bias is observed in $Mn_2Ni_{1.6}Sn_{0.6}$ and $Mn_2Ni_{1.6}In_{0.6}$ [79–84].

The structural and magnetic properties in Mn_2YZ systems are thus quite diverse. The basic information of many systems [85, 86] in this series are available but a detailed investigation deciphering the role of each possible factor like site preferences, chemical identity, sub-lattice disorder, magnetic interactions etc. in influencing the physical properties and stabilities of the crystalline phases, could be quite interesting and thus worth exploring. In this thesis we have, therefore, addressed these issue from a microscopic point of view for selected materials.

1.6 The importances of first-principles electronic structure calculations towards inquiring into material properties

The discussions in the previous subsections clearly demonstrate that Mn_2YZ compounds make a playground where the fundamental picture behind the fascinating structural, electronic and magnetic properties of the Heusler compounds can be explored. For a theoretician, the natural way is to do this by obtaining the solution of Schrödinger equation for electrons in real solids, where their quantum mechanical behaviour is determined by the presence of other electrons and atomic nuclei. For such a many body interacting system, exact solution of the Schrödinger equation is not possible. Hence appropriate approximations are required. The Density Functional Theory (DFT) [87, 88] which projects the many body interacting system onto a non-interacting single particle one; where the many body interactions are taken care of in an average way through a single term, has made the required breakthrough to arrive at parameter-free, first principles methods so that robust and accurate results on materials properties can be obtained. Integration of DFT based first-principles methods with advanced softwares made tackling of complex problems accurately within reasonable time period [89–95]. Over the years, application of these methods in calculating the electronic structures of collinear and complex noncollinear magnetic ground states [96–99], dynamical properties of materials [100, 101] and simultaneous comparison of these results with experimental observations confirmed the accuracy of these methods. Various problems related to sub-lattice disordered alloys [102, 103] have also been encountered with these sophisticated tools. Over the years, these methods are widely accepted to predict properties of new materials where experimental evidence is not present. Therefore, the DFT based first-principles methods are the essential tool for fundamental understanding of materials that I have worked with during my doctoral research.

1.7 Outline of the thesis

In this dissertation, we have extensively investigated the structural, electronic and magnetic properties of Mn_2YZ systems (Y=Ni, Fe, Co; Z=Ga, Sn) as well as the phenomena and physics of structural phase transitions in them, by first principles electronic structure calculations. We have systematically explored the fundamentals of structural modifications, site occupancies, chemical disorder, magnetic interactions and phase stabilities in these systems. The computations and analysis are done with the help of DFT-based electronic structure methods, and simple models, wherever applicable.

Chapter 1 starts with the importance of functional materials in the context of technological revolution followed by a discussion on the importances of Heusler systems. A review on the magnetism related functional properties observed in the Heusler systems in the context of our systems of interest is then done.

Chapter 2 contains a brief description of theoretical methods which are used for material simulations. This chapter starts with a description of Density functional theory (DFT), the backbone of current day electronic structure calculations in complex materials. Various implementations of the DFT which are used in this work are then described. In this work, we have used two techniques: the projected augmented wave method (PAW) and Korringa Kohn Rostoker-Green's function method which are implemented in Vienna Ab initio Simulation Package (VASP) and Munich Spin-Polarized-Relativistic Korringa-Kohn-Rostoker (SPRKKR) band structure program package, respectively. The PAW method was developed by combining ideas from all electron- Linearized Augmented Plane Wave(LAPW) and Pseudopotential methods. The main idea of PAW method was to divide the wave function into two parts: partial wave expansion in a sphere around the atom (augmentation region) and envelope functions outside the spheres (interstitial region) which are connected by a linear transformation at the sphere radius. The KKR-Green's function method is based on the multiple-scattering theory which provides a unique framework to solve many different problems in electronic structure theory. Within this formalism, the chemical disorder can be conveniently treated with the coherent potential approximation (CPA).

In **Chapter 3**, we investigate the sequence of phase stability in Mn_2NiGa from high temperature to low temperature and make an attempt to understand the origin of such sequence as the system is driven from high-temperature cubic to low temperature non-modulated(NM) tetragonal variant. In our study, we only consider the commensurate modulated structures ubiquitous in literature, like 6M, 10M and 14M with wave-like modulations confined in an orthorhombic cell and nano-twinned structures with fully optimized monoclinic lattice parameters. We first optimize the different modulated and NM tetragonal structures and obtain a volume change of less than 1% with respect to the cubic phase, a prerequisite for shape memory properties. From the optimized c/a (c/a determines the structural deformation) ratio, we predict that the maximum theoretically achievable MFIS (as $|1 - c/a|$), for the wavelike modulated structure is 11% and that for monoclinic structure is 13%, both higher than those in Ni-rich Ni-Mn-Ga systems. The relative stability of different structural phases is investigated from the total energy calculations. From energetics, it has been seen that the high-temperature cubic phase drives towards an intermediate 6M pseudocubic(modulated structure with $c/a = 1$) state, which immediately decays downhill into a modulated structure with a significant pseudo-tetragonal distortion. Afterwards, the relaxations of the internal coordinates and the structural parameters stabilize other modulated structures. With the orthorhombic constraint for the simulation cell, the minimum energy state is obtained for the $14M_{2/7}$ modulation. This is in agreement with the results of Brown et al. obtained at low-temperature [69]. Further relaxation of the shape of the cells leads the 10M and 14M pseudotetragonal structures to monoclinic $10M(3\bar{2})_2$ and $14M(5\bar{2})_2$ structures by lowering energies. Once again, the $14M(5\bar{2})_2$ structure has the lowest total energy, in agreement with the observation of a monoclinic 14M structure by Singh et al. [68]. The relative stability of different structural phases is explained from the electronic structures. The fundamental question on the origin of the modulated structures is addressed by computing the phonon dispersion relations, Fermi surface and generalized electronic susceptibility. Significant differences with Ni_2MnGa, particularly in the context of adaptive martensites, are highlighted and discussed. In summary, the work in this chapter explores the fundamental physics associated with the phase transformations in Mn_2NiGa which was not addressed earlier.

In **Chapter 4**, We investigate the effects of Fe and Co substitutions on the mechanical, electronic and magnetic properties and on the stability of the low temperature martensitic phase of Mn_2NiGa. The evolution of these aspects upon substitution of Fe and Co at different crystallographic sites are investigated by computing the electronic structures, mechanical properties (tetragonal shear constant, Pugh ratio and Cauchy pressure) and magnetic exchange parameters. We find that the martensitic phase of Mn_2NiGa gradually de-stabilizes with an increase in the concentration of Fe/Co due to the weakening of the minority spin hybridization of Ni and Mn atoms occupying crystallographically equivalent sites. The interplay between relative structural stability and the compositional changes are understood from the variations in the elastic moduli and electronic structures. We find that like in the Ni_2MnGa-based systems [104–106], the elastic shear modulus C' can be considered as a predictor of composition dependence of martensitic transformation temperature T_m in substituted Mn_2NiGa, thus singling it out as the universally acceptable predictor for martensitic transformation in Ni-Mn-Ga compounds over a wide composition range. The magnetic properties of Mn_2NiGa are found to be greatly improved by the substitutions due to stronger ferromagnetic interactions in the compounds. The gradually weaker(stronger) Jahn-Teller distortion (covalent bonding) in the minority spin densities of states due to substitutions leads to a half-metal-like gap in these compounds resulting in materials with high spin-polarization when the substitutions are complete. The substitutions at the Ga site result in two new compounds Mn_2NiFe and Mn_2NiCo with very high magnetic moments and Curie temperatures. Thus, our work indicates that although the substitutions destabilize the martensitic phase in Mn_2NiGa, new magnetic materials with very good magnetic parameters and potentially useful for novel magnetic applications can be obtained. In summary, this chapter explores the interrelations between the site occupancy, martensitic phase stability, bonding , mechanical and magnetic properties of Fe and Co substituted Mn_2NiGa.

In **Chapter 5**, We investigate the structural and magnetic properties of Mn_2FeGa in different structural phases(cubic, hexagonal and tetragonal) which are reported experimentally. The relative structural stabilities and the possible phase transformation mechanisms are discussed using results for total energy, electronic structure, and elastic constants. We find that the phase transformation from hexagonal to ground state tetragonal structure would take place through a meta-stable Heusler-like phase.

The electronic structures, the elastic constants, and the phonon dispersions indicate that the transition from the Heusler-like phase to the ground state tetragonal phase is of pure Jahn-Teller origin. A major highlight of this chapter is the investigation into the ground state magnetic structures in each phase. For Heusler-like and tetragonal phases, we find that the ferromagnetic exchange interactions associated with the Fe atoms balance the dominating antiferromagnetic interactions between the Mn atoms leading to collinear magnetic structures. In the hexagonal phase, we find that the atomic moments are confined in the planes in a collinear-like fashion, in stark contrast to the well known non-collinear magnetic structure in the hexagonal phase of Mn_3Ga [107, 108], another material with similar structural properties. The overwhelmingly large exchange interactions between atom pairs involving Fe destroy the possibility of magnetic frustration in the hexagonal phase of Mn_2FeGa. In summary, the work of this chapter provides a comprehensive study of the microscopic physics associated with the structural and magnetic orders in different phases of Mn_2FeGa.

In **Chapter 6**, we investigate the impacts of site occupancy, composition and magnetic structure on the stability of the martensitic phases in $Mn_2Ni_{1+x}Sn_{1-x}$. Impact of each one of these factors is explored in a systematic way to understand their individual roles. The major highlight of this work is unraveling the facts that the magnetic structure changes with martensitic transformation whose origin lies in the changes in the electronic structures due to different orientations of Mn atoms occupying three different sites in the lattice, and that the presence of Mn at the Sn site is crucial to reproduce the experimentally observed trends in the structural and magnetic properties of this system. An important by product of the findings is a possible explanation of the discrepancies between experimental observation and DFT calculations regarding phase stability in Mn_2NiSn. The work in this chapter provides significant insight into the mechanism of phase transformation in Mn-excess Ni-Mn-Sn system which will probably hold for similar other systems like Mn-excess Mn-Ni-In.

In **Chapter 7**, we summarise the outcome of the thesis and discuss the possible extensions.

Chapter 2

Methodology

In this chapter, we describe the theoretical methods which are used in this thesis for material simulations. The study carried out in this thesis is mainly based on density functional theory (DFT), which is described in section 2.3. In this chapter, we provide descriptions of two different implementations of DFT for calculations of ground state properties, which are used to obtain results presented in the thesis. Apart from descriptions to obtain the ground-state charge density and total energy, we also provide descriptions regarding calculations of elastic moduli, magnetic exchange interactions, the magnetic transition temperatures and the phonon dispersion relations using DFT results.

2.1 The many-body Hamiltonian

The nonrelativistic, time-independent many body Schrödinger equation for solving the electronic structure of a solid can be written as

$$\mathcal{H}\Psi = E\Psi \tag{2.1}$$

Where Ψ is the many body wavefunction of the form,

$$\Psi = \Psi(\mathbf{r}_1, \mathbf{r}_2, ..., \mathbf{r}_i, ..., \mathbf{R}_1, \mathbf{R}_2, ..., \mathbf{R}_I, ...) \tag{2.2}$$

$\mathcal{H}$ is the Hamiltonian and E is the total electronic energy. The indices i and I are for electrons and atomic nuclei, respectively. The Hamiltonian $\mathcal{H}$ can be written as

$$\begin{aligned}\mathcal{H} = -\frac{\hbar^2}{2}\sum_{I}\frac{\nabla_I^2}{M_I} + \frac{1}{2}\sum_{I\neq J}\frac{Z_I Z_J e^2}{|\mathbf{R}_I - \mathbf{R}_J|} - \frac{\hbar^2}{2}\sum_{i}\frac{\nabla_i^2}{m_i} \\ + \frac{1}{2}\sum_{i\neq j}\frac{e^2}{|\mathbf{r}_i - \mathbf{r}_j|} - \sum_{i,I}\frac{Z_I e^2}{|\mathbf{r}_i - \mathbf{R}_I|}\end{aligned} \tag{2.3}$$

Where Z_I and M_I are charge and mass of the nucleus and mass of electron is m_i. The nuclear coordinates are given by $\mathbf{R}_I$ and electronic coordinates are given by $\mathbf{r}_i$. The first and third terms in the Hamiltonian are kinetic energies of nuclei and electrons, respectively. The second, fourth and fifth terms are Coulomb interactions between nuclei and nuclei, electrons and electrons and electrons and nuclei, respectively. The many body Hamiltonian given by Eq. 2.3 is difficult to solve for solid state systems and approximations are required at different levels. In the next subsections we discuss them.

2.2 The Born-Oppenheimer approximation

The many-body problem can be simplified by Born-Oppenheimer approximation [109]. The Born-Oppenheimer approximation uses the fact that the nuclei are much more massive than the electrons. Therefore, the time scale associated with nuclear motion is orders of magnitude larger than that of the electrons and hence the nuclei can be considered as motionless. Thus, their kinetic energy can be neglected and the potential energy due to nucleus-nucleus interactions is assumed to be constant. Accordingly, under the Born-Oppenheimer approximation, the many-body contribution mainly comes from electrons and the electronic Hamiltonian is given by

$$\begin{aligned}\mathcal{H}_{el} &= -\frac{\hbar^2}{2}\sum_{i}\frac{\nabla_i^2}{m_i} + \frac{1}{2}\sum_{i\neq j}\frac{e^2}{|\mathbf{r}_i - \mathbf{r}_j|} - \sum_{i,I}\frac{Z_I e^2}{|\mathbf{r}_i - \mathbf{R}_I|} \\ &= T_e + V_{ee} + V_{ext}\end{aligned} \tag{2.4}$$

T_e is the kinetic energy of the electrons, V_{ee} is the Coulomb energy due to electron-electron interaction and V_{ext} is the interaction with external potential.

2.3 Density Functional Theory (DFT)

Inspite of the simplification due to Born-Oppenheimer approximation, Eq. 2.1 is still an extremely complicated many-body eigenvalue problem to solve as a solid contains N electrons resulting in 3N number of degrees of freedom. The Density Functional Theory (DFT) circumvents this by focusing on one electron density rather than the many-body wave function to solve the Schrödinger equation for a large electronic system. An early version of the density functional theory was proposed by Thomas [110] and Fermi [111] where the kinetic energy was represented by one electron density. The all important electron-electron interactions were incorporated by a mean field approximation which was common to the wave function based Hartree [112] and Hartree-Fock [113] approaches. However, the semi-classical Thomas Fermi approximation, inspite of pointing out the importance of one electron density to obtain the ground state properties in a solid, failed miserably to address the exchange and correlation effects in a many body electronic system. In 1964, Hohenberg and Kohn [87] provided the required breakthrough. Their approach, which is the backbone of current day DFT, is summarized in the following two theorems:

1. The external potential $V_{ext}(\mathbf{r})$ is uniquely determined by the electron density $n(\mathbf{r})$ so the total energy is a unique functional of the density E[n] [89].

2. The true ground state density n(r) minimizes this total energy functional E[n] and the minimum energy is the ground state energy E_0 [89].

According to the above theorem, the ground state energy of interacting electrons in an external potential $V_{ext}(\mathbf{r})$ is described by an energy functional

$$E[n] = F[n] + \int V_{ext}(\mathbf{r}) n(\mathbf{r})\, d\mathbf{r} \tag{2.5}$$

The first term is a universal functional of the electron density $n(\mathbf{r})$ and the second term represents interaction energy with the external potential. The total energy in the ground state is realized through the minimization of $E[n]$.

Therefore, the ground state density, in principle, uniquely determines the ground state properties of an interacting electronic system. This approach, thus, offers a perspective different than the conventional methods where many body wave functions are to be computed, which is often a difficult task. The success of the DFT lies in using the Hohenberg and Kohn theorem in conjunction with the Kohn-Sham formalism [88] in which the many body problem is mapped onto a single body problem where the many body system is treated as a single body in an effective external field. This mapping by Kohn and Sham resulted in a Schrödinger like equation for single particle which provides a variational total energy and thus the ground state single particle density to a good approximation

$$(H_{ks} - \epsilon_i)\phi_i(\mathbf{r}) = 0 \tag{2.6}$$

$$H_{ks} = -\frac{1}{2}\nabla^2 + V_{eff} \quad (in\ Hartree\ units) \tag{2.7}$$

where,

$$V_{eff} = V_{ext}(\mathbf{r}) + V_{Hartree}(\mathbf{r}) + V_{xc}(\mathbf{r}) \tag{2.8}$$

The second term is called Hartree potential,

$$V_{Hartree} = \frac{1}{2}\int \frac{n(\mathbf{r})n(\mathbf{r}')}{|\mathbf{r}-\mathbf{r}'|}\, d\mathbf{r}d\mathbf{r}' \tag{2.9}$$

and the last term is exchange-correlation potential defined as,

$$V_{xc} = \frac{\delta E_{xc}[n]}{\delta n(\mathbf{r})} \tag{2.10}$$

which includes electron-electron interaction beyond the Hartree term. The density is calculated from single-electron orbitals according to

$$n(\mathbf{r}) = \sum_{i=1}^{N} |\phi_i(\mathbf{r})|^2 \tag{2.11}$$

The total number of electron is obtained as

$$N = \int n(\mathbf{r})\, d\mathbf{r} \tag{2.12}$$

The self-consistent equations (2.5-2.12) are used to compute the ground state energy of an electronic system with

$$E_{ks} = T_s[n] + \int V_{ext}(\mathbf{r})n(\mathbf{r})\, dr + E_{Hartree}[n] + E_{xc}[n] \tag{2.13}$$

Although the Kohn-Sham theory is exact in principle, further approximations are required as the exchange and correlation terms are not known exactly, except for the free (homogeneous) electron gas. The simplest approach to obtain an approximate E_{xc} is the local density approximation (LDA) [88]. The LDA assumes that the variation of density in a solid is insignificant locally and thus the electron density in a solid can be mimicked using that of the homogeneous electron gas. The E_{xc}, under LDA, is given by

$$E_{xc}^{LDA}[n] = \int n(\mathbf{r})\varepsilon_{xc}^{hom}(n(\mathbf{r}))d^3r \tag{2.14}$$

where ε_{xc}^{hom} is the sum of the exchange and correlation energies of the homogeneous electron gas of density $n(\mathbf{r})$.

LDA, however, ignores the exchange-correlation energy at point $\mathbf{r}$ due to nearby inhomogeneities in the electron density. Inspite of this, the success of LDA is remarkable due to the fact that it gives the correct sum rule for the exchange-correlation hole. However, it failed upto the extent of producing wrong electronic ground state in some important cases. An attempt to improve the LDA was made by introducing the gradient corrections on the electron density, the generalized gradient approximation (GGA) [114–116]. The GGA functional is given by

$$E_{xc}^{GGA}[n] = \int d^3r\, n(\mathbf{r})\, \varepsilon_{xc}^{GGA}(n(\mathbf{r}), |\nabla n(\mathbf{r})|) \tag{2.15}$$

For systems where the charge density varies slowly, the GGA functional improves the results. Calculations presented in the thesis are done with the GGA functionals.

Depending on the nature of the problem addressed, developing accurate and at the same time efficient numerical methods for solving the Kohn-Sham equations is the biggest challenge in computational material science. Currently, there are three major groups of methodologies: the Pseudopotential (PP) method, the full potential (FP) method and the Green's function method.

2.4 Pseudopotential method

Bloch's theorem states that the wavefunction of an electron in a band can be expanded using a discrete set of plane waves. However, a plane wave basis set is poorly suited to expand electronic wavefunctions because a very large number of plane waves are required to expand the tightly bound core orbitals and to represent the rapid oscillations of the wavefunctions of the valence electrons in the core region. The construction of the pseudopotentials removes the rapid oscillations in the wave functions of the valence electrons in the core region, resulting in a smooth valance wavefunction there. Consequently, the pseudo-wavefunctions can be represented by a reasonable number of plane waves, making the method computationally tractable. In the next subsections, we briefly describe the evolution of plane wave based pseudopotentials which are widely used in the electronic structure calculations.

2.4.1 Norm-Conserving Pseudopotentials (NCPP)

The norm-conserving pseudopotentials (NCPP) were the first in the block of pseudopotentails which were computationally tractable. The NCPPs are generated by putting up the constraint that the norm of the pseudo wave function is same as that of the all electron wave function within some cut-off distance $\mathbf{r}_c$. The condition is mathematically stated as,

$$\int_0^{\mathbf{r}_c} \varphi^{PS*}(r)\varphi^{PS}(r)r^2\, dr = \int_0^{\mathbf{r}_c} \varphi^{AE*}(r)\varphi^{AE}(r)r^2\, dr \tag{2.16}$$

φ^{PS*} and φ^{AE} are the pseudo and all electron wave functions respectively. Though working well for *sp* elements, this approach becomes somewhat intractable for transition metals and rare earth elements as very large plane wave basis sets are required for localized d and f states.

2.4.2 Ultrasoft Pseudopotentials (USPP)

The concept of pseudopotential is that the considered pseudo-wavefunctions should match to the all-electron wavefunctions outside $\mathbf{r}_c$, as prescribed within norm-conserving pseudopotentials scheme. However, inside $\mathbf{r}_c$ they are allowed to soften as much as possible. With norm-conservation criteria, it is unrealistic to make the pseudopotential dramatically smooth inside $\mathbf{r}_c$. Thus, a large plane wave basis set is required which is in contrast to the requirement of fast convergence in the plane wave based calculations. To overcome this issue, in 1990, Vanderbilt proposed a new and radical idea for generating pseudopotentials [117–119]. Although this introduces some complications, it greatly reduces the number of plane waves required to construct the basis set. The three-fold complications inherent to the construction of ultrasoft pseudopotential are: (i) since the wavefunctions are not necessarily been normalized, they introduce a non-trivial overlap term in the secular equation, (ii) the pseudo charge density cannot simply be obtained with calculations $\sum \varphi^{*}\varphi$ as done with norm-conserving pseudopotentials. Rather, a term is needed to be added in the core region, (iii) relaxation of the norm conservation results in less transferable pseudopotentials. Nevertheless, usage of these pseudopotentials over the years in large-scale calculations proved their reliability in condensed matter calculations and most importantly, the cost of generating these kinds of pseudopotentials is negligible compared to the cost of calculations where they are used.

2.5 Projector Augmented Wave (PAW) method

Inspite of the enormous benefits in terms of speed and memory, the major drawback of pseudopotential method is that all the information of the full wave function are lost close to the nuclei which can influence the result obtained in cases of certain properties, such as hyperfine parameters and electric field gradients. Another disadvantage is that there are many adjustable parameters and degrees of freedom for the generation of the pseudopotentials. For this reason, a particular pseudopotential with fixed parameters may not give the accurate results under all circumstances. A more general approach introduced by Peter Blöchl in 1994 is the Projector Augmented Wave (PAW) method [120]. The PAW method was developed by combining ideas from all-electron-Linearized Augmented Plane Wave(LAPW) [92–95] and Pseudopotential methods. The main idea of PAW method was to divide the wave function into two parts: partial wave expansion in a sphere around the atom (augmentation region) and envelope functions outside the spheres (interstitial region) which are connected by a linear transformation at the sphere radius. In this section, we present a brief description of this formalism.

In the PAW method, the all electron wavefunction $|\psi_n>$ is represented by a smooth wavefunction after a linear transformation with operator T

$$|\psi_n >= T\,|\tilde{\psi}_n > \tag{2.17}$$

Around each atom, a augmented sphere ($|\mathbf{r} - \mathbf{R}^a| < r_c^a$) is constructed, where r_c^a is the cut-off radius, a is the atom index, $\mathbf{R}^a$ is the atom position. The linear transformation operator T can be written as

$$T = 1 + \sum_a T^a \tag{2.18}$$

where T^a only acts in the augmentation sphere. Within the augmentation region, the smooth wavefunction can be expanded into smooth partial waves $\tilde{\phi}^a$

$$|\tilde{\psi}_n >= \sum_{ia} c^a_{ni} |\tilde{\phi}^a_i > \tag{2.19}$$

Similarly the all-electron wavefunction can be written as

$$|\psi_n >= \sum_{ia} c^a_{ni} |\phi^a_i > \tag{2.20}$$

The smooth partial wave after linear transformation operation

$$|\phi^a_i >= T\, |\tilde{\phi}^a_i >= (1 + T^a)\, |\tilde{\phi}^a_i > \tag{2.21}$$

As T^a only acts inside the augmented sphere, so the Eq. 2.21 at $r > r^a_c$

$$|\phi^a_i >= |\tilde{\phi}^a_i > \tag{2.22}$$

Now the true wavefunction are expressed as (using Eq 2.19 and 2.12)

$$|\psi_n >= |\tilde{\psi}_n > - \sum_{ia} c^a_{ni} |\tilde{\phi}^a_i > + \sum_{ia} c^a_{ni} |\phi^a_i > \tag{2.23}$$

As the transformation operator T is linear, the coefficient of the smooth partial wave must be scaler product and

$$c^a_{ni} =< \tilde{p}^a_i | \tilde{\psi}_n >\equiv \mathcal{P}^a_{ni} \tag{2.24}$$

where $\tilde{p}^a_i$ are some smooth projector operators. So the transformation operator T become

$$\mathcal{T} = \sum_a \sum_i (|\phi^a_i > - |\tilde{\phi}^a_i >) < \tilde{p}^a_i | \tag{2.25}$$

After the transformation in Eq. 2.25, the Kohn-Sham wavefunction is

$$\begin{aligned} |\psi_n > &= |\tilde{\psi}_n > + \sum_a \sum_i (|\phi^a_i > - |\tilde{\phi}^a_i >) < \tilde{p}^a_i | \tilde{\psi}_n > \\ &= |\tilde{\psi}_n > + \sum_a \left(\sum_i (|\phi^a_i >< \tilde{p}^a_i | \tilde{\psi}_n > - |\tilde{\phi}^a_i >< \tilde{p}^a_i | \tilde{\psi}_n > \right) \end{aligned} \tag{2.26}$$

From Eq. 2.26, the wavefunction can be decomposed as the sum of the smooth wavefunctions (smooth everywhere) and sum over the subtraction of one-centred all electron contribution and one-centred pseudo part. Using Eq. 2.26 in Eq. 2.17, one can obtain compact expression for various quantities in PAW method [121–124]. Throughout the thesis, We have used the PAW method as implemented in the VASP code [125].

2.6 Korringa, Kohn and Rostoker (KKR) Green's Function method

The Korringa-Kohn-Rostoker (KKR) method for electronic structure calculation of materials was introduced in 1947 by Korringa [90] and in 1954 by Kohn and Rostoker [91]. In this approach, the scattering properties of each atom center are determined first by a scattering matrix. In the next step, the multiple-scattering theory is applied for solving the equation of one electron scattered at many different potentials (all atomic sites in the lattice). The single scattering and the multiple scattering problems are connected by a condition that the incident wave at each scattering centre has to be equal to the sum of the outgoing waves from all the other scattering centres. Due to the above splitting, the structural part is separated from the potential part which made this formalism tractable.

The significant development of the KKR method is made by construction of the Green function. This method is able to produce the crystal Green function efficiently by relating it to the Green function of free space via the Dyson equation which also works efficiently for a system with an impurity in the crystal. So, KKR method with Green function is an extremely efficient technique for solving the impurity problem without the construction of huge supercells which are needed in wavefunction based methods. The KKR Green's Function method can be straightforwardly applied to

1. Systems with impurity
2. Surfaces or arbitrarily layered systems
3. Disordered systems using appropriate alloy theory
4. Calculation of response functions and susceptibility

The kew steps in the KKR Green's Function formalism are as described below.

Suppose that the system is composed of an assembly of non-overlapping spherical muffin-tin potentials centered on each lattice site of a crystal. Then, the crystal

Green's function $G(\mathbf{r}, \mathbf{r}^{'}; E)$ can be evaluated from the free space Green's function $g(\mathbf{r}, \mathbf{r}^{'}; E)$ by

$$G(\mathbf{r}, \mathbf{r}^{'}; E) = g(\mathbf{r}, \mathbf{r}^{'}; E) + \int dr^{''} g(\mathbf{r}, \mathbf{r}^{''}; E) V(\mathbf{r}^{''}) G(\mathbf{r}^{''}, \mathbf{r}^{'}; E) \tag{2.27}$$

where $V(\mathbf{r}^{'})$ denotes the assembly of muffin-tin potentials. In reality, the above equation can not be used for calculations because of convergence problem. Instead, a cell-centered angular momentum based representation is introduced. Let's first consider the cell-centered representation of $g(\mathbf{r}, \mathbf{r}^{'}; E)$

$$\begin{aligned} g(\mathbf{r} + \mathbf{R_m}, \mathbf{r}^{'} + \mathbf{R_n}; E) &= g(\mathbf{r}, \mathbf{r}^{'} + \mathbf{R_n} - \mathbf{R_m}; E) \\ &= -i\sqrt{E} \sum_{L} J_L(\mathbf{r}) H_L(\mathbf{r}^{'} + \mathbf{R_n} - \mathbf{R_m}) \end{aligned} \tag{2.28}$$

where H_Ls are the Hankel functions. Using the addition theorem of Hankel functions,

$$H_L(\mathbf{r}^{'} + \mathbf{R_n} - \mathbf{R_m}; E) = \frac{i}{\sqrt{E}} \sum_{L^{'}} g^{mn}_{LL^{'}}(E) J_{L^{'}}(\mathbf{r}; E) \tag{2.29}$$

and utilizing the following abbreviations

$$\begin{aligned} J_L(\mathbf{r}; E) &= j_\ell(\sqrt{E}r) Y_L(\mathbf{r}) \\ H_L(\mathbf{r}; E) &= h_\ell(\sqrt{E}r) Y_L(\mathbf{r}) \end{aligned} \tag{2.30}$$

the free electron Green's function can be expressed as

$$\begin{aligned} & g(\mathbf{r} + \mathbf{R_m}, \mathbf{r}^{'} + \mathbf{R_n}; E) = -i\sqrt{E}\delta_{mn} \textstyle\sum_L J_L(r_<; E) H_L(r_>; E) \\ & + \textstyle\sum_{LL^{'}} J_L(\mathbf{r}; E) g^{mn}_{LL^{'}} J_L(\mathbf{r}^{'}; E) \end{aligned} \tag{2.31}$$

The structure constants are defined by

$$g^{mn}_{LL^{'}}(E) = -4\pi i\sqrt{E}(1 - \delta_{mn}) \sum_{L^{''}} i^{\ell - \ell^{'} + \ell^{''}} C^{L^{''}}_{LL^{'}} H_{L^{''}}(R_m - R_n; E) \tag{2.32}$$

with the Gaunt coefficients

$$C^{L^{''}}_{LL^{'}} = \int d\Omega Y_{L^{''}}(\mathbf{r}) Y_{L^{'}}(\mathbf{r}) Y_L(\mathbf{r}) \tag{2.33}$$

Similarly, the crystal Green's function has the cell-centered representation as follows,

$$\begin{aligned} &G(\mathbf{r}+\mathbf{R_m},\mathbf{r}'+\mathbf{R_n};E) = -i\sqrt{E}\delta_{mn}\textstyle\sum_L \mathcal{J}_L(r_<;E)\mathcal{H}_L(r_>;E) \\ &+\textstyle\sum_{LL'}\mathcal{J}_L(\mathbf{r};E)G^{mn}_{LL'}\mathcal{J}_L(\mathbf{r}';E) \end{aligned} \tag{2.34}$$

with

$$\begin{aligned} \mathcal{J}_L(\mathbf{r};E) &= P_\ell(\sqrt{E}r)Y_L(\mathbf{r}) \\ \mathcal{H}_L(\mathbf{r};E) &= Q_\ell(\sqrt{E}r)Y_L(\mathbf{r}) \end{aligned} \tag{2.35}$$

The second term, in equation 2.31, represents the contribution of the multiple scattering or back scattering to the Green's function and produces the band structure. The relation between $G^{mn}_{LL'}(E)$ and $g^{mn}_{LL'}(E)$ can be obtained by inserting the above expressions for the Green's function into the integral equation

$$G^{mn}_{LL'}(E) = g^{mn}_{LL'}(E) + \sum_{L''m'} g^{mm'}_{LL'}(E)t^{m'}_{L''}G^{m'n}_{L''L'}(E) \tag{2.36}$$

where t-matrix $t^{m'}_{L''}$ is defined as

$$t^{m'}_{L''} = \int\int d\mathbf{r_m}d\mathbf{r}'_{\mathbf{m}}J_L(\mathbf{r}_{m'};E)t^{m'}(\mathbf{r}_{m'},\mathbf{r}'_{m'};E)J_{L'}(\mathbf{r}'_{m'};E) \tag{2.37}$$

When the scattering centers are aligned periodically in the crystal, $G^{mn}_{LL'}$ and $g^{mn}_{LL'}$ can be Fourier transformed as,

$$G^{mn}_{LL'}(\mathbf{R}_m-\mathbf{R}_n;E) = \frac{1}{\tau}\int_\tau G_{LL'}(\mathbf{k},E)e^{i\mathbf{k}(\mathbf{R_m}-\mathbf{R_n})}d\mathbf{k} \tag{2.38}$$

$$g^{mn}_{LL'}(\mathbf{R}_m-\mathbf{R}_n;E) = \frac{1}{\tau}\int_\tau g_{LL'}(\mathbf{k},E)e^{i\mathbf{k}(\mathbf{R_m}-\mathbf{R_n})}d\mathbf{k} \tag{2.39}$$

where τ is the volume of the first Brillouin zone. Substituting them into equation 2.36, one gets

$$G_{LL'}(\mathbf{k},E) = g_{LL'}(\mathbf{k},E) + \sum_{L''} g_{LL'}(\mathbf{k},E)t_{L''}G_{L''L'}(\mathbf{k},E) \tag{2.40}$$

Finally,

$$G_{LL'}(\mathbf{k},E)=\sum_{L''}[\delta_{L''L}-g_{L''L}(\mathbf{k},E)t_L]g_{L''L}(\mathbf{k},E) \tag{2.41}$$

Then, the crystal Green's function is given by

$$\begin{gathered}G(\mathbf{r}+\mathbf{R_m},\mathbf{r}^{'}+\mathbf{R_n};E)=-i\sqrt{E}\delta_{mn}\textstyle\sum_L\mathcal{J}_L(r_<;E)\mathcal{H}_L(r_>;E)\\ +\mathcal{J}_{Lm}(\mathbf{r})\int\frac{d\mathbf{k}}{\tau}exp(i\mathbf{k}.(\mathbf{R_m}-\mathbf{R_n}))\textstyle\sum_{L''}g_{LL''}(\mathbf{k},E)[1-tg(\mathbf{k},E)]^{-1}_{L''L'}\mathcal{J}_{L'n}(\mathbf{r}^{'})\end{gathered} \tag{2.42}$$

The band structure is then calculated by finding the zeros of the determinant of the matrix appearing in equation 2.41 for each **k**

$$det|\delta_{LL'}-t_L(E)g_{LL'}(\mathbf{k};E)|=0 \tag{2.43}$$

The procedure determines the energy eigenvalues as a function of **k** and hence, yields an energy dispersion relation $E(\mathbf{k})$. The zeros of the KKR matrix gives the poles of the Green's function; each pole corresponds to the eigenstate of the Hamiltonian.

In this thesis, we have extensively used this method for chemically disordered systems. The chemical disorder is treated by coherent potential approximation (CPA), which we discuss in the next section. We have used the Munich group's implementation of the KKR-CPA method as done in their SPRKKR package [126].

2.7 Coherent Potential Approximation (CPA)

For electronic structure calculations of chemically disordered systems, Coherent Potential Approximation (CPA) has been used widely. P. Soven was first to introduce the CPA method [127]. Later, D. W. Taylor has used this concept for phonons in random alloys [128]. In 1972, B. L. Gyorffy implemented this method in the framework of the multiple scattering theory using Green function technique [129]. Over the years, this method is used for the calculation of lattice parameters, elastic constants, mixing enthalpy, etc., for disordered alloys with an accuracy similar to the ordered systems. The main approximation is that the disordered system can be replaced by an ordered effective medium, the parameter of which is determined self-consistently. The single-site approximation is used to treat the impurity problem which means that the single impurity is placed in an effective medium and no information is provided about the individual potential and charge density beyond the sphere or polyhedra around this impurity. Let us consider a substitutional alloy

$A_aB_bC_c$, . . . , where the atoms A, B, C, . . . are randomly distributed in the lattice sites. Here a, b, c, ... stand for the atomic fractions of the A, B, C, ... atoms, respectively. The Green's function g and the alloy potential P_{alloy} are used to characterize the above system. In real alloy, due to the disorder in the environment, the alloy potential varies uniform around the same type of atoms. There are two important approximations within the CPA. The first approximation within the CPA is that the local potentials around a certain type of atoms from the alloy are the same, i.e. the effect of the local environment is neglected. These local potentials are described by the potential functions P_A, P_B, P_C, ... Second approximations are that the system is replaced by a monatomic set-up described by the site independent coherent potential $\tilde{\mathrm{P}}$. Therefore, the real Green's function g is approximated by the coherent Green's function $\tilde{g}$. For each alloy component $i =$ A, B, C, . . . a single-site Green's function g_i is introduced. The main steps to construct the CPA effective medium are as follows.

First, the coherent Green's function is calculated from the coherent potential with an electronic structure method.

$$\tilde{g} = \left[S - \tilde{P}\right]^{-1} \tag{2.44}$$

here S denotes the structure constant matrix corresponding to the underlying lattice. Next, the Green's functions of the alloy components, g_is are determined by substituting the coherent potential of the CPA medium by the real atomic potential P_i, which is given by

$$g_i = \tilde{g} + \tilde{g}\left(P_i - \tilde{P}\right) g_i;\ i = A, B, C \tag{2.45}$$

Finally, the average of the individual Green's functions should reproduce the single-site part of the coherent Green's functions, i.e.,

$$\tilde{g} = ag_A + bg_B + cg_C + ... \tag{2.46}$$

The above three equations are solved iteratively and the output $\tilde{g}$'s and g_i's are used to determine the electronic structure, charge density and total energy of random alloys [130].

2.8 Calculation of elastic moduli

In the next few subsections, we describe the approach to calculate the elastic moduli adopted in this thesis.

2.8.1 Bulk Modulus

The bulk modulus (B) describes the behaviour of the crystal volume or lattice parameters under hydrostatic pressure. It is evaluated from the energy-volume $E(V)$ relations. The bulk modulus can be obtained from the Birch-Murnaghan isothermal equation of state which is a relationship between the total energy with crystal volume under hydrostatic pressure [131]. The third order B-M equation of state is given by

$$\begin{aligned} E(V) = & E_0 + \frac{9}{16} B V_0 \\ & \times \left\{ \left[\left(\frac{V_0}{V} \right)^{\frac{2}{3}} - 1 \right]^3 B_0' - \left[\left(\frac{V_0}{V} \right)^{\frac{2}{3}} - 1 \right]^2 \left[\left(4\frac{V_0}{V} \right)^{\frac{2}{3}} - 6 \right]^2 \right\} \end{aligned} \tag{2.47}$$

and the related pressure $P(V)$ is given by

$$P(V) = \frac{3B}{2} \left[\left(\frac{V_0}{V} \right)^{\frac{7}{3}} - \left(\frac{V_0}{V} \right)^{\frac{5}{3}} \right] \left\{ 1 + \frac{3}{4}(B_0' - 4) \left[\left(\frac{V_0}{V} \right)^{\frac{2}{3}} - 1 \right] \right\} . \tag{2.48}$$

where V_0 is the equilibrium volume, V is the deformed volume, and B_0' is the derivative of the bulk modulus with respect to pressure. The value of B_0' is almost constant for many substances [132].

2.8.2 Elastic Constants

There are two standard methods for calculating the elastic constants from *ab initio* calculations. One is the energy-strain method and another is the stress-strain method. In this thesis, we employed the energy-strain method where one calculate the total energy as a function of the applied strain [130]. The applied strains are chosen at constant volume as the total energy depends on the volume much more strongly than on strain. We denote by $e_1, e_2, ..., e_6$ the elements of the stain matrix $D(e)$ which transforms the lattice A with basis vectors x, y, z into the deformed lattice A' with basis vector x', y', z', i.e.

$$\begin{pmatrix} x' \\ y' \\ z' \end{pmatrix} = (D(e)+I)\begin{pmatrix} x' \\ y' \\ z' \end{pmatrix} = \begin{pmatrix} (1+e_1)x & \frac{1}{2}e_6 y & \frac{1}{2}e_5 z \\ \frac{1}{2}e_6 x & (1+e_2)y & \frac{1}{2}e_4 z \\ \frac{1}{2}e_5 x & \frac{1}{2}e_4 y & (1+e_3)z \end{pmatrix} \tag{2.49}$$

where I is the 3×3 identity matrix. In practice, the $e_1, e_2, ..., e_6$ are expressed in terms of δ so that the energy change upon strain is written as

$$E(e_1, e_2, ..., e_6) = E(0) + \frac{1}{2}V \sum_{i,j=1,6} c_{ij} e_i e_j + O(\delta^3) \tag{2.50}$$

where c_{ij}s are the elastic constants. In general the Eq. 2.50 becomes

$$E(\delta) = E(0) + VC\delta^2 + O(\delta^3) \tag{2.51}$$

where C is the particular combination of elastic constants which is obtained by fitting $E(\delta)$ by a polynomial of δ

$$C = \frac{C_2}{V} \tag{2.52}$$

where C_2 is the second order coefficient of the polynomial [130]. In the next subsection we show the expressions for the relevant elastic moduli for cubic lattices only, as we have computed the elastic moduli for systems with cubic symmetry in this thesis.

2.8.2.1 Elastic moduli in a cubic lattice

For a cubic lattice there are three independent elastic constants C_{11}, C_{12} and C_{44}. The corresponding strains are given in the Table 2.1. The compliances of the cubic phase can be obtained from the elastic constants using the following relations:

$$\begin{aligned} S_{44} &= \frac{1}{C_{44}}, \\ S_{11} - S_{12} &= \frac{1}{C_{11} - C_{12}}, \\ S_{11} + S_{12} &= \frac{C_{11}}{(C_{11} - C_{12})(C_{11} + C_{12})}, \end{aligned} \tag{2.53}$$

Table 2.1: Strain table for the calculation of elastic constants in the cubic systems. ΔE is the energy change upon strain and V is the equilibrium volume of the lattice.

Strain	Parameter	$\Delta E/V$
C1	$e_1 = e_2 = e_3 = \delta$	$\frac{3}{2}(C_{11} + 2C_{12})\delta^2$
C2	$e_1 = \delta, e_2 = -\delta, e_3 = \frac{\delta^2}{1-\delta^2}$	$(C_{11} - C_{12})\delta^2 + O(\delta^4)$
C3	$e_3 = \frac{\delta^2}{1-\delta^2}, e_6 = \delta$	$2C_{44}\delta^2 + O(\delta^4)$

Throughout this thesis, we have varied the strains from 0.00 to ±0.04 with intervals of 0.01 depending on the type of deformation and calculated total energies for monoclinic and orthorhombic deformations. The elastic moduli (C$_{11}$, C$_{12}$ and C_{44}) are then obtained by fitting the variation of total energies on the respective strain tensors to a 4th order polynomial equation. In the cubic lattice, the bulk modulus (B) is defined by $B = \frac{1}{3}\left(C_{11} + 2C_{12}\right)$. The bulk modulus can be calculated in several ways [133, 134]. In this thesis, we have used the Birch-Murnaghan equation of state as described in subsection 2.8.1. The shear elastic modulus (C$'$) is defined by C$' = \frac{1}{2}\left(C_{11} - C_{12}\right)$. For mechanical stability in the cubic lattice, the conditions are

$$C_{44} > 0, \quad C_{11} > |C_{12}|, \quad C_{11} + 2C_{12} > 0 \tag{2.54}$$

Apart from these elastic constants which are the ones in a single crystal, other elastic moduli are relevant when the material is polycrystalline. In a polycrystalline material, the single-crystal grains are randomly oriented. On a large scale, such materials can be considered to be quasi-isotropic or isotropic in a statistical sense. So suitable averaging methods based on statistical mechanics are needed to calculate the polycrystalline elastic moduli. There are two approximation methods to derive the isotropic elastic modulus for polycrystalline material. They are the Voigt [135] and Reuss [136] averaging methods, which represent the upper and lower bounds respectively of the isotropic elastic modulus. As there are only three independent elastic constants in the cubic crystal, the bulk modulus and the shear modulus in the Voigt method are

$$\begin{aligned} B_V &= \frac{C_{11} + 2C_{12}}{3}, \\ G_V &= \frac{C_{11} - C_{12} + 3C_{44}}{5} \end{aligned} \tag{2.55}$$

and the corresponding ones in Reuss method are

$$
\begin{aligned}
B_R &= \frac{1}{3(S_{11}+2S_{12}}, \\
G_R &= \frac{5}{S4_{11}-4S_{12}+3S_{44}}
\end{aligned}
\tag{2.56}
$$

respectively. Finally, the bulk modulus(B) and shear modulus(G) are the average of Voigt and Reuss elastic moduli based on Hill approximation [137, 138] which are expressed as following:

$$B = \frac{1}{2}(B_R + B_V), \tag{2.57}$$

and

$$G = \frac{1}{2}(G_R + G_V), \tag{2.58}$$

The ratio of shear modulus(G) and bulk modulus(B) of the polycrystalline phase (G/B) proposed by Pugh [139] is well correlated with hardness of the material [134, 140].

2.9 Calculation of the magnetic exchange interactions and the magnetic transition temperatures

Since the materials considered in this thesis are magnetic, computations of their magnetic properties constitute a significant part. In this section, we present methods that are used in this thesis to compute the magentic exchange interactions and the Curie temperatures (T_c).

2.9.1 The magnetic exchange interactions (J_{ij})

The magnetic pair exchange parameters are computed in order to understand the nature of the magnetic interactions of the systems studied in this thesis. They are efficiently calculated using the multiple-scattering Green's function formalism as implemented in the SPRKKR code [141]. In this approach, the spin part of the Hamiltonian is mapped to a Heisenberg model:

$$H = -\sum_{\mu,\nu}\sum_{i,j} J_{ij}^{\mu\nu}\mathbf{e}_i^{\mu}.\mathbf{e}_j^{\nu} \tag{2.59}$$

μ, ν represent different sublattices; i, j represent atomic positions; and $\mathbf{e}_i^{\mu}$ denotes the unit vector along the direction of magnetic moment at site i belonging to sublattice μ. The $J_{ij}^{\mu\nu}$ are magnetic exchange interactions which are computed from energy difference due to the small orientation of a pair of spins resulting a perturbation in spin-density which within the formulation of Lichtenstein *et al.* [142], based on magnetic force theorem [143] takes the following form

$$J_{ij} = \frac{1}{4\pi}\int_{-\infty}^{E_F} d\epsilon \,\mathrm{Im}\,\mathrm{Tr}(\Delta_\mathrm{i}\hat{\mathrm{T}}_{\sigma}^{\mathrm{ij}}\Delta_\mathrm{j}\hat{\mathrm{T}}_{\sigma\prime}^{\mathrm{ji}}) \tag{2.60}$$

where Δ_i= ($\hat{t}_{i\sigma}^{-1}$-$\hat{t}_{i\sigma\prime}^{-1}$), σ is the spin index, $\hat{t}$ is the single scattering matrix and $\hat{T}$ is the scattering path operator related to the off-diagonal elements of the Green's function. Tr is the trace over the orbital indices of the scatting matrix. Positive (negative) values for J$_{ij}$ indicate ferromagnetic (antiferromagnetic) coupling between atoms i and j.

2.9.2 The Curie temperature (T$_c$)

The Curie temperature (T$_c$) is estimated using the J$_{ij}$. We have used two different approaches to calculate T$_c$; the mean field approximation (MFA) [144] and the Monte Carlo simulations (MCS) [145] in order to check the qualitative consistency in the results and to obtain a reliable estimate of the quantity as the MFA is known to overestimate T$_c$ while the MCS method is more accurate quantitatively.

2.9.2.1 Mean field approximation (MFA)

The Curie temperature within the mean field approximation for a multi-sublattice material can be obtained by solving the system of coupled equations [144, 146, 147]

$$\langle \mathbf{e}^{\mu}\rangle = \frac{2}{3k_BT}\sum_{\nu} J_0^{\mu\nu}\langle \mathbf{e}^{\nu}\rangle \tag{2.61}$$

where $\langle \mathbf{e}^{\nu} \rangle$ is the average Z component of $\mathbf{e}_i^{\nu}$ and $\mathrm{J}_0^{\mu\nu} = \sum_i J_{0i}^{\mu\nu}$. Eq. 2.61 can be expressed in the form of an eigenvalue matrix problem

$$(\mathbf{\Theta} - T\mathbf{I})\mathbf{E} = 0 \tag{2.62}$$

where $\Theta_{\mu\nu} = \frac{2}{3k_B T} J_0^{\mu\nu}$, $\mathbf{I}$ is a unit matrix and $\mathbf{E}$ is the vector of $\langle \mathbf{e}^{\nu} \rangle$. The largest eigenvalue of matrix $\mathbf{\Theta}$ determines the value of the Curie temperature [144].

2.9.2.2 Monte Calro simulation (MCS)

In this subsection, we describe the Monte Carlo method for calculating the Curie temperature. The problems using Monte Carlo method [148] are solved in a stochastic manner which depends on a sequence of random numbers, generated during the simulation. This method is widely used in the statistical physics where systems deal with many degrees of freedom. A typical problem posed by statistical physics is to compute average macroscopic observables of a system for which the Hamiltonian is assumed to be known. For instance, we have considered the Heisenberg model and the corresponding Hamiltonian is given in Eq. 2.59. In this model, $\mathbf{e}_i = (e_i^x, e_i^y, e_i^z)$ is a classical Heisenberg spin variable and $|\mathbf{e}_i| = 1$ at lattice site i.

The physical properties computed from the model Hamiltonian H are the average energy E and average magnetization M per site at a given temperature T,

$$E = \langle H \rangle_T / N, \quad M = \langle \sum_i \mathbf{e}_i \rangle_T / N \tag{2.63}$$

where N is the number of sites.

In the MC simulations, the initial spin states are randomly sampled and the acceptance or rejection of the spin states is determined by Metropolis algorithm [149]. For a given site, the components of new spin state are then randomly chosen in the following manner [145]; two random numbers r_1 and r_2 are chosen in the interval of [0, 1] to produce a vector with two components $\xi_1 = 1 - 2r_1$ and $\xi_2 = 1 - 2r_2$. The length of the vector is determined by $\xi^2 = \xi_1^2 + \xi_2^2$ and if $\xi^2 < 1$, then the new spin components are $e^x = 2\xi_1\sqrt{1-\xi^2}$, $e^y = 2\xi_2\sqrt{1-\xi^2}$ and $e^z = 1 - \xi^2$. After selecting the new spin components, we calculate the change in energy (ΔE) of the system. If ΔE is negative then the new spin state is accepted and if not then the new spin state is accepted with probability $e^{-\Delta E/k_B T}$. The above procedure is continued for all the sites and when all the sites are covered, one Monte Carlo step is finished. The system is evolved using MC algorithm for several MC steps till the system reaches equilibrium when the total energy of the system does not change significantly with MC step. Then the statistics are calculated from the significant number of configurations. The total magnetization is calculated from the Eq. 2.63 and the Curie temperature is estimated from the susceptibility, defined as [147, 150]

$$\chi = \frac{1}{N}\sum_{i}^{N}\frac{\langle M^2\rangle - \langle M\rangle^2}{k_B T} \tag{2.64}$$

For the above calculations, we have used the magnetic exchange interaction ($J_{ij}^{\mu\nu}$), calculated using SPRKKR code [126], as described in subsection 2.9.1.

2.10 Calculation of phonon dispersion relations

We have calculated the phonon dispersion relations for few systems discussed in this thesis by the direct method [151–153] as implemented in the PHON [154] package. The "direct method" relies on modeling specific phonon wave vector by construction of supercells, computation of forces on each atom by displacing it, and obtaining the dynamical matrix by the finite difference method.

Let us consider a lattice, where the translation form one point to another is defined by a translation vector

$$\mathbf{r}_l = l_1\mathbf{a}_1 + l_2\mathbf{a}_2 + l_3\mathbf{a}_3 \tag{2.65}$$

where $\mathbf{a}_1$, $\mathbf{a}_2$ and $\mathbf{a}_3$ are the primitive translation vectors of the lattice and l_1, l_2 and l_3 are arbitrary integer. If there are n number of atoms in the unit cell, labelled by $k = 1, ..., n$, then the positions of these n atoms with respect to the origin [$\mathbf{r}_l$; $l = (0, 0, 0)$] of the unit cell are given by the vectors $\mathbf{r}_k$. Therefore, in general the position of kth atom in the lth primitive cell is given by

$$\mathbf{r}_{lk} = \mathbf{r}_l + \mathbf{r}_k \tag{2.66}$$

The atoms are displaced from their equilibrium positions when the system undergoes vibration. If the atoms are allowed to move from their equilibrium positions by an amount $\mathbf{u}_{lk} = (u_{lk_x}, u_{lk_y}, u_{lk_z})$ then the actual position of any atom under

---

The detailed calculations of phonon dispersion relation are described in "http://cmt.dur.ac.uk/sjc/thesis/thesis/node52.html" the influence of a vibration is $\mathbf{R}_{lk} = \mathbf{r}_{lk} + \mathbf{u}_{lk}$. Therefore, the potential energy of the crystal is a function of the instantaneous coordinates $\mathbf{R}_{lk}$ of the atoms. If the displacements are assumed to be small then the potential of the crystal can be expanded about the equilibrium positions

$$\phi = \phi_0 + \sum_{lk\alpha} \phi_{lk_\alpha} u_{lk_\alpha} + \frac{1}{2} \sum_{lk\alpha, l'k'\beta} \phi_{lk_\alpha, l'k'_\beta} u_{lk_\alpha} u_{l'k'_\beta} + ... \tag{2.67}$$

where α and β are the cartesian coordinates and the coefficient ϕ_{lk_α} and $\phi_{lk_\alpha, l'k'_\beta}$, are

$$\phi_{lk_\alpha} = \left(\frac{\partial \phi}{\partial u_{lk_\alpha}} \right)_0 \tag{2.68}$$

and

$$\phi_{lk_\alpha, l'k'_\beta} = \left(\frac{\partial^2 \phi}{\partial u_{lk_\alpha} \partial u_{l'k'_\beta}} \right)_0, (lk) \neq (l'k') \tag{2.69}$$

The subscript '0' means that the derivatives are evaluated at the equilibrium position, $\mathbf{r}_{lk}$. The force on the atom is then given by

$$F_{lk_\alpha} = -\frac{\partial \phi}{\partial u_{lk_\alpha}} \tag{2.70}$$

The first term in the series (Eq. 2.67) is constant as is independent of the displacements of the atoms from their equilibrium positions. The contribution to the force from the second term is also zero as there are no forces on any atom at equilibrium. In the harmonic approximation, the cubic and higher order terms are assumed to be negligible. Therefore, the potential can be expressed simply as the third term of the expansion. So, in the harmonic approximation, the force exerted on the atom at position $\mathbf{R}_{lk}$ is

$$F_{lk_\alpha} = -\sum_{l'k'_\beta} \phi_{lk_\alpha, l'k'_\beta} u_{l'k'_\beta} \tag{2.71}$$

The coefficient, $\phi_{lk_\alpha, l'k'_\beta}$ is calculated by the small-displacement method [155]. The equation of motion can be expressed as

$$M_k \ddot{u}_{lk_\alpha} = \sum_{l'k'_\beta} \phi_{lk_\alpha, l'k'_\beta} u_{l'k'_\beta} \tag{2.72}$$

where M_k is the mass of the kth atom. The Eq. 2.72 is a set of coupled equations and it can be solved by considering a wave-like solution

$$u_{lk_\alpha} = \frac{1}{\sqrt{M_k}} e_{k_\alpha}(\mathbf{q}) \exp[i\mathbf{q} \cdot r_{lk} - \omega(\mathbf{q})t] \tag{2.73}$$

where, $e_{k_\alpha}(\mathbf{q})$ is the amplitude of the wave and $\mathbf{q}$ is the wavevector. The substitution of Eq. 2.73 into Eq. 2.72 leads to the following dispersion relation

$$\omega^2(\mathbf{q})e_{k_\alpha} = \sum_{k'_\beta} D_{\alpha\beta}\begin{pmatrix}\mathbf{q}\\ kk'\end{pmatrix} e_{k_\beta} \tag{2.74}$$

where D is known as the dynamical matrix. The elements of D are given by

$$D_{\alpha\beta}\begin{pmatrix}\mathbf{q}\\ kk'\end{pmatrix} = \frac{1}{\sqrt{M_\alpha M_\beta}} \sum_{l'} \phi_{lk_\alpha, l'k'_\beta}) \exp[i\mathbf{q} \cdot (\mathbf{r}_{l'k'} - \mathbf{r}_{lk})] \tag{2.75}$$

The dynamical matrix D is a $3n \times 3n$ Hermitian matrix. In case of solids, there are n number of atoms followed by 3n number of linear homogeneous equations. For non-trivial solution of these system of equations, the determinant of the coefficients in Eq. 2.74 must be zero. This is set as

$$\left| D_{\alpha\beta}\begin{pmatrix}\mathbf{q}\\ kk'\end{pmatrix} - \delta_{\alpha\beta}\delta_{kk'}\omega^2(\mathbf{q}) \right| = 0 \tag{2.76}$$

Therefore, the eigenvalues of the dynamical matrix yield phonon frequencies for a given $\mathbf{q}$. As the dynamical matrix is Hermitian, the eigenvalues, $\omega(\mathbf{q}, \mathbf{k})$ are real.

2.11 Summary

In this chapter, we have briefly described the state-of-the-art computational techniques used in condensed matter physics, i.e., DFT based methods, for the simulations of the materials which I have investigated. We have extensively used two different implementations of DFT, (i) PAW method as implemented in the VASP (ii) Full potential KKR method as implemented in the SPRKKR package.

Chapter 3

Investigation of the modulated martensites in Mn_2NiGa

3.1 Introduction

The modulated martensitic structures are one of the prerequisites for the observation of large reversible MFIS. These modulated structures evolve when the high-temperature, high-symmetry cubic structure phase transforms to low-temperature, low-symmetry structures in a diffusionless way [156]. The modulated martensites can be commensurate and incommensurate orthorhombic or twinned monoclinic structures [157–162]. The phases exhibit a high mobility of particular twin boundaries [163, 164], which can even be driven in moderate magnetic fields and a low hysteresis which makes them appealing as smart materials for actuator and sensor applications. This is believed to be a consequence of the formation of a hierarchical martensitic microstructure, which involves twinning of twinned or modulated structures, spanning several length scales [165–167].

A volume of work has been done on Ni-excess Ni-Mn-Ga system, often in the stoichiometric composition of 2:1:1, to understand the origin of these modulated structures. One line of thought considers solely the softening of a particular vibrational mode at a specific wave vector, due to Fermi surface nesting, as the origin of the modulated phases, which are shearing of lattice planes within the equilibrium martensite phase [168, 169]. In contrast, the concept of adaptive martensites [170] considers the modulated structures, instead of being equilibrium structures, as metastable microstructures of the nonmodulated (NM) martensite. Both concepts gained significant currency due to corroborations by theoretical calculations

---

The contents of this chapter are published in Physical Review B **96**, 064107 (2017) and experimental observations, e.g., for the case of stoichiometric and Ni-excess Ni-Mn-Z systems [166, 171–175]. Very recently, an attempt has been made to unify the opposing lines of thought [176]. Nevertheless, the fundamental understanding of the modulated phases can only be considered complete if the underlying concepts can be applied to a broader set of systems. Subsequently, Mn_2NiGa has been investigated highlighting this perspective. A seven-layered monoclinic modulated structure was observed at room temperature in the powder x-ray diffraction study of Mn_2NiGa [68]. It was observed that the structure of the martensitic variant is quite sensitive to the residual stress in the system. Recent neutron diffraction study of Mn_2NiGa has also reported a seven-layered orthorhombic modulated structure at low temperature [69]. The handful of experimental results and the signatures obtained from the DFT calculations thus call for a detailed investigation into the energy landscape to understand and interpret the origin and stabilities of different modulated structures in the martensite phase of Mn_2NiGa. Such an investigation is required since the efficiency of MFIS and MCE depend substantially on the structures in the martensite phases for MSM systems. Such a study would also provide further insights into the mechanism of the martensitic phase transformation in Ni-Mn-Ga systems and put the research on understanding of the modulated structures in Heusler MSM compounds in a broader perspective.

In this chapter, we therefore investigate the structural properties and relative stabilities of different modulated structures of Mn_2NiGa and make an attempt to understand the origin of the sequences of structural phases as the system is driven from high-temperature cubic to low-temperature NM tetragonal variant. Comparisons with Ni_2MnGa are made in order to understand the physical mechanism. Using DFT calculations, we first perform an elaborate study of the structural properties of the various crystalline phases. We discuss the results on the sequences of various phases and their relative stabilities from their electronic structures. The origin of the modulated structures is explained from the phonon dispersions, the features in the Fermi surfaces, and the electronic susceptibilities.

3.2 Computational Details

Electronic structure calculations were performed with the spin-polarized density functional theory (DFT) based projector augmented wave method [120] as implemented in the Vienna *ab initio* Simulation Package (VASP) [177, 178]. For all calculations, we have used the PBE-GGA functional [179] for exchange and correlation parts in the Hamiltonian. A high kinetic energy cutoff of 750 eV was used for all calculations to address the small energy difference between different modulated structural phases. For Ga, the 3*d* electrons were included in the valence band. The Brillouin zone was sampled by the Monkhorst-Pack [180] *k*-point generation scheme with a uniform 21x21x21 *k*-point mesh for the cubic structure, a 12x4x8 mesh for 6M modulated structures, and a 10x2x8 mesh for 10M and 14M modulated structures, after careful convergence tests (The modulated structures are shown in Fig. 3.1). The total energy convergence criteria were set to 10^{-5} eV and the force convergence criteria were set to 10^{-2} eV/Å.

Phonon dispersion relations were calculated with the direct method as implemented in the PHON package [154]. A 4x4x4 supercell containing 256 atoms with a small atomic displacement of 0.02 Å was used to calculate the force constant matrices. An energy cut-off of 500 eV and a 2x2x2 *k* mesh were used for the calculations of forces.

Fermi surfaces and generalized susceptibilities were obtained from electronic structure calculations. As for the total energy calculations, we employed the VASP code using the PBE functional and the tetrahedron method for the integration over a dense Γ-centered *k*-mesh containing $75 \times 75 \times 75$ points in the full Brillouin zone (9880 in the irreducible part). This dense mesh was used in the self-consistency cycle to determine charge distribution and eigenvalues which are required to be significantly more accurate than in previous calculations of the Fermi surfaces of Ni_2MnGa obtained by a similar procedure [181, 182]. The *k*-dependent eigenvalues were processed by a script written for the computer algebra system Mathematica. The script unfolds the irreducible part of the Brillouin zone and determines the Fermi surface as the cross section at the Fermi level of the four-dimensional energy in reciprocal space, interpolated by cubic splines. The real part of the generalized susceptibility was obtained from the same quantity in the way described in Sec. 3.3.4.

3.3 Results and Discussions

3.3.1 Structural properties of cubic, non-modulated, and different modulated phases

In this subsection, we present detailed results on the structural parameters of the different phases of Mn_2NiGa at different temperatures. The high-temperature phase of this system, like Ni_2MnGa, is a variant of the $L2_1$ structure. Experimental results

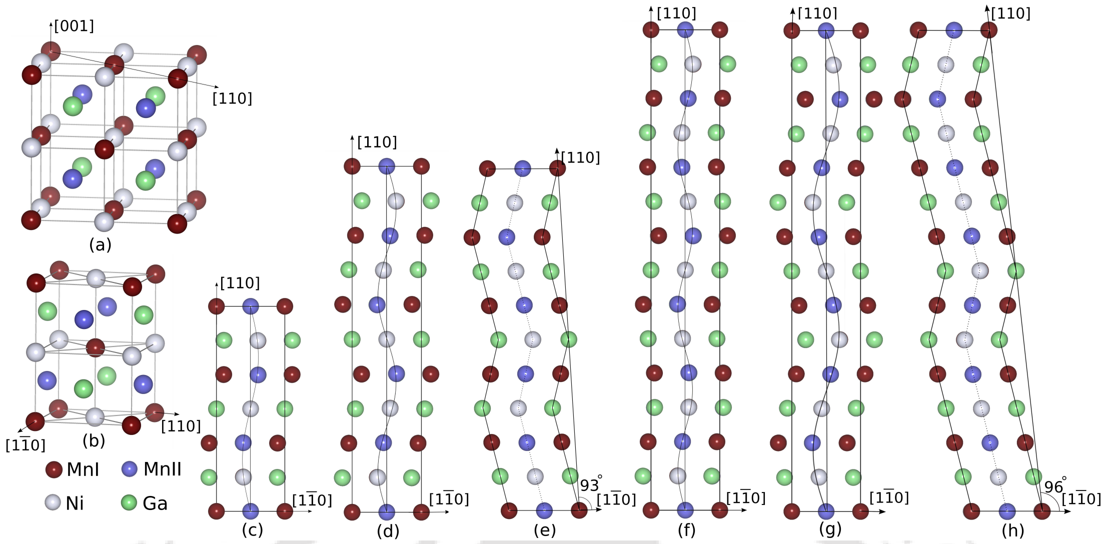

Figure 3.1: (a) Cubic Hg_2CuTi structure of Mn_2NiGa ; (b) Non modulated tetragonal ($L1_0$)structure; (c) 6M structure; (d) 10M structure; (e) 10M$(3\bar{2})_2$ structure; (f) 14M$_{3/7}$ structure; (g) 14M$_{2/7}$ structure (h) 14M$(5\bar{2})_2$ structure for the martensitic phase.

[64, 65, 68] and theoretical calculations [66, 77, 86] have confirmed that the the high-temperature, high symmetry structure of Mn_2NiGa alloy is the Hg_2CuTi structure or inverse Heusler structure. The corresponding structure is shown in Fig. 3.1(a). The equilibrium lattice constant is determined by calculating the total energy as a function of lattice parameters and then by fitting the results to the Murnaghan equation of state. Our calculated lattice constant a=5.84 Å is within 1% with the experimental lattice constant a=5.907 Å [64] and shows excellent agreement with other theoretical results [66, 77, 86].

Liu *et al.* first reported the shape memory behavior in Mn_2NiGa and observed a martensitic transformation around room temperature [64, 65]. From the x-ray diffraction pattern in the system, they concluded that the low-temperature structure is a nonmodulated(NM) tetragonal structure, as shown in Fig. 3.1(b). In order to verify this, we tetragonally distort the cubic structure, keeping the volume constant at the equilibrium volume of the high-temperature structure, and compute the total energy as a function of the tetragonal distortion provided by the value of c/a. The total energy curve of Mn_2NiGa consists of two minima, one shallow at $c/a = 0.93$ and another deep at $c/a = 1.28$, as shown in Fig. 3.3. The energy difference between the cubic($c/a = 1.0$) and NM tetragonal structure at $c/a = 0.93$ is about 3 meV/atom whereas that value for $c/a = 1.28$ is about 28 meV/atom. Our calculated values of the c/a and the energy differences are in good agreement with a previously reported result [77]. This, thus is in agreement with the experimental observations from the x-ray diffraction data. However, the presence of a meta-stable minimum for $c/a < 1$ indicates that other martensitic NM structures may be present in Mn_2NiGa. A similar feature has also been reported for the related isoelectronic compound Mn_2PtGa [183]. For Ni_2MnGa, a stable phase with $c/a < 1$ could only be obtained in DFT calculations by shuffling the atomic planes resulting in modulated structures, such as 6M, 10M, and 14M, which differ from one another by the period of modulations [159–161, 184–187]. It has also been observed that the existence of a particular modulated structure in Ni-Mn-Ga system depends on the relative concentrations of the three constituents and also on the resolution of the diffraction technique [161].

The results above and the observation of a 14M monoclinic modulated structure by Singh *et al.* [68] and a 14M orthorhombic modulated structure by Brown *et al.* at low temperature [69] in Mn_2NiGa show that there can be several modulated structures in this system, depending on the periodicity of the modulations and/or the stacking sequences of atomic layers. Accordingly we perform detailed computations of the structural aspects of different modulated structures of Mn_2NiGa, with orthorhombic and monoclinic lattice parameters. In what follows, we present results on pseudotetragonal 6M, 10M, and 14M modulated structures with orthorhombic lattice parameters originating from wavelike modulations, and on 10M and 14M modulated structures with monoclinic symmetry originating from stacking sequences.

The 10M structure in Ni_2MnGa is probably the most studied modulated martensite in terms of atomistic simulations (see, e.g., Refs. [176, 184, 185, 187–193]). Experimentally, the 10M of Ni_2MnGa is frequently reported as an incommensurate modulation [159, 161, 162, 186, 194], e. g, its period does not amount to exactly 10 lattice planes, but there is some notable deviation leading to irrational wave vectors, which is difficult to model accurately, as it requires large supercells [195, 196]. An incommensurate modulation is straightforwardly explained in terms of a soft phonon mode arising from an electronic instability at the Fermi surface (which can lead to arbitrary wave vectors), instead of a twinned microstructure. But there is an ongoing discussion, as to whether a statistically perturbed stacking sequence might alternatively explain the experimental observation [162, 176, 197, 198]. Since the differences in total energy are expected to be rather small, it is very difficult to accurately predict incommensurate modulations from atomistic calculations. Therefore, we will concentrate, as most theoretical approaches up to now, on the paradigmatic commensurate modulations ubiquitous in literature, like 6M, 10M and 14M. These will be considered alternatively as sinusoidal modulations confined in a orthorhombic

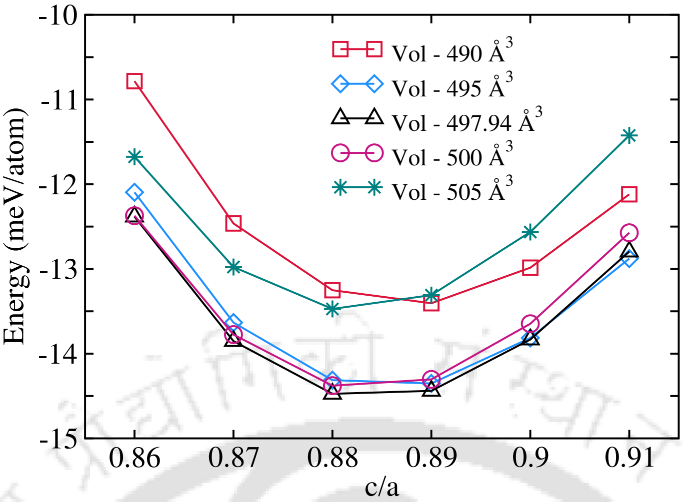

Figure 3.2: The total energies of pseudo-tetragonal 10M structure (with orthorhombic lattice parameters) relative to the cubic Hg_2CuTi structure, as a function of c/a ratio for five different volumes: 490 Å^3, 495 Å^3, 497.94 Å^3(equilibrium volume of cubic structure), 500 Å^3 and 505 Å^3.

cell and as nano-twinned structures with fully optimized monoclinic lattice parameters.

Although no report on the existence of a 10M structure is available for Mn_2NiGa, we performed structural optimization and total energy calculation for this structure. Following Zayak *et al.* [184], we constructed a $1 \times 5 \times 1$ supercell of a body- centered tetragonal (bct) structure, generated from the high-temperature cubic structure. The supercell, shown in Fig. 1(d), contains 40 atoms. The modulation was incorporated by shuffling the (110) atomic planes along $[1\bar{1}0]$ direction, thus including two sine periods in the ten atomic layers along [110]. An initial displacement of 0.2 Å was chosen for both Ni-Mn and Mn-Ga atomic planes.

We optimized the atomic positions of 10M structure for different volumes around the equilibrium volume of the high-temperature phase, by keeping the shape of the cell fixed, thus representing the pseudotetragonal or orthorhombic structure. The results of total energies for different volume of the 10M structure are shown in Fig. 3.2. We obtained an energy minimum at $c/a = 0.88$. From Fig. 3.2, it is observed that the c/a ratio does not change much with the volume of the cell. Therefore, in order to investigate the volume change, we have calculated the total energies at different volumes, but with the c/a ratio at a constant value of 0.88. We obtained a volume change of 0.05% for the 10M structure, (Table 3.1). After atomic relaxation the structure preserves the wavelike modulation with modulation amplitude 0.565 Å for the Mn-Ni plane and 0.554 Å for the Mn-Ga plane.

Table 3.1: The calculated lattice parameters of Mn_2NiGa in cubic Hg_2CuTi-type, NM tetragonal($L1_0$), 6M, 10M and 14M structures with wavelike modulation. For the pseudo-tetragonal 6M, 10M and 14M, the orthorhombic lattice parameter b is fixed as $3 \times a$, $5 \times a$, and $7 \times a$, respectively, while the ratio c/a_0 is calculated from $a_0 = \sqrt{2}\,a$ allowing direct comparison with the cubic case where $c/a = 1$.

	Lattice parameter			
Structure	a (Å)	c (Å)	c/a_0	$\Delta V/V(\%)$
Cubic	5.84(5.90)	5.84	1.00	0.00
6M	4.29	5.40	0.89	0.22
10M	4.30	5.36	0.88	0.05
$14M_{3/7}$	4.29	5.40	0.89	0.22
$14M_{2/7}$	4.31	5.36	0.88	0.05
Tetragonal	3.80	6.88	1.28	0.65
14M[expt.] [69]	4.172	5.336	0.90	

In order to benchmark our technical settings, we also calculated the structural parameters of the 10M Ni_2MnGa structure using the same approach. We obtained an energy minimum at $c/a = 0.92$ with a modulation amplitude of 0.332 Å for the Mn-Ga planes and 0.363 Å for the Ni planes. The obtained c/a ratio of the 10M structure for Ni_2MnGa is consistent with other theoretical results [184, 187, 192]. The optimized modulation amplitudes in our calculation are slightly larger than those reported by Zayak *et al.*. This could be due to the c/a ratio of 0.92 obtained in our calculations which is smaller than the value 0.955 used by Zayak *et al.* [184] according to the linear relationship of modulation amplitude with the c/a ratio [187].

Next, we investigated the 6M and 14M structures with orthorhombic symmetry for Mn_2NiGa. The 6M and 14M structures were constructed by 1 x 3 x 1 and 1 x 7 x 1 supercells of the bct structure as shown in Figs. 3.1(c), (f) and (g), respectively. The 6M and 14M structures contain 24 and 56 atoms, respectively, in the unit cell. For the 6M structure, one period was fitted into six atomic planes. For the 14M structure, two possible kinds of modulations are reported in the context of Ni_2MnGa: (1) two periods fitted into 14 atomic planes, referred to as $14M_{2/7}$[see Fig. 3.1(f)] [160] and (2) three periods fitted into 14 atomic planes, referred to as $14M_{3/7}$[see Fig. 3.1(g)] [186]. In the absence of any experimental information on the nature of the 14M modulation in this system, we considered both types of 14M modulations in our work. The optimized lattice parameters for all the structures considered are given in Table 3.1. The modulation amplitudes of the 6M, $14M_{3/7}$, and $14M_{2/7}$ structures are 0.506 Å, 0.5 Å and 0.52 Å, respectively, for Mn-Ni planes and 0.492 Å, 0.481 Å and 0.507 Å, respectively, for Mn-Ga planes. Our calculated structural parameters of different modulated structures and the NM tetragonal structure are within 2-3 % of the available experimental lattice parameters [64, 69].

We next calculated the structural parameters of 10M and 14M modulated structures by allowing full monoclinic variation of the constructed supercells. The monoclinic structures are obtained by displacing the atomic layers in a different manner on top of the periodic modulations. For the 10M structure, three atomic planes are shifted in one particular direction while two atomic planes are shifted in the opposite direction, generating a $(3\bar{2})_2$ stacking sequence [Fig. 3.1(e)]. In the case of the 14M structure, the $(5\bar{2})_2$ stacking sequence was chosen, as shown in Fig. 3.1(h). These $(3\bar{2})_2$ and $(5\bar{2})_2$ stacking sequences are usually considered for 10M and 14M structures, respectively [185, 197], although Zayak *et al.* [185] showed that a different sequence can also be stabilized for Ni_2MnGa. In the case of Mn_2NiGa, the initial shifts of the planes were chosen from the experimentally reported monoclinic angle $\beta = 93.1°$ for a 14M structure, although there is no result reported about the stacking of atomic planes [68]. Thus, the initial shift of the two consecutive lattice planes was taken to be 0.356Å in our calculations. The structures were relaxed with respect to the ionic positions, and the shape and volume of the supercells. The relaxed structural parameters for these two structures are given in Table 3.2. Our calculated lattice parameters for the 14M structure have small differences with the experimentally reported parameters for Mn_2NiGa. This difference might be due to the presence of extra 3.5% Mn content in the experimental sample [68] or might be due to the stacking sequence we chose in our calculations.

The (c/a) ratio in the martensitic phase is related to the maximum theoretically achievable MFIS as $|1 - c/a|$. In case of Ni-rich Ni-Mn-Ga, the experimental MFIS value was found to be almost close to the theoretical maximum MFIS for 10M (c/a≈0.94) and 14M (c/a≈0.90) structures. From the results on the structural parameters, we conclude that for Mn_2NiGa, the maximum achievable MFIS for wavelike modulated structure is 11% (c/a≈0.89) and that for monoclinic structure is

Table 3.2: The calculated lattice parameters of Mn_2NiGa in 10M and 14M monoclinic structures with $(3\bar{2})_2$ and $(5\bar{2})_2$ stacking sequences, respectively.

	Lattice parameter				
Structure	a (Å)	b (Å)	c (Å)	γ in degree	$\Delta V/V(\%)$
$10M(3\bar{2})_2$	4.36	5×4.27	5.35	93.3	0.20
$14M(5\bar{2})_2$	4.36	7×4.27	5.36	96.3	0.34
14M[expt.] [68]	4.25	7×4.13	5.36	93.1	

13% (c/a≈0.87), both higher than those in Ni-rich Ni-Mn-Ga systems. To date, there is only one measurement of the MFIS in Mn_2NiGa available for comparison with our theoretical prediction reporting a 4% MFIS for the NM structure of Mn_2NiGa [64]. This should be compared with a maximum of 0.17% MFIS obtained in the NM tetragonal phase of Ni_2MnGa single crystals with composition ratio close to $2:1:1$ [199]. In Ref. [64], it was observed that the reported 4% MFIS was nonsaturating at a rather high magnetic field of 1.8 T. This raises the expectation that with sufficiently higher magnetic fields considerably larger MFIS may be obtained in Mn_2NiGa. In turn, experiments that observed modulated phases of Mn_2NiGa [68, 69] did not report MFIS. This is in contrast to the prototype Ni_2MnGa, where strain as large as nearly 10% was obtained for the 14M orthorhombic structure with a magnetic field of only 0.5 T [20, 21].

The larger MFIS obtained in the modulated martensite phases of Ni_2MnGa are attributed to the low twinning stresses in comparison to the magnetic stress due to the presence of adaptive modulations and mesoscopic twin boundaries [166, 172]. Consequently, their absence explains the larger twinning stress and low MFIS in the NM martensite phase of Ni_2MnGa [200, 201]. A recent work of Sozinov *et al.* [202], however, suggests that a MFIS, as large as 12% can be obtained in the NM martensite phase if the twinning stress can be lowered by lowering the tetragonal distortion, which was realized in off-stoichiometric samples after simultaneous codoping of Co and Cu. A similar strategy might be successful for Mn_2NiGa, as well, as the observed MFIS so far is already significantly higher than Ni_2MnGa. Detailed quantifications of twinned and magnetic stress are, however, beyond the scope of the present work.

3.3.2 Energetics of the modulated structures

Figure 3.3 shows the total energy curves, as a function of the tetragonality, denoted by the value of (c/a), for different modulated and the NM tetragonal structures of Mn_2NiGa considered here. The zero energy $(c/a = 1)$ in the NM curve corresponds to the high-temperature cubic structure. In case of the NM structure, two energy minima are observed; one corresponds to the lowest energy $L1_0$ structure at $c/a = 1.28$ and another corresponds to the aforementioned metastable minimum at $c/a = 0.93$. The modulated structures 6M, 10M, $14M_{3/7}$ and $14M_{2/7}$, obtained by shuffling lattice planes along the (110) directions in the cubic structure, have lower energies as is seen from the total energies of different modulated structures at $c/a = 1$ (Fig. 3.3). At $c/a = 1$, the 6M structure has the lowest energy, the

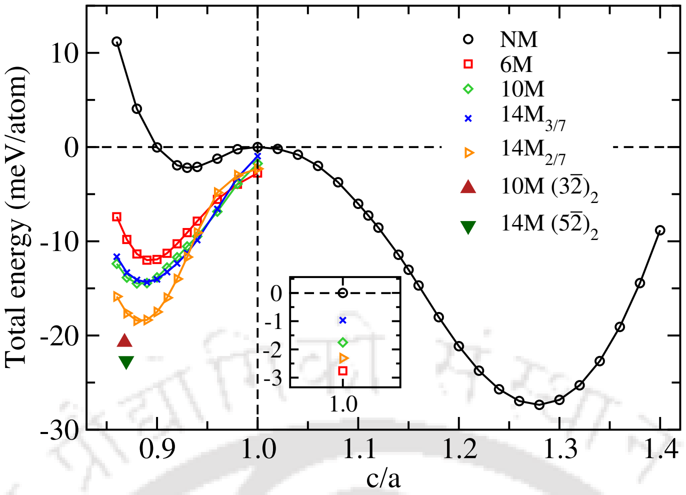

Figure 3.3: The variation of the total energy in NM tetragonal ($L1_0$) and in the different modulated structures of Mn_2NiGa as a function of the c/a ratio. The zero energy is taken to be the energy of the cubic Hg_2CuTi-type inverse Heusler structure. The energies of the pseudo-cubic structures (modulated structures inscribed in an orthorhombic cell with $c/a = 1$) are shown in the inset.

energy of the structure being lower by about 3 meV per atom with respect to that of the cubic structure. It is to be noted that for Ni_2MnGa, it was the 10M structure that had the lowest energy at $c/a = 1$ [193], while only the 6M has a metastable energy minimum close to the pseudocubic case [197]. After relaxation of the lattice parameters, while keeping the orthorhombic shape of the cell, all modulations gain significantly in energy by increasing the pseudotetragonal distortion. Therefore, we propose that a pseudocubic 6M premartensite would be unstable against further structural distortions. With the orthorhombic constraint for the simulation cell, the minimum energy state is obtained for the $14M_{2/7}$ modulation. This is in agreement with the results of Brown *et al.* obtained at low temperature [69]. Relaxations of the shapes of the cells convert the 10M and 14M pseudotetragonal structures to monoclinic $10M(3\bar{2})_2$ and $14M(5\bar{2})_2$ structures by lowering energies further (shown in Fig. 3.3 by filled triangles). Once again, the $14M(5\bar{2})_2$ structure has the lowest total energy, in agreement with the observation of a monoclinic 14M structure by Singh *et al.* [68]. The hierarchy of energetics for the nanotwinned structures with monoclinic symmetry is the same as obtained from DFT calculations for Ni_2MnGa [197]. However, there is a noticeable difference. For Ni_2MnGa, the energy difference between the relaxed 14M structure (the modulated structure with the lowest energy) and the NM tetragonal structure was nearly zero whereas in the present case of Mn_2NiGa, the difference is about 18 meV per formula unit, significantly larger than that in the case of Ni_2MnGa. This indicates a significant energy penalty associated with the formation of nanotwin interfaces in Mn_2NiGa as opposed to Ni_2MnGa, where this interface energy turns out to be very small. According to the concept of adaptive martensite of Khachaturian *et al.* [170], a large interface energy can effectively inhibit the formation of adaptive microstructures on the nanoscale. This may, however, be overcome by externally applied stress, which conforms with the experimental observation of Singh *et al.* [68] that the observation of modulated structures in Mn_2NiGa are dependent on the residual stress. Other experiments indicate the formation of secondary phases or precipitates depending on the annealing conditions [69, 203, 204]. Respective changes in local composition due to segregation and chemical disorder may alter the energy landscape considerably. For instance, it has been reported that at least the magnetic moments are significantly affected by chemical disorder and structural distortion [78, 205, 206].

Our present study is restricted to the case of single-phase, fully stoichiometric systems, where we can conclude from the $T = 0$ energy landscape that due to the lack of energy barriers aside from microstructure, the system should evolve downhill into a martensitic state with significant tetragonal or orthorhombic distortion along a comparatively steep transformation path, once a specific modulation is established. Thus, we interpret the absence of a corresponding energy minimum as the signature of prevention of the formation of a stable premartensite, in agreement with experiment. Further, once a modulation with tetragonal or orthorhombic lattice parameters is established, we can expect that it will subsequently transform into a nanotwinned monoclinic structure, according to the associated energy gain of 6 to 8 meV/atom. This structure consists of nonmodulated building blocks separated by atomically sharp twin boundaries. In Ni_2MnGa, the nonmodulated and nanotwinned arrangements are nearly degenerate, which effectively slows down the coarsening process [173, 176, 197]. In Mn_2NiGa, however, the system can gain further 5 to 7 meV/atom by eliminating the twin boundaries, which should speed up the kinetics of the transition to the $L1_0$ ground state significantly, such that nanotwinned structures might not become observable unless they are stabilized by external strain. A concrete prediction of temperature- and stress-induced transitions in terms of the free energy must be left open at this point, since this involves a computationally significantly more involved estimate of vibrational and magnetic entropy, which can play a decisive role at finite temperatures as shown previously for Ni_2MnGa [174, 207]. In the next subsection, we discuss the relative stabilities of different martensitic structures, as shown in Fig. 3.3 and Table 3.3 in terms of their

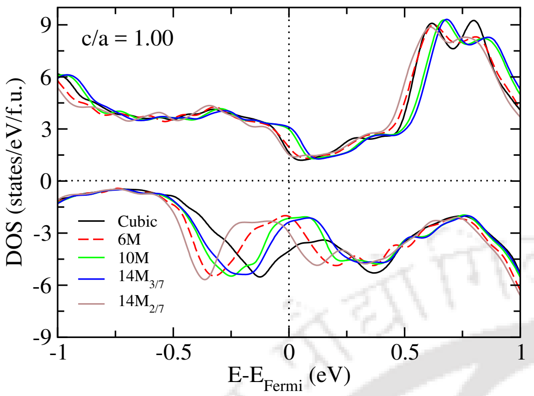

Figure 3.4: Total density of states of different pseudo-cubic modulated phases. The total density of states in the cubic structure is shown for comparison.

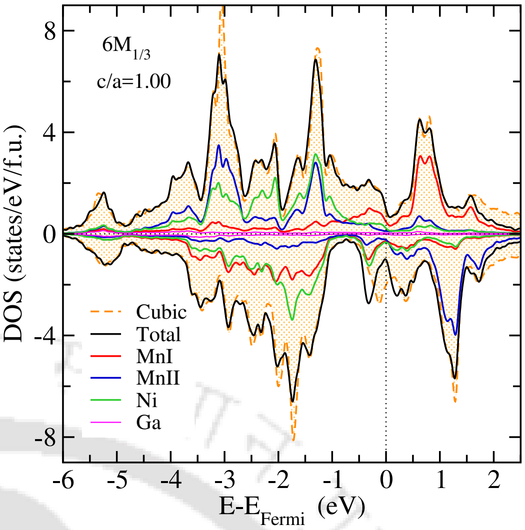

Figure 3.5: Total and atom projected density of states of Mn_2NiGa in the pseudo-cubic 6M modulated structure. The total density of states in the cubic Hg_2CuTi-type structure is shown for comparison.

electronic structures.

Table 3.3: The equilibrium energies (in meV per atom) of the NM tetragonal ($L1_0$) and different modulated structures relative to the energy of the high-temperature cubic phase. The zero energy is considered to be that of the cubic structure (A). The corresponding c/a ratios are given. For monoclinic structures, c/b ratios are given in parentheses.

	c/a_0	Energy(meV/atom)
E_{A-6M}	0.89	-12.00
E_{A-10M}	0.88	-14.47
$E_{A-14M_{3/7}}$	0.89	-14.35
$E_{A-14M_{2/7}}$	0.88	-18.42
$E_{A-10M(3\bar{2})_2}$	0.87(0.88)	-20.71
$E_{A-14M(5\bar{2})_2}$	0.87(0.89)	-22.69
E_{A-L1_0}	1.28	-27.37

3.3.3 Electronic structures of the modulated phases

In this section, we show the results on the densities of states (DOS) of different modulated and NM structures and try to understand the results on relative stabilities of the different structures by analyzing them. We first focus on the comparisons of the densities of states of the pseudocubic structures, the modulated 6M, 10M and

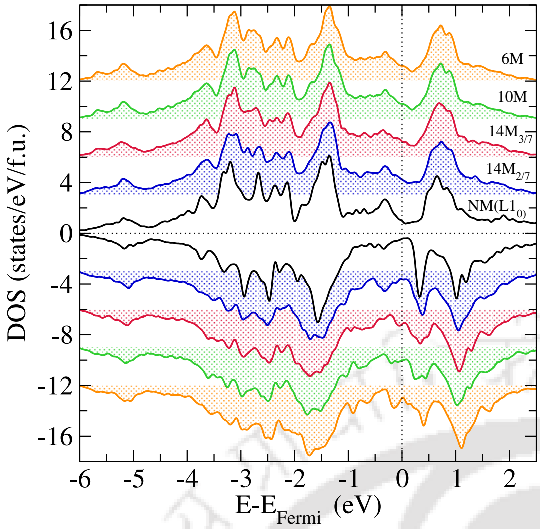

Figure 3.6: Total densities of states of different modulated pseudo-tetragonal structures (orthorhombic symmetry) along with that in the NM tetragonal ($L1_0$) structure.

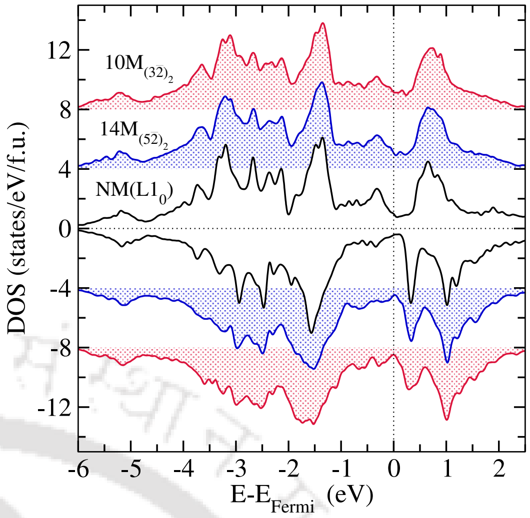

Figure 3.7: Total density of states of fully relaxed modulated structures along with that in the NM tetragonal ($L1_0$) structure.

14M structures with $c/a = 1$, with that of the cubic structure. The total densities of states near the Fermi level for the cubic and the four pseudocubic structures are shown in Fig. 3.4. Since the relative stabilities of the different structures can be understood from the features near the Fermi level, it is enough to focus on the features in the nearby region only. The results of Fig. 3.4 clearly show that the major changes in the densities of states are coming from the minority spin bands. For the cubic structure, the minority densities of states at the Fermi level were the largest. The lowering of the symmetry due to modulation redistributes the states at the Fermi level, which stabilizes the modulated phases. The particular stability of the 6M pseudocubic structure is reflected in the opening of a pseudogap in the minority band at the Fermi level. The direct comparison between the cubic structure and the 6M pseudocubic structure presented in Fig. 3.5 shows this more prominently. A look at the atomic contributions reveals that the features near the Fermi level, distinguishing the electronic structures of different phases, stem from the d electrons of MnI and Ni atoms which are occupying lattice positions, which correspond to the equivalent positions of Ni in the case of Ni_2MnGa. In both cases these states are responsible for the features in the electronic structures near the Fermi level. The relative stability of the 6M, 10M and 14M modulated structures with orthorhombic lattice parameters, obtained upon relaxation of the lattice parameters of the pseudocubic structures, can be motivated in the same way.

In Fig. 3.6, we provide a comparison between the densities of states of the 6M, 10M, $14_{3/7}$ and $14M_{2/7}$ pseudo-tetragonal structures along with that of the NM tetragonal structure. In Fig. 3.7, we show a comparison of the densities of states of monoclinic 10M and 14M structures along with that of the NM tetragonal structure. From both the figures(Figs. 3.6 and 3.7), we observe that the minority spin densities of states at the Fermi energy decreases gradually from pseudo-tetragonal and monoclinic modulated structures to the NM tetragonal structures, indicating that the structures gain more stability in the direction 6M→NM. The trend of change in the densities of states at Fermi energy is consistent with the trends in the energetics, thus explaining the relative stabilities of the different modulated phases. In Ni_2MnGa, a similar close correspondence was observed for the densities of states for the three structures. Since the electronic density of states represents a fingerprint of the local electronic environment at each site, this leads to the understanding that these optimized modulated structures are defected representations of the NM martensite, the so-called nanotwinned martensites. This, together with the extremely low values of γ_{twin}, the interface energies corresponding to the martensitic twin boundaries, led to the conclusion that the Ni_2MnGa is a paradigmatic example of an adaptive martensite [166, 172, 173]. For Mn_2NiGa, although the close connections between the densities of states of the fully relaxed modulated martensites and the NM martensite are visible, the values of γ_{twin} are one order of magnitude larger than those in Ni_2MnGa. The γ_{twin} is defined by the energy difference between the NM and the corresponding modulated structure per unit area of the interface. The energy difference between the NM and the $10M(3\bar{2})_2$ and $14M(5\bar{2})_2$ modulated structures of Mn_2NiGa are 26.63 meV/f.u. and 18.72 meV/f.u., respectively. So, the calculated γ_{twin} values for the $10M(3\bar{2})_2$ and $14M(5\bar{2})_2$ modulated structures are 2.86 meV/Å^2 and 2.02 meV/Å^2, respectively while those for Ni_2MnGa are only 0.25 meV/Å^2 and 0.06 meV/Å^2, respectively.

The similarities in the electronic structures of the fully relaxed modulated structures and the NM tetragonal structure along with the geometric visualization of the NM tetragonal building blocks in the supercell of the modulated structures indicate that the modulated structures can be conceived as nanotwinned structures with a high number of interfaces between its nonmodulated twins, but the high values of γ_{twin} hamper the realization of adaptive martensites in Mn_2NiGa. The question of whether such structures can become thermodynamically stable without additional external stress can only be addressed through the computation of the free energy and is beyond the scope of the present work. Another immediate outcome of the similarities in the electronic structures across various phases is the similarity in their element-resolved magnetic moments listed in Table 3.4. It can be seen that the changes in the magnetic moments across different structures are not very substantial. The atomic moments of the two Mn atoms too do not practically change across structural phases. The largest change is observed in the atomic moment of Ni atom. This is consistent with the role of Ni in hybridisations near the Fermi surfaces which bring about the changes in the electronic structures across the modulated phases. We have compared our results on total and atomic magnetic moments with available theoretical [77, 86, 205, 208] and experimental [204, 206, 209, 210] results. Our results are in excellent agreement with the results (for cubic and tetragonal NM structures only)from other theoretical calculations which are DFT based. In the next subsection, we focus on understanding the origin of the modulated martensites in Mn_2NiGa.

3.3.4 Phonon instability, Fermi Surface Nesting and Generalised Susceptibility

The total energy curves and the analysis of the densities of states of austenite and different modulated and NM martensites of Mn_2NiGa provide us with the possible sequence of phase transformation, relative stabilities of different martensites and changes in the electronic structures as the system makes a transition from the cubic austenite to the NM martensite phase via different modulated structures. The question now remains as to why different modulated structures are observed to occur.

Phonon dispersion relations in Ni_2MnGa provided an important clue to the origin of particular modulated structures observed experimentally. An anomalous softening of the transverse acoustic (TA_2) phonon branch in $[\xi\xi 0]$ direction in the cubic $L2_1$

Table 3.4: The calculated total(M_{Tot} in $\mu_B/f.u.$) and average atomic magnetic moments(M_X in μ_B) of Mn_2NiGa in cubic, tetragonal and different modulated phases. The results from literature are given in parenthesis.

Structure	M_{Tot}	M_{MnI}	M_{MnII}	M_{Ni}	M_{Ga}
Cubic	1.17(1.14,[208] 1.177,[77] 1.18,[86] 1.13 [205])	-2.37(-2.52[205])	3.14(3.31[205])	0.33(0.34[205])	0.01
6M	0.95	-2.41	3.05	0.25	0.01
10M	0.83	-2.47	3.05	0.21	0.01
$14M_{3/7}$	0.91	-2.44	3.05	0.24	0.01
$14M_{2/7}$	0.87	-2.45	3.04	0.22	0.01
$10M(3\bar{2})_2$	0.81	-2.48	3.04	0.20	0.01
$14M(5\bar{2})_2$	0.87	-2.43	3.03	0.22	0.01
Tetragonal	1.00(1.01,[208] 1.017,[77] 1.00[86])	-2.35	3.04	0.26	0.01

phase, with the pronounced softening at $\xi \approx 0.33$, ξ being the reduced reciprocal lattice vector, was interpreted to be the precursor to the martensitic transformation. DFT calculations of phonon dispersion relations for the $L2_1$ austenite phase in Ni_2MnGa provided completely unstable transverse acoustic mode (TA_2) along the $[\xi\xi0]$ direction with the ξ value at which the instability is pronounced being close to 0.33 [169]. The wave vector at which the instability is maximum could be fitted into a 6M modulated structure, and thus the 6M phase was interpreted to be the premartensitic phase arising out of the phonon instability. Later DFT calculations found the phonon instability rather at around $\xi \approx 0.4$ [211], which could be connected to a 10M modulated structure observed in diffraction experiments. Taking the cue from Ni_2MnGa, we have computed the phonon dispersion relations for Mn_2NiGa.

In Fig. 3.8 we plot the phonon dispersion relations for Mn_2NiGa along different symmetry directions in the entire Brillouin zone. We compare this directly with the calculated dispersion of Ni_2MnGa from Ref. [212], which was obtained in a similar technical setup and agrees excellently with the dispersion measured by inelastic neutron scattering. In Mn_2NiGa, along the $[\xi\xi0]$ direction, we find the TA_2 mode to be unstable with the frequency being imaginary in the range between Γ and $\xi = 0.45$ with a pronounced instability (the minimum value of the frequency) at $\xi \approx 0.33$. The results agree very well with an earlier calculation with density functional perturbation theory (DFPT) using ultrasoft pseudopotentials [213], except a small deviation regarding the range for which the frequency of the TA_2 mode is imaginary. This small deviation might be due to use of different pseudopotentials and different parameters in DFPT [213]. We do not find any instability in any of the other symmetry directions. The comparison with Ni_2MnGa shows that the dispersion relations in the two materials are very similar, highlighted by the single instability along the $[\xi\xi0]$ direction, and differing only in the ξ value at which the instability is most pronounced. This implies that the phonon related physics would be very similar for the two systems. One immediate consequence of the phonon instability in Mn_2NiGa would be to associate it with the 6M modulated structure which is found to be the most stable pseudocubic structure in our calculations, much the way it was done in case of Ni_2MnGa [169, 211]. However, deeper understanding into the electronic origin of the modulated structures needs to be gained from further analysis of the phonon dispersions along the given direction.

The softening of acoustical modes in martensitic materials at a finite fraction ξ of a reciprocal lattice vector $\underline{q}$ in a specific direction is frequently discussed in terms

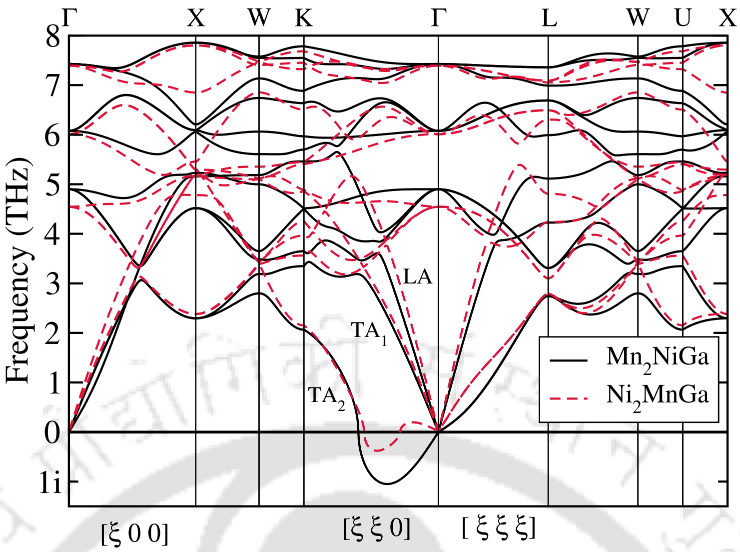

Figure 3.8: Full phonon dispersion curve for Mn$_2$NiGa (solid line) and Ni$_2$MnGa (dashed line) in the cubic structure. The calculated dispersion for Ni$_2$MnGa was taken from Ref. [212].

of electron-phonon coupling. The contribution from electron-phonon coupling to the dynamical matrix is given by the expression [214, 215]

$$D^{\alpha\beta}_{\mathrm{el-ph}}(\underline{q}) \quad = \quad \sum_{\underline{k},m,n} \frac{f(\varepsilon_{\underline{k},m}) - f(\varepsilon_{\underline{k}+\underline{q},n})}{\varepsilon_{\underline{k}+\underline{q},n} - \varepsilon_{\underline{k},m}} \quad g^{\alpha *}_{\underline{k},m,\underline{k}+\underline{q},n}\, g^{\beta}_{\underline{k}+\underline{q},n,\underline{k},m} \tag{3.1}$$

where f is the Fermi distribution function, $\varepsilon_{\underline{k},m}$ are the energies of band m corresponding to the reciprocal lattice vector $\underline{k}$, and α, β refer to the Cartesian directions. The g denote the matrix elements describing the strength of the electron-phonon coupling. As these are difficult to calculate and in many cases only little variation is expected, they are often treated as constant. In the constant matrix element approximation, one can obtain, from the phonon self energy, the so-called generalized susceptibility $\chi_0'(\underline{q}, 0)$ [216], which is the real part of the bare electronic susceptibility

$$\chi_0(\underline{q}, \omega) = \sum_{\underline{k},m,n} \frac{f(\varepsilon_{\underline{k},m}) - f(\varepsilon_{\underline{k}+\underline{q},n})}{\varepsilon_{\underline{k}+\underline{q},n} - \varepsilon_{\underline{k},m} - \hbar\omega - i\delta} \tag{3.2}$$

in the low phonon frequency limit $\omega \rightarrow 0$. The denominator of $\chi_0'(\underline{q}, 0)$ is the difference in the occupation of initial and final states connected by a wave vector $\underline{q}$, which becomes maximum when the former are occupied and the latter empty. Therefore peaklike features in the generalized susceptibility can be regarded as indication for an electronic instability which is related to the topology of the Fermi surface. From the imaginary part $\chi''(\underline{q}, \omega)$, one can derive the quantity

$$\lim_{\omega \to 0} \frac{\chi_0''(\underline{q}, \omega)}{\omega} = \sum_{\underline{k}} \delta\left(\varepsilon_{\underline{k}} - \varepsilon_{\mathrm{F}}\right) \delta\left(\varepsilon_{\underline{k}+\underline{q}} - \varepsilon_{\mathrm{F}}\right) . \tag{3.3}$$

It is termed the “nesting density” since it provides a measure for nesting regions of the Fermi surface, which are connected by a rigid vector $\underline{q}$. The nesting density is straightforwardly obtained from the Fermi surface alone, whereas $\chi_0'(\underline{q}, 0)$ also contains contributions from bands farther away from the Fermi surface. These are not effectively suppressed since their contributions scale inversely to the energy difference between occupied and unoccupied states. Indeed, this may be significant in the sense that their extremal features do not necessarily coincide. One example is the so-called hidden nesting observed in purple bronze, which can occur, although obvious nesting features are absent according to avoided crossing of bands right at the Fermi surface [217]. Consequently, the use of Eq. (3.3) as a replacement for $\chi_0'(\underline{q}, 0)$ has been criticized [218].

The connection between Fermi surface nesting and the transition to a premartensitic modulated structure appears to be well established for the case of the conventional shape memory alloys [223]. For the magnetic shape memory system Ni_2MnGa, a first systematic discussion of band structure, Fermi surface, and generalized susceptibility was provided by Velikokhatnyi and Naumov [224]. The authors found that in the minority spin $\chi'(\underline{q})$, there were two pronounced maxima along [110] (in units of π/a, where a is the lattice constant), one at $\xi_1 = 0.43$ and a second at $\xi_2 = 0.59$. Due to the discrepancy with the experimentally observed phonon softening at experimental value $\xi \approx 0.33$, the authors suggested that the transition to the 6M premartensite should rather be of anharmonic origin following the suggestion of Gooding and Krumhansl [225, 226], while ξ_1 corresponds to the incommensurate 10M martensite observed in diffraction experiments. Lee, Rhee, and Harmon [168] pointed out that a peak corresponding to the 6M premartensite exists in the $\chi'(\underline{q}, 0)$ of the 17th majority spin band. The position of this feature is fine tuned through the reduction of the Ni exchange splitting and eventually matches the observed 6M modulation due to the increasing magnetic disorder at finite temperatures, which was confirmed later on by similar calculations of Haynes and co-workers [221]. Bungaro, Rabe, and Dal Corso [169] directly compared the Fermi surface with the full phonon dispersion of austenite Ni_2MnGa calculated by means of density functional perturbation theory [227]. Their calculations reveal an instability in the [110] di-

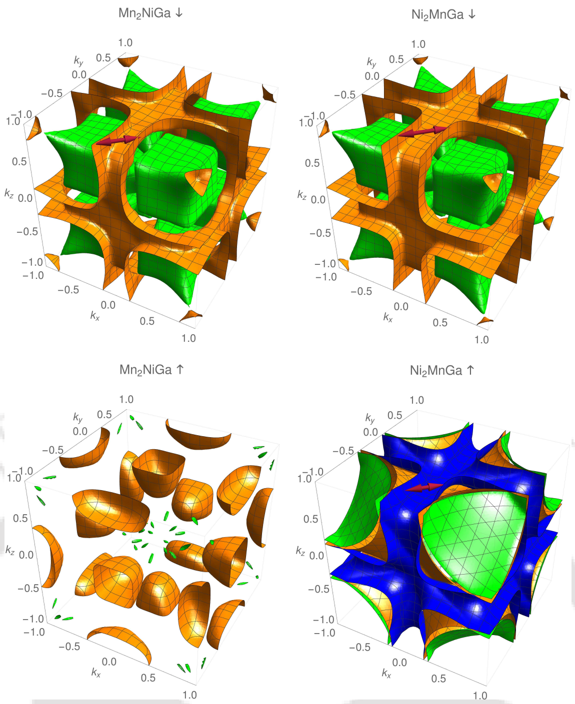

Figure 3.9: Minority spin (top row) and majority spin (bottom row) Fermi surfaces of Mn_2NiGa (left column) and Ni_2MnGa (right column) in the extended zone scheme, represented by a cubic box with the edge length $2\pi/a$. The center and the corners of the box refer to the Γ point. Each band crossing the Fermi energy (three in the case of the majority spin channel and two for the minority spin channel) is indicated by an individual color (green: 17th spin-up and the 13th spin-down band of Ni_2MnGa and 14th spin-up and 13th spin-down band of Mn_2NiGa; orange: 18th spin-up and 14th spin-down band of Ni_2MnGa and 15th spin-up and 14th spin-down band of Mn_2NiGa; blue: 19th spin-up band of Ni_2MnGa). The Fermi surfaces agree excellently with previous calculations for Mn_2NiGa [208, 213] and Ni_2MnGa. [169, 181, 182, 219–222] The red arrows indicate possible nesting vectors according to the respective first maxima of $\chi'_0(\underline{q},0)$ at $\underline{q}=\xi_1\,[1\,1\,0]$ as calculated in this work. The figure is generated by Markus E. Gruner.

rection which corresponds to the nesting vectors obtained from cross sections of the Fermi surface. Later works [181, 184, 189, 219, 221] confirmed this picture, which coincides well with the nesting present in the minority spin Fermi surface shown in Fig. 3.9. The shape of the minority spin Fermi surface of Ni_2MnGa has been verified experimentally using the positron annihilation technique [221]. An analogous relation between Fermi surface nesting and phonon instability has also been proposed for Mn_2NiGa [208, 213], while calculations of $\chi'_0(\underline{q})$ are missing for this system, so far. The antiparallel orientation of the spin moments of Ni and MnI allows for a perfect hybridization of their minority spin states. In consequence the minority Fermi surfaces of Ni_2MnGa and Mn_2NiGa are nearly identical. The only visible difference is the smaller distance of the (orange) plane sheets forming the

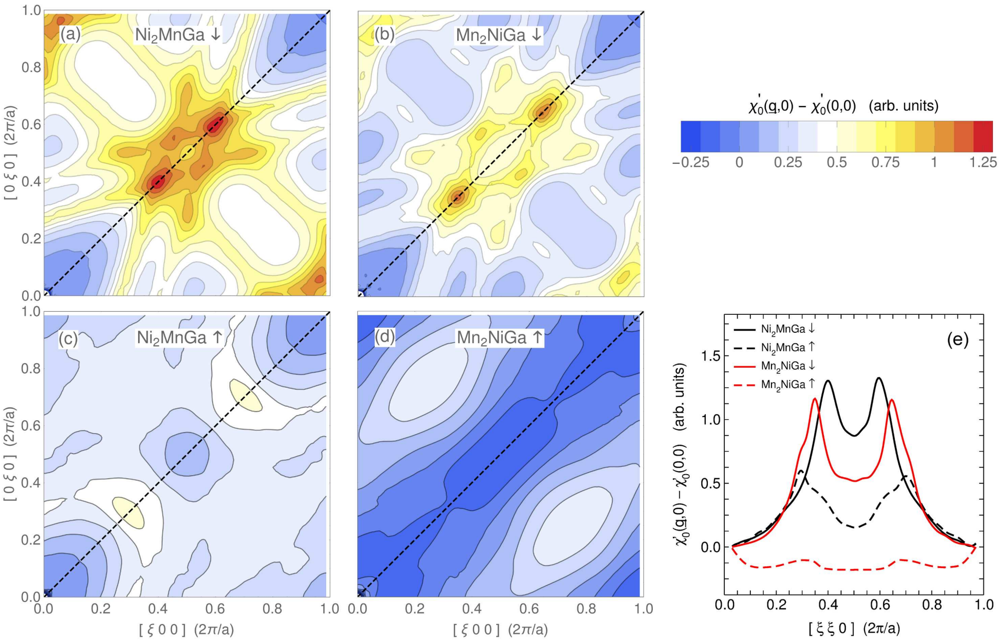

Figure 3.10: Real part of the generalized susceptibility in the low-frequency limit $\chi'_0(\underline{q}, 0)$ of Ni_2MnGa and Mn_2NiGa for wave vectors $\underline{q}$ in the [1 0 0]-[0 1 0] plane: (a) and (b) show the minority spin contribution, (c) and (d) the majority spin channel. Panel (e) shows the cross sections along the [1 1 0] direction indicated by the dashed lines in (a)−(d). In all cases, a moderate electronic temperature of $T = 50$ K was assumed to smoothen the features. The long-wavelength limit $\chi'_0(0, 0)$ has been subtracted, such that the absolute magnitude of the features represented by the color coding can be compared. The difference between two neighboring contour lines is 0.1 (arbitrary units) in (a)-(d). The figure is generated by Markus E. Gruner.

narrow rectangular channels in Mn_2NiGa, which originates from the e_u-peak being slightly closer to the Fermi level. In turn, MnI does not occupy all states in the majority channel, which reduces hybridization and the majority spin Fermi surfaces of Ni_2MnGa and Mn_2NiGa do not resemble each other at all, as can be seen from the lower panels of Fig. 3.9. From this, we can conclude that mechanisms derived from the electronic structure of Ni_2MnGa should be transferable to Mn_2NiGa, if they involve the minority spin states only. In contrast, effects connected to features of the majority spin electronic structure in Ni_2MnGa should not be observed in Mn_2NiGa.

In Fig. 3.10 we present a detailed comparison of $\chi'_0(\underline{q}, 0)$ between both systems, Ni_2MnGa and Mn_2NiGa, for both spin channels. Unlike previous studies on Ni_2MnGa, we take into account vectors $\underline{q}$ in the whole [1 0 0]-[0 1 0] plane. We consider all bands present in an interval of ± 0.5 eV around the Fermi level, which are in particular the 17th-19th spin-up and the 12th-15th spin-down bands for Ni_2MnGa and the 12th-15th spin-up and the 14th-17th spin-down bands for Mn_2NiGa (not counting the Mn- and Ni-3p and Ga-3d semicore states). To allow for direct comparison, the scale of all panels in Fig. 3.10 is the same. This was realized by subtracting $\chi_0'(0,0)$, following the argument that for $\underline{q} \to 0$, the electronic and ionic contributions of the dynamical matrix cancel each other [228]. The cross section along [110] shown in Fig. 3.10 (e) shows pronounced maxima at $\xi_1 = 0.4$ and $\xi_2 = 0.6$ in the minority spin channel and at $\xi_1 = 0.3$ and $\xi_2 = 0.7$ in the majority channel for Ni_2MnGa, which reproduces the trend previously reported by Lee *et al.* [168], in particular the much smaller magnitude of the features in the majority compared to the minority channel.

The small differences in the numerical values of Refs. [224] and [168] may be related to the use of the GGA in the present study as opposed to the LDA exchange correlation used previously. For Mn_2NiGa, the minority channel shows, as expected, a very similar structure, with slightly shifted and lesser pronounced maxima at $\xi_1 = 0.35$ and $\xi_2 = 0.65$. As depicted in Fig. 3.10 (a,b), these maxima are indeed confined to $\underline{q}$ along $[1\,1\,0]$. If we identify the maximum at smaller ξ with the soft TA_2 phonon, this fits very well to the instability being observed at smaller wavelength in Mn_2NiGa. The close similarity between both systems in the minority spin $\chi_0'(\underline{q})$ extends to the entire $[1\,0\,0]$-$[0\,1\,0]$ plane and includes also the maxima close to $[1\,0\,0]$ and the satellites around $[\frac{1}{2}\,\frac{1}{4}\,0]$. In contrast, the generalized susceptibility shows no resemblance between both system in the majority spin channel. In Mn_2NiGa, the majority spin $\chi_0'(\underline{q},0)$ is essentially featureless, while in Ni_2MnGa, we find the above-mentioned maximum in the $[1\,1\,0]$ direction around $\xi_1 = 0.3$, which Lee *et al.* related to the premartensite modulation [168]. On the premise that the modulation in martensite and premartensite could be of different origin this alone is not necessarily a contradiction, since in experiment a premartensitic modulation has not been reported for Mn_2NiGa so far.

The red arrows in Fig. 3.9 show exemplarily the vectors belonging to the maxima at $\underline{q} = \xi_1\,[1\,1\,0]$. As discussed above, maxima of the generalized susceptibility do not necessarily need to indicate the most frequent nesting vectors characterized by $\chi_0''(\underline{q},0)$. Nevertheless, they appear to achieve this quite well for the minority channel of both Ni_2MnGa and Mn_2NiGa. Here, nesting is expected between the walls of the rectangular flat channel structure formed by the 14th band (indicated by the arrows in the top row of Fig. 3.9), as well as between the parallel surfaces of the cube like structures formed from the 13th band (which are hidden beneath the sheets of the 13th bands) [169, 181, 208, 213, 221, 224]. In the majority channel of Ni_2MnGa, nesting was reported to occur mainly within the 17th band between the flattened surfaces of the central hole pocket around Γ and its periodic images (again hidden in Fig. 3.9 by the surfaces 18th and 19th band) [168, 221], while some nesting is also present in the other bands.

Conversely, the importance of Fermi surface nesting for the systems might be assessed by comparing the electronic density of states between the dynamically unstable cubic $L2_1$ phase and the energy-minimizing modulation in pseudocubic structure in a cell with $L2_1$ lattice parameters. Since the redistribution of states at the Fermi level is thought to drive the transition to the martensitic modulation in the spirit of a Peierls instability, a condensed soft phonon should remove the nesting parts of the Fermi surface, accompanied by a characteristically reduced DOS around the Fermi level. This is indeed the case for the minority spin channel of Mn_2NiGa in a very similar fashion to that for the minority channel of Ni_2MnGa (Ref. [229]). In turn, the majority channel DOS remains essentially unaltered at the Fermi level, even for Ni_2MnGa, which underlines the importance of the minority spin e_u states for the electron-phonon coupling in both cases. Thus the comparison of both systems yields a strong support for the view that the softening of the $[1\,1\,0]$ TA_2 acoustic branch observed in the ground-state phonon calculations is essentially nourished by the nesting features of the minority spin Fermi surface. A final discussion of this issue requires, however, the first-principles evaluation of the respective electron-phonon coupling matrix elements, which is beyond the scope of the present work.

3.4 Conclusions

In this chapter, we have presented a comprehensive study of the structural and electronic properties of the recently found, comparatively less explored shape memory alloy Mn_2NiGa by density functional theory based calculations. Our calculations confirmed the existence of the experimentally observed 14M modulated martensite phases with two different symmetries. Our calculations revealed the possible existences of other modulated martensites, 6M and 10M with orthorhombic symmetry and 10M($3\bar{2}$) with monoclinic symmetry. The total energy calculations indicated that the high-temperature cubic phase will be first driven towards a intermediate 6M pseudocubic premartensite state, which should immediately decay downhill into a modulated structure with a significant pseudotetragonal distortion. Afterwards the relaxations of the internal coordinates and the structural parameters will stabilize other modulated structures. This corresponds well to the fact that the complementary phonon calculations in the cubic phase show that the cubic structure is unstable and that the instability can be mapped onto a 6M modulated structure. Our results attribute the origin of the instability to the Fermi surface nesting features in the minority spin bands, while no supporting contribution is encountered from the majority spin electronic susceptibility. The striking similarities in the features of the minority band Fermi surfaces and the susceptibilities for Mn_2NiGa and Ni_2MnGa lead us to believe that the electronic mechanism driving the martensite transformations in these two systems are similar. The calculations of the structural parameters in various modulated phases and the relative energies (of modulated phases) with respect to the non-modulated ground state reveal important differences with Ni_2MnGa, the prototype magnetic shape memory alloy. On the other hand, this also indicates that the maximum achievable MFIS in Mn_2NiGa would be greater than that in Ni_2MnGa.

In summary, comparing our DFT results for Mn_2NiGa side by side with Ni_2MnGa, we would like to sketch the following potential scenario for the martensitic transformation process: In both systems, wavelike modulations in the cubic phase provide an energetic advantage of a few meV/atom over the $L2_1$ austenite. This arises from the nesting features of the Fermi surface connected to an enhanced electronic susceptibility at specific wave vectors along [110]. When temperature becomes sufficiently low, this may end in a static modulation of the ionic positions. In Ni_2MnGa this corresponds to the premartensitic 6M state, which is stabilized by vibrational entropy in a certain range of temperatures above the martensitic transformation [207]. Although the energy gain from a 6M modulation in the pseudocubic lattice is significantly larger in Mn_2NiGa, this does not imply a stable premartensite phase, here. The reason is that the pseudo-tetragonal wave-like 6M in Ni_2MnGa has a metastable energy minimum at $c/a = 0.985$, close to 1, whereas in Mn_2NiGa this condition is not fulfilled as the energy landscape implies a downhill relaxation towards a state with a much larger tetragonal distortion c/a, which is similar for all modulated structures. Our calculations only consider commensurate modulations. Thus, we cannot exclude incommensurate modulations being lower in energy. But we expect such modifications to be small, since the extremal features in the generalized susceptibility and the imaginary phonon branches are rather close to the commensurate wave vectors. In addition, there is no reason to stop the relaxation process right here, since the other modulations in the pseudotetragonal cell and even more the monoclinic nanotwinned states are significantly lower in energy. According to the concept of adaptive martensite [170], a specific twinning sequence will be favored since it additionally benefits from minimizing the elastic energy at the interface to austenite, which dominates when the growing martensite plates are still sufficiently small. For Ni_2MnGa, recent DFT results imply that pseudotetragonal 10M modulation may finally be stabilized by vibrational entropy [174], while the adaptive nanotwinned 14M structure is nearly degenerate with the non-modulated $L1_0$ phase at $T = 0$ [173, 176]. Therefore, macroscopic regions of 14M can remain metastable for a very long time. Eventually, the nanotwin boundaries may be eliminated in an irreversible twin coarsening process through the (stress-induced) motion of twinning dislocations [172, 230]. We expect the significantly larger twin boundary energy in Mn_2NiGa to speed up this process, such that the nanotwinned intermediate state might not be observed unless the sample is strained. This, once again, corresponds well to the experimental observation of stress-induced modulated structures in Mn_2NiGa [68].

Chapter 4

Effect of Fe and Co substitution on the martensitic stability and the elastic, electronic, and magnetic properties of Mn_2NiGa

4.1 Introduction

Controlled substitution of one element with another is a standard procedure for achieving target properties of materials. In order to optimize the thermodynamic parameters without compromising much on the other important properties for functional applications such as MFIS, substitution of each one of the constituents in Ni_2MnGa with other transition metals Fe, Co and Cu have been attempted. The outcomes of these attempts are mixed and provide useful insights into the fundamental physics of this system which can be useful in designing this material with target properties. A larger MFIS of about 12% was observed in the non-modulated tetragonal phase of Ni_2MnGa upon substitution of all three elements by 4% of Co and Cu each.[202] Several investigations with substitution of a single type of transition metal into different sub-lattices have also been carried out. The outcome of substitution at the Ni site is substantial reduction of T_m with slight improvement in T_c,[231–233] irrespective of whether the substituting element is Fe, Co, or Cu. Substitution at the Mn site, on the other hand, produced results depending on the substituting element. While substitution of Mn by Co or Cu elevates T_m and reduces T_c as the concentration of the substituting element increases,[234–236] T_m

---

The contents of this chapter are published in Physical Review B **96**, 174107 (2017) is observed to decrease as a function of Fe concentration when Fe is substituted at the Mn site. Substitution at the Ga site by either Fe, Co, or Cu shows a trend of rapid increase in T_m and slow decrease of T_c, resulting in them coinciding for the concentration of the substituting element in the range of 10-20%.[236–238] These outcomes, thus, prove that the structure-property relationships in Ni-Mn-Ga-based systems delicately depend on the substituting element, the substituent, and the composition.

In chapter 3, we have explored the interrelation between the large MFIS and the modulated structures of Mn_2NiGa. A hindrance to obtain significant MFIS at a low applied magnetic field in Mn_2NiGa is its low value of magnetization which is about $1.2\mu_B$ per formula unit as opposed to more than $4\mu_B$ per formula unit in Ni_2MnGa. This happens due to a ferrimagnetic ground state arising out of anti-parallel orientation of the two Mn atoms. Substitution by another magnetic atom such as Co, Fe, and Cu could be an useful way to adjust the magnetic interactions in the parent alloys, thus improving the magnetization primarily. With this motivation, Luo *et al.* substituted Mn with Fe in Mn_2NiGa [239]. They observed an increase in the saturation magnetization with increasing Fe concentration. However, both T_m and T_c decrease with increasing Fe content and no martensitic transformation is observed beyond 30% of the Fe content [239]. Ma *et al.* investigated the effect of Co substitution at Ni and Ga sites of Mn_2NiGa through magnetization measurement and *ab initio* calculations [240]. They found a remarkable three fold jump in the saturation magnetization when Co is substituted at Ga sites which, by means of *ab initio* calculation, was attributed to a complex sub-lattice occupancy pattern. Though Co substitution at the Ni site was not as dramatic, the magnetization improved which was explained by means of increasing ferromagnetic component in a ferrimagnetic host. In both cases, the martensitic transformation vanished rapidly indicating stabilization of the the Inverse Heusler phase down to low temperature. A different variation of T_c with Co content was observed depending on the site of substitution. Very recently, DFT calculations on Cu-doped Mn_2NiGa reported that T_m decreases when Cu is substituted at Mn and Ni sites but increases when substituted at the Ga site [241].

The investigations on substitution of another transition metal in Mn_2NiGa are thus quite scattered. However, they offer very interesting perspectives, both for fundamental understanding as well as for engineering materials with target properties. The number of valence electron per atom(e/a) was identified to be a predictor of T_m with $T_m \sim e/a$ [242–244] for systems undergoing martensitic transformations.

In the case of off-stoichiometric Ni_2MnGa alloys and Fe, Co and Cu substituted Ni_2MnGa alloys e/a was found not to correlate with T_m [104–106, 245]. Instead, the shear modulus C' was found to be a better predictor for composition dependence of T_m [105, 106]. On the other hand, ΔE, the energy difference between the high-temperature Heusler phase and the low-temperature NM tetragonal phase, was found to correlate well with C' and T_m for a number of systems in the Ni-Mn-Ga family [246, 247]. Experimental results on substituted Mn_2NiGa [239, 240] indicate that e/a does not correlate with T_m. On the other hand, the variations of T_c and magnetization in substituted Mn_2NiGa depend, both quantitatively as well as qualitatively, not only on the nature of the element that is being substituted. Another noteworthy point is the gradual stabilization of the high symmetry inverse Heusler phase with substitution, irrespective of the chemical identity of the substituting atom and the site on which it is being substituted, in substituted Mn_2NiGa. Recent DFT calculations of magnetic moments and the electronic structures in two compounds, MnCoNiGa and MnFeNiGa, predict that the compounds are nearly half metals [248]. We note that these two compounds can be obtained by substituting 50% of the total Mn content in Mn_2NiGa.This implies that the substitution of Mn in Mn_2NiGa would potentially give rise to materials with different functional properties. Given these findings, one needs a systematic first-principle-based investigation addressing the multiple issues, under a single approximation, in order to provide a fundamental understanding of the interrelations between composition, sub-lattice occupancy, phase stability, and magnetic interactions. An investigation along this line would help to tune the necessary parameters for targeted applications in Mn_2NiGa-based systems and possibly in Ni-Mn-Ga systems over a wide composition range.

In this chapter, we report the outcome of substitution of 25%, 50%, 75% and 100% Fe and Co at different sites of the parent compound Mn_2NiGa. Specifically, we have looked at the patterns of site occupancies upon a particular substitution, the stabilities of the martensitic NM phases, the elastic properties, the total and atomic magnetic moments, the effective magnetic exchange interactions, and the magnetic transition temperatures and their variations upon substitution at different sites. The results are interpreted from the composition dependencies of the computed electronic structures.

4.2 Computational Methods

The total energies, the electronic structures and the magnetic moments were calculated with the spin-polarized density functional theory (DFT) based projector augmented wave (PAW) method as implemented in the Vienna Ab-initio Simulation Package (VASP) [120, 177, 178]. For all calculations, we have used the Perdew-Burke-Ernzerhof implementation of the generalised gradient approximation (GGA) for the exchange-correlation functional [179]. An energy cut off of 450 eV and a Monkhorst-Pack [180] $11 \times 11 \times 11$ k-mesh were used for self consistent calculations. A larger k mesh of $15 \times 15 \times 15$ was used for the calculations of the electronic structures. The convergence criteria for the total energies and the forces on individual atoms were set to 10^{-6} eV and 10^{-2} eV/Å, respectively. To investigate the stability of the substituted compounds, we have calculated the formation energy for each system, which can be obtained in the following way,

$$E_f = E_{tot} - \sum_i n_i E_i \tag{4.1}$$

E_{tot} is the ground state total energy of a system, E_i is the ground state energy of the i-th component in its elemental phase, and n_i is its concentration in the system under consideration.

The elastic moduli are calculated from the total energies and their derivatives. Since differences of total energies are associated with these calculations, the convergence criteria have to be tighter. Thus, we have used a larger k-mesh of $15 \times 15 \times 15$ for computations of total energies related to the evaluation of the elastic constants. The convergences with respect to the plane wave cut off and total energies are kept same as those for self consistent calculations. The method of calculating elastic constants has been described in chapter 2.

The magnetic pair exchange parameters are computed in order to understand the nature of the magnetic interactions in these systems. They are efficiently calculated using the multiple-scattering Green's function formalism as implemented in the SPRKKR code [141] and as discussed in chapter 2. In order to calculate the total energy by the SPRKKR code, a full-potential spin polarized scaler relativistic Hamiltonian with angular momentum cut off $l_{max} = 3$ is used along with a converged k mesh for Brillouin zone integrations. The Green's functions are calculated for 32 complex energy points distributed on a semi circular contour. The energy convergence criterion was set to 10^{-5} eV for the self-consistency cycles. The equilibrium lattice parameters obtained from the PAW calculations were used in these calculations. These exchange parameters are then used for the calculations of Curie temperatures (T_c). The Curie temperatures are estimated with two different approaches: the mean-field approximation (MFA) [147] and the Monte Carlo simulation (MCS) [145] method. The Mean field approximated T_c have been computed using magnetic exchange interactions $J_{ij}^{\mu\nu}$ for upto twenty neighbours around each atom. The Monte Carlo simulations have been carried out using Metropolis algorithm[145]. Magnetic exchange interactions $J_{ij}^{\mu\nu}$ for upto twenty neighbours surrounding each atom have been considered to construct the Heisenberg Hamiltonian (chapter 2). At each temperature, 80000 Monte Carlo steps have been performed to achieve convergences in the total energies. The Curie temperatures are obtained from the resulting $M-T$ relationship, where M is the total magnetic moment of the system and T the temperature.

4.3 Results and Discussions

In this work, we focus on the high-temperature phase of Mn_2NiGa which is inverse Heusler phase, described in chapter 1. The results obtained in this phase would be enough for most of the physical understanding about the effects of substituting another magnetic element on the functional properties of Mn_2NiGa. To model the chemical substitution, we have taken a 16-atom conventional cubic cell. Thus, chemical substitution of 25 %, 50%, 75%, and 100% can be modelled by successive replacement of the atoms of one of the constituents. For example, to make a 25% Co substitution at the Ni site, one Ni atom out of the four in the 16 atom cell is to be replaced with one Co atom. This modeling strategy has worked well in cases of investigations on chemically substituted Ni_2MnGa [249, 250].

4.3.1 Site preferences, stability and structural parameters

The site occupancies in a substituted system have an important impact on the physical properties of the system. Thus, before proceeding with computations of the physical properties, the site preferences of the substituting atom are to be decided. If the substituting atom occupies the site of the substituted element, the configuration is “normal”; otherwise it is termed “abnormal”. The preferred site occupancy is determined by comparing the total energies of the two configurations. In the case

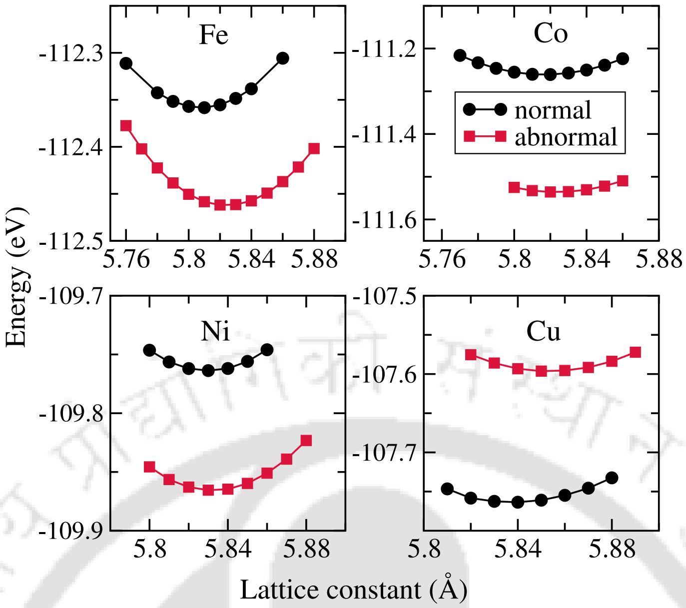

Figure 4.1: Calculated total energy as a function of lattice constant for 25% Fe, Co, Ni, and Cu substituted at the Ga site in $Mn_2NiGa(Mn_2NiGa_{0.75}X_{0.25})$. "normal": Fe, Co, Ni, or Cu occupy the Ga sublattice; "abnormal": Fe, Co, Ni, or Cu occupy the MnI sites and remaining MnI atoms move to Ga sites.

of Fe and Co-substituted Ni_2MnGa, free-energy calculations revealed that the preferred configuration in cases of substitutions at Ni or Mn sites are "normal" whereas the substitution at Ga site prefers an "abnormal" configuration[substituting Fe (Co) occupies the Mn (Ni) sites while the rest of the Mn (Ni) move to Ga sites] [106]. For Cu-substituted Ni_2MnGa, the preferred configuration always is the "normal" one [106]. In the case of Co and Cu substituted Mn_2NiGa, the trend of site occupancy is found to be quite similar to that of substituted Ni_2MnGa systems [240, 241]. It has been observed that in Heusler alloys, the following pattern of site occupancy is generally followed: the substituting transition-metal atom will prefer the 4a and 4b sites if it has a larger number of valence electrons, while it will prefer the 4c and 4d sites if the number of valence electrons is less [55–58, 251]. This has been observed even in cases of anti-site disorder in Mn_2NiZ alloys [78, 252]. So the substituting Fe or Co in Mn_2NiGa would prefer the MnI sites over MnII sites if Mn atoms were being substituted, as, Fe and Co both have larger numbers of valence electrons than Mn. We have verified this by comparing the total energies of two cases: one, where the entire Fe/Co occupies MnI sites and two, Fe/Co are equally distributed among the two Mn sites. For substitution of Fe or Co at the Ni site, we find the "normal" site occupancy (Fe/Co occupying Ni sites) to be energetically favorable. This is consistent with the general pattern described above and the previous first-principles

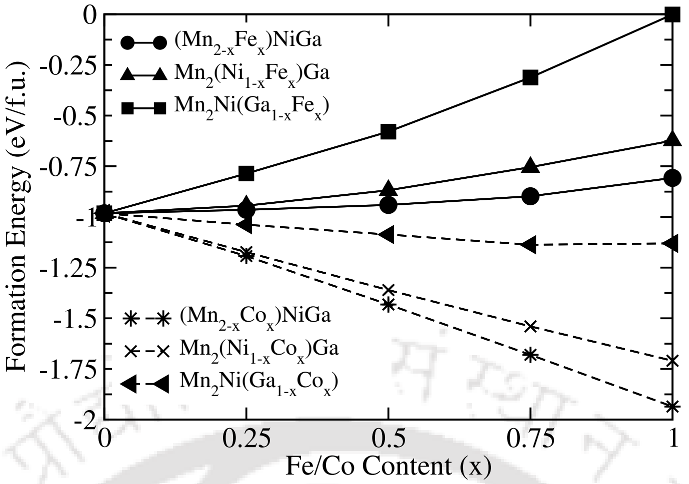

Figure 4.2: Formation energy (eV/f.u.) as a function of Fe and Co content substituted at different sites in Mn_2NiGa.

results on Co-substituted Mn_2NiGa [240]. The substitution at the Ga site, however, follows a different pattern, depending on the substituting element. In the case of Co substitution at the Ga site in Mn_2NiGa, earlier work [240] showed that the Co prefers to occupy the MnI sites pushing the remaining MnI atoms to Ga sites (henceforth denoted as MnIII). This can be understood on the basis of the general occupancy pattern in Heusler alloys described above: since Co has more valence electrons than Mn and Ga, it will occupy the MnI sites and the remaining MnI will occupy the Ga sites and would be distinguished from MnI and MnII by being denoted as MnIII. In order to check whether this is indeed the case with both Fe- and Co-substituted system, we have computed the total energies for "normal" and "abnormal" configurations. The results for 25% substitution are shown in Fig. 4.1. For comparison, we have also shown the results for Ni and Cu substitution at Ga sites. The results suggest that the "abnormal" site occupancies are preferable for Fe, Co and Ni substitutions at Ga sites of Mn_2NiGa while Cu substitution prefers a "normal" configuration. This exactly follows the trend obtained in substituted Ni_2MnGa [106]. We can thus conclude that the site preferences of the substituting transition-metal atom in Ni-Mn-Ga systems is dependent on the valence shell electronic configurations of both the atom that is being substituted and the substituting atom.

After fixing the site preferences of the atoms in substituted Mn_2NiGa, we computed the equilibrium lattice constants and the formation energies of the compounds obtained by chemical substitutions at various sites in the cubic Hg_2CuTi phase. The results are presented in Table 4.1. For all the cases, the equilibrium lattice constants

Table 4.1: Calculated values of equilibrium lattice constants (a_0), electron to atom ratios (e/a), and the formation energies (E_f) of various compounds in the Hg_2CuTi phase are given. The total energy differences (ΔE) between the austenite (Hg_2CuTi) phase and the martensite (tetragonal) phase (the equilibrium value of (c/a), the tetragonal distortion, is given in parentheses) and the corresponding volume changes ($|\Delta V|/V$) with respect to the equilibrium volume in the Hg_2CuTi phase, are given in the 5th and 6th columns. M_A is the total magnetic moment in μ_B/f.u. of the austenite phase. Reported values of lattice constants and magnetic moments in the literature are also given.

System	a_0(Å)	e/a	E_f (eV/f.u.)	ΔE(c/a) (mev/atom)	$\|\Delta V\|/V$ (%)	M_A ($\mu_B/f.u.$)	$a_0^{Lit.}$(Å)	$M_A^{Lit.}$ ($\mu_B/f.u.$)
Mn_2NiGa	5.84	6.75	-0.98	26.98(1.28)	0.65	1.16	5.91 [64, 239], 5.85 [85, 208], 5.88 [240]	1.14 [208], 1.18 [240]
$(Mn_{0.75}Fe_{0.25})NiMnGa$	5.83	6.8125	-0.96	8.55(1.26)	0.98	1.72	5.88 [239]	1.55 [239]
$(Mn_{0.5}Fe_{0.5})NiMnGa$	5.81	6.875	-0.94	-	-	2.62	5.86 [239]	2.68 [239]
$(Mn_{0.25}Fe_{0.75})NiMnGa$	5.78	6.9375	-0.90	-	-	3.46		
FeNiMnGa	5.75	7	-0.81	-	-	4.02	5.799 [248]	4.01 [248], 3.45 [248]
Mn_2NiGa	5.84	6.75	-0.98	26.98(1.28)	1.04	1.16		
$Mn_2(Ni_{0.75}Fe_{0.25})Ga$	5.82	6.625	-0.94	11.80(1.30)	0.42	1.45		
$Mn_2(Ni_{0.5}Fe_{0.5})Ga$	5.80	6.5	-0.87	5.07(1.34)	1.67	1.49		
$Mn_2(Ni_{0.25}Fe_{0.75})Ga$	5.79	6.375	-0.75	15.04(1.38)	1.71	1.31		
Mn_2FeGa	5.78	6.25	-0.62	33.07(1.40)	2.53	1.04	5.80 [253], 5.76 [85]	1.03 [85]
Mn_2NiGa	5.84	6.75	-0.98	26.98(1.28)	0.65	1.16		
$Mn_2Ni(Ga_{0.75}Fe_{0.25})$	5.82	7.0625	-0.78	9.56(1.30)	1.82	2.79		
$Mn_2Ni(Ga_{0.5}Fe_{0.5})$	5.80	7.375	-0.58	-	-	4.63		
$Mn_2Ni(Ga_{0.25}Fe_{0.75})$	5.77	7.6875	-0.31	-	-	6.40		
Mn_2NiFe	5.74	8	0.00	-	-	8.03		
Mn_2NiGa	5.84	6.75	-0.98	26.98(1.28)	0.65	1.16		
$(Mn_{0.75}Co_{0.25})NiMnGa$	5.83	6.875	-1.19	18.57(1.26)	0.43	1.97		
$(Mn_{0.5}Co_{0.25})NiMnGa$	5.81	7	-1.43	-	-	2.95		
$(Mn_{0.25}Co_{0.75})NiMnGa$	5.80	7.125	-1.68	-	-	3.78		
CoNiMnGa	5.78	7.25	-1.94	-	-	4.98	5.803 [248]	5.07 [248], 4.47 [248], 4.5 [232]
Mn_2NiGa	5.84	6.75	-0.98	26.98(1.28)	0.65	1.16		
$Mn_2(Ni_{0.75}Co_{0.25})Ga$	5.82	6.6875	-1.17	18.51(1.28)	0.02	1.46		1.52 [240]
$Mn_2(Ni_{0.5}Co_{0.5})Ga$	5.80	6.625	-1.36	7.00(1.28)	1.02	1.71	5.88 [240]	1.70 [240]
$Mn_2(Ni_{0.25}Co_{0.75})Ga$	5.78	6.5625	-1.54	-	-	1.92		
Mn_2CoGa	5.76	6.5	-1.70	-	-	2.00	5.78 [85]	2.00 [85]
Mn_2NiGa	5.84	6.75	-0.98	26.98(1.28)	0.65	1.16		
$Mn_2Ni(Ga_{0.75}Co_{0.25})$	5.82	7.125	-1.04	16.99(1.30)	1.82	2.88		3.11 [240]
$Mn_2Ni(Ga_{0.5}Co_{0.5})$	5.81	7.5	-1.09	-	-	4.73	5.84 [240]	5.29 [240]
$Mn_2Ni(Ga_{0.25}Co_{0.75})$	5.80	7.875	-1.14	-	-	6.94		
Mn_2NiCo	5.79	8.25	-1.13	-	-	9.04		

decrease linearly with increasing concentration of the substituting element. For most of the cases, this trend can be explained from the variations of atomic radii of the host (the atomic radii of Mn, Ni, and Ga are 1.27Å, 1.24Å and 1.35Å respectively) and the substituting elements(the atomic radii of Fe and Co are 1.26Å and 1.25Å respectively). The only exceptions are the substitutions at the Ni site where instead of an expected increase in the lattice constant with concentration of the substituting element, the lattice constant decreases. Thus, the trends in the variations in the lattice constants cannot be understood in terms of differences in atomic radii alone, and other effects such as bonding and magnetism are expected to play roles as was noted earlier [106, 241]. Another noteworthy point is that while the trends in the variations of the lattice constants obtained in this calculations qualitatively agree with those observed in the experiments on Fe substituted at Mn sites [239] and Co substituted at Ga sites of Mn_2NiGa [240], the experimentally observed trends are opposite to our calculated results in cases of Co-substituted at the Ni sites [240]. Experimentally, it is found that the lattice constant increases with increasing con-

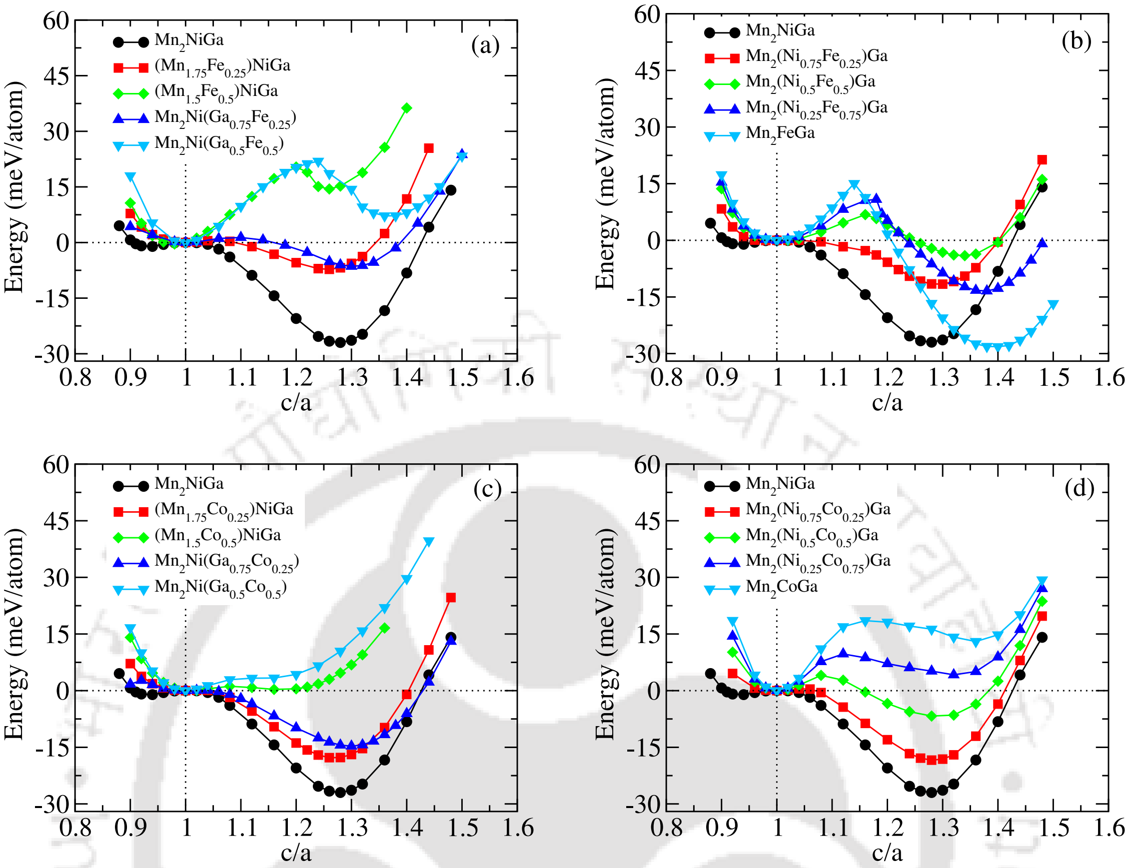

Figure 4.3: The variations of total energies as a function of c/a ratio for Fe and Co substituted Mn$_2$NiGa compounds. The zero energy is taken to be the energy of the austenite phase.

centration of Co when it is substituted at the Ni site, although the increase is very slow (about 0.1% maximum). Thus, the calculated trends are consistent with the experiments for most of the systems under consideration here.

In Fig. 4.2, we present the variations in formation energies of compounds with Fe or Co substituted at different sites in Mn$_2$NiGa as a function of the concentration of the substituent. We consider the bcc-Fe, hcp-Co, fcc-Ni, orthorhombic Ga, and antiferromagnetic bcc-Mn as ground state structure in their elemental phase. It can be seen that the formation energy is negative for all systems except Mn$_2$NiFe(E$_f$=0). This implies that except for Mn$_2$NiFe all the compounds can form in the the Hg$_2$CuTi structure from an enthalpy point of view. We have not come across any experimental result regarding Mn$_2$NiFe contradicting this finding. As some of the compounds under investigation such as Mn$_{2-x}$Fe$_x$NiGa(x=0-0.5) [239], Mn$_2$Ni$_{1-x}$Co$_x$Ga(x=0-0.5) and Mn$_2$NiGa$_{1-x}$Co$_x$(x=0-0.52) [240] have already been synthesized, our DFT calculations correctly reproduce the experimental observations and hence can provide guidance regarding the possibility of synthesizing the ones which have not been synthesized yet. Regarding the relative stabilities of compounds upon substitution of different atoms, our calculations imply that the substitution at different sites by Co is more favorable than substitution by Fe. Also the substitutions at the Ga sites make the compounds the least stable. By comparing the formation energies calculated here and in Ref. [241], we conclude that the Co substitution in Mn_2NiGa produces more stable compounds compared to the ones formed by substituting Fe or Cu. The origin of this lies in the differences in the electronic structures. We address this in Sec. 4.3.4

4.3.2 Martensitic phase transformation

From the point of view of functionality, it is important to investigate the sustainability of the martensitic transition of Mn_2NiGa upon substitutions by various atoms. Experiments on Co substitution at Ni and Ga sites [240] did not find any martensitic transformation beyond 16% of Co in the system. The measurements on $Mn_2Co_{0.08}Ni_{0.92}Ga$ and $Mn_2Co_{0.08}NiGa_{0.92}$ showed that T_m decreases rapidly to 125 K and 103 K respectively, from 270 K in the case of Mn_2NiGa. Fe substitution at the Mn site also led to a rapid decrease of T_m(120 K for $Mn_{1.7}Fe_{0.3}NiGa$) with no trace of martensitic transformation being observed beyond 30% of Fe. In this sub section, we examine the stabilities of the martensitic phases for all the compounds in order to find whether there is any trend with quantities such as (e/a) so that a predictor of variation in the T_m can be fixed. We do this by computing the total energy differences, ΔE, between the high-temperature Hg_2CuTi phases and the low-temperature non-modulated martensitic phases with tetragonal structure, the later being obtained by tetragonal distortion of the former. While ΔE does not provide an accurate quantitative estimate of T_m as that requires inclusion of various contributions to the free energy which are difficult to compute for a chemically disordered system, its variations with compositions help make a heuristic predictions on qualitative variations of T_m and the stability of the martensitic phases. Such an approach has been adopted elsewhere [241, 246] successfully.

In Fig. 4.3, we show the results of variations in the total energies with tetragonality(c/a) by keeping the volume constant at the equilibrium volume of Hg_2CuTi phases for each one of the Fe and Co substituted Mn_2NiGa systems. The reference energy in all cases is fixed at the one corresponding to (c/a)=1, the Hg_2CuTi phase. From Figs. 4.3(a) and (c), it can be seen that the Fe or Co substitutions at Mn or Ga sites reduce the stabilities of the martensite phases as the values of ΔE decrease(see Table-4.1) compared to the host Mn_2NiGa(ΔE=26.98 meV/atom) as the concentrations of the substituents increase. The total energy plots for ($Mn_{2-x}Fe_x$)NiGa show that for $x = 0.25$, the martensitic phase is almost destabilized; the ΔE decreases by a factor of more than 3 in comparison to the parent compound. At $x = 0.5$, the tetragonal phase is not even energetically favorable. These are in good agreement with the experimental observations as ΔE is considered as the predictor for T_m [239]. In the case of $Mn_2Ni(Ga_{1-x}Co_x)$, our calculated trends on the composition dependence of the martensitic transformation differs slightly from the experimental observations. In the experiments, no martensitic transformation was observed beyond $x = 0.16$ [240]. Our calculations, on the other hand, obtain a substantially deep energy minimum at (c/a) $\neq 1$ for $x = 0.25$, signifying the possibility of martensitic transformation at this composition. Qualitatively, though, this result is in agreement with the experimental observation as ΔE gradually decreases with x. The discrepancy can be due to consideration of only the total energy differences. Inclusion of various free-energy contributions can make the deep energy minimum vanish, in agreement with the experiment. We see the same trend of gradual destabilization of the martensitic phases with increasing concentration of the substituents for ($Mn_{2-x}Co_x$)NiGa and $Mn_2Ni(Ga_{1-x}Fe_x)$ systems. A comparison of the ΔE values for the systems presented in Figs. 4.3(a) and (c) indicates that Co-substituted systems have greater stability of the martensitic phases in comparison to Fe-substituted systems.

In Figs. 4.3(b) and (d), we compare the cases between Fe and Co substitutions, respectively, at the Ni sites. We find a gradual destabilization of the martensitic phase with increasing x for the $Mn_2(Ni_{1-x}Co_x)Ga$ system. A shallow minimum at a (c/a) $\neq 1$ for $x = 0.5$ followed by the absence of any minima for c/a $\neq 1$ for higher x indicate that martensitic transformation at reasonable temperatures might happen for up to $x = 0.25$. This, once again, is slightly different from the experimental observations that no traces of martensitic transformation were obtained for $x >$ 0.16 [240]. The case of $Mn_2(Ni_{1-x}Fe_x)Ga$ is somewhat different from the rest. Here, we see a gradual decrease in ΔE with x indicating the gradual destabilization of the martensitic phase up to $x = 0.5$. However, as x increases further, ΔE increases with the highest ΔE obtained for $x = 1$, that is, for the compound Mn_2FeGa. An inspection of the relative volume changes in Table 4.1 shows that for this system, the relative changes in volume with x are substantial and as large as 2.53% for Mn_2FeGa. Thus, although there is a cubic-to-tetragonal transformation, it is not volume conserving and thus is not martensitic in the context of shape memory properties. The physics of cubic-to-tetragonal phase transformation in Mn_2FeGa is very different which will be discussed in the next chapter, and thus the trends observed in our calculations do not suggest any anomalous behavior in this system.

A comparison with substituted Ni_2MnGa systems, at this point, is required to understand the similarities and differences between the two systems, in the context of impact of substitutions on the martensitic phase transformation. Unfortunately, there are not enough results available for substituted Ni_2MnGa which discuss the impact of substitution on the phase stability from the point of view of the nature of the energy surfaces as done in Fig. 4.3. The only work, to our knowledge, is available for Co-substituted Ni_2MnGa [245], where upto 25% of Co was substituted in Ni sites. Comparing our results to Ref. [245], we find that Co doping in Ni_2MnGa strongly affects the equilibrium (c/a) by gradually reducing it with increase in Co concentration, while there is hardly any change in the equilibrium (c/a) for the Co-substituted Mn_2NiGa. The reduction in (c/a) is indeed preferable for obtaining larger MFIS by lowering twinning stress [202] and thus the Co-substituted Ni_2MnGa would be better suited than Co-substituted Mn_2NiGa for actuator applications. A general feature of various substitutions in Mn_2NiGa, as observed in Fig. 4.3, is that the (c/a) hardly changes with concentration of the substituent, for the compositions where the tetragonal phase is having lower energy than the cubic phase. The only exception is Fe substituted at Ni sites in Mn_2NiGa for high concentrations of Fe. However, in contrast to Co-doped Ni_2MnGa, the equilibrium (c/a) increases with increasing Fe concentration in $Mn_2(Ni_{1-x}Fe_x)Ga$. Another difference between $(Ni_{1-x}Co_x)_2MnGa$ and $Mn_2(Ni_{1-x}Co_x)Ga$ energy surfaces is in the trends in the barrier height between austenite and martensite phases. While the barrier height decreases with increasing x in the former, the opposite happens in case of the latter. This implies that with increasing concentration of Co substituting Ni, in Mn_2NiGa, the austenite phase gains stability, in accordance with experimental trend. For $Mn_2(Ni_{1-x}Fe_x)Ga$, the change in the barrier heights with x is substantial. For $x = 0.5$ onwards, the barrier height is significantly high which implies that the inverse Heusler structure is gaining meta-stability with increasing x, and a transformation to a tetragonal structure would require substantial energy. The analysis in terms of the trends in the barrier height, thus, reaffirms that the cubic to tetragonal transformation in $Mn_2(Ni_{1-x}Fe_x)Ga$ for large x is not martensitic in nature.

Figure 4.3 and the tabulated (e/a) and ΔE values in Table 4.1 now suggest that the ΔE can be considered as a predictor for the qualitative variations in T_m.

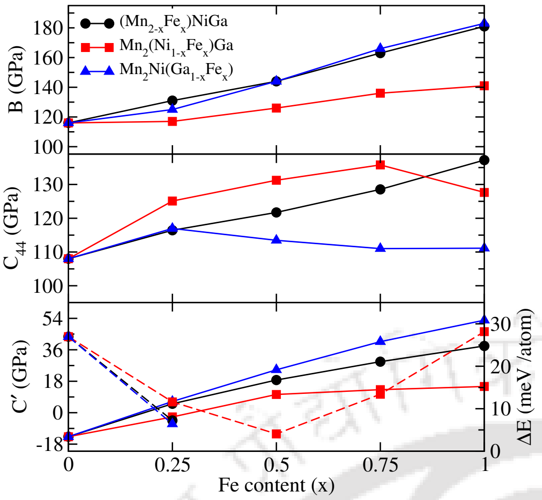

Figure 4.4: The calculated bulk modulus(B) and shear elastic constants C_{44} and C' as a function of Fe content at different sites in Mn_2NiGa. The dashed lines represent variations of ΔE with x; ΔE is defined in Table 4.1.

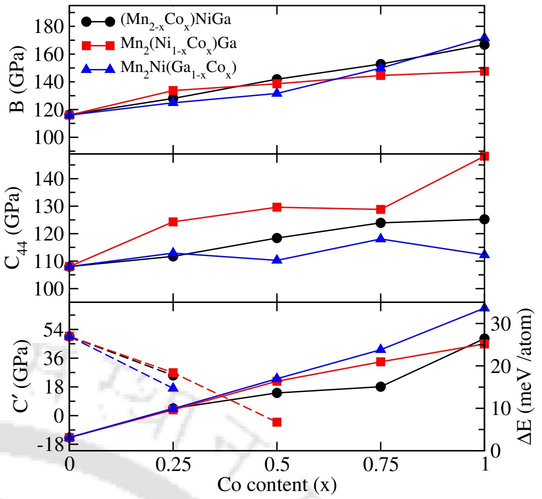

Figure 4.5: The calculated bulk modulus(B) and shear elastic constants C_{44} and C' as a function of Co content at different sites in Mn_2NiGa. The dashed lines represent variations of ΔE with x; ΔE is defined in Table 4.1.

However, in the systems under consideration, T_m versus (e/a) correlation is absent except in the $Mn_2(Ni_{1-x}Co_x)Ga$ system, suggesting that (e/a) would not be a good predictor for T_m. This is consistent with the experimental results [239, 240]. Summarizing, we find a universal trend of destabilization of the martensitic phase with increasing Fe or Co concentration, irrespective of the site at which they are substituted. The martensitic phases are stable mostly at low concentrations (up to $x = 0.25$) of the substituent. In the next subsections we analyze the reasons behind this.

4.3.3 Elastic properties

The composition-dependent variations in the elastic constants of the high temperature austenite phase having cubic symmetry can often be a predictor of the martensitic transformation for the Ni-Mn-Ga system [105, 246]. In Fe, Co, and Cu substituted Ni_2MnGa, it has been established that the shear modulus C' can be a better predictor of composition-dependent T_m [106, 241] than e/a since the martensitic transformations in these systems are related to the soft phonon modes which, in turn, are associated with the tetragonal shear elastic constant C' in the high-temperature austenite phase. In Mn_2NiGa, the mechanism of martensitic phase transformation is quite similar to Ni_2MnGa as discussed in chapter 1. So the cal-

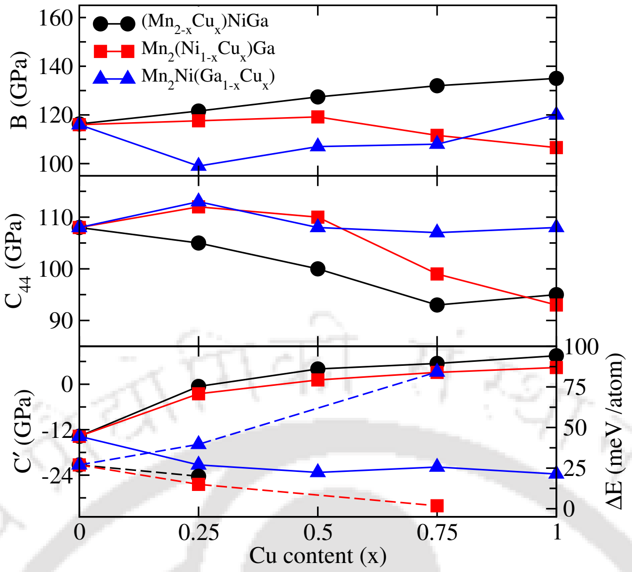

Figure 4.6: The calculated bulk modulus(B), shear elastic constants C_{44} and C' as a function of Cu concentration at different sites in Cu-substituted Mn_2NiGa. The dashed lines represent variations of ΔE with x; ΔE is defined in Table 4.1. The value of ΔE are taken from the Ref. [241]

culation of C' along with other elastic constants would be useful to verify whether C' can be a good predictor of the composition dependence of martensitic transformation apart from the fundamental understanding of the composition dependence of the mechanical stability of these systems.

In Figs. 4.4 and 4.5, we present the results of calculated bulk modulus and shear moduli C_{44} and C' for Fe and Co substituted Mn_2NiGa. For all systems, the bulk modulus increases as the volume decreases which is consistent with the expected general trend. The elastic modulus C_{44} is positive for all the alloys which satisfies one of the stability criteria for crystals with cubic symmetry. The value of C' increases with increasing Fe or Co concentration which indicates that the system is increasingly insusceptible to a martensitic transformation. Negative or very low values of C' up to 25% of the substituent concentration for all systems are consistent with the obtained trends in the total energy minima with compositions (Fig. 4.3). For $Mn_2(Ni_{1-x}Fe_x)Ga$ system, we notice that the C' is almost constant beyond $x = 0.25$ as opposed to the increasing trend (with x) for other systems. This is, once again, consistent with the fact that at all compositions in this particular system, the cubic phase transforms to a tetragonal phase with large energy cost, in particular for $x > 0.5$, although such a phase transformation is not a volume-conserving martensitic one. The important outcome of the variations in the C' with compositions is that it can be considered as a better predictor of the composition dependence of T$_m$. In the previous subsection, we have demonstrated that ΔE is a good predictor of the martensitic transformation. However, in order to fix a predictor, one needs a physically measurable quantity. The justification of considering C' as the one can be understood by looking at the variations of C' with ΔE as shown in Figs. 4.4 and 4.5. The C' has an inverse relationship with ΔE which is according to our expectations; the former indicating increasing difficulty in destabilizing the Hg_2CuTi structure against tetragonal shear while the latter stands for the possibility of obtaining a martensitic transformation. Another significance of this result is that one can immediately find a similarity with regard to fixing C' as the predictor of the composition dependence of T$_m$ in Fe, Cu, and Co substituted Ni_2MnGa systems. To make sure that this is indeed true in cases of substitutions of all of these three atoms in Mn_2NiGa also, we have plotted the variations of B, C_{44} and C' with concentration of the substituent for Cu substitution in various sites of Mn_2NiGa, shown in Fig. 4.6. We see the same inverse relationship between C' and ΔE in this system as well. Thus, we can conclude that C' can be considered as the predictor of the composition dependence of martensitic phase transformation in the Ni-Mn-Ga alloy system, irrespective of substitution by another magnetic atom.

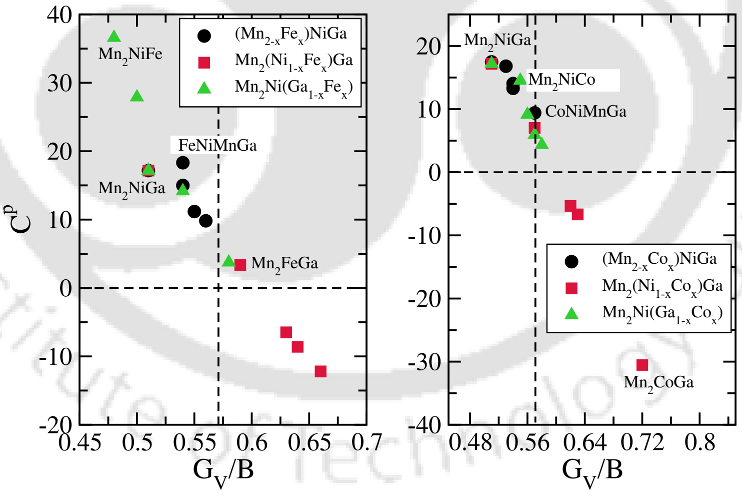

Figure 4.7: Variations in the Cauchy pressure $C^p = (C_{12} - C_{44})$ with Pugh ratio G_v/B are plotted for all the compounds. According to Ref. [140], $C^p > 0, G_v/B < 0.57$ indicates more ductility and more components of metallic bonding while $C^p < 0, G_v/B > 0.57$ indicates more brittleness and stronger covalent bonding.

One of the reasons for substituting another magnetic atom into Mn_2NiGa is to improve its mechanical properties, such as ductility. A good measure of whether the system is more ductile or more brittle is to look at its Pugh ratio [139] given as G_v/B [136, 254, 255], G_v the isotropic shear modulus under Voigt formalism [135]

Table 4.2: Elastic constants of Co and Fe substituted Mn_2NiGa in their Hg_2CuTi cubic phases.

System	B (GPa)	C' (GPa)	C_{44} (GPa)	C_{11} (GPa)	C_{12} (GPa)	G_v (GPa)	G_v/B	$C^p = C_{12} - C_{44}$ (GPa)
Mn_2NiGa	116	-13.75	108	97.67	125.17	59.3	0.51	17.17
$(Mn_{0.75}Fe_{0.25})NiMnGa$	131	5.1	116.43	137.8	127.6	71.9	0.55	11.17
$(Mn_{0.5}Fe_{0.25})NiMnGa$	144	18.69	121.72	168.92	131.54	80.51	0.56	9.82
$(Mn_{0.25}Fe_{0.75})NiMnGa$	163	29.2	128.54	201.93	143.53	88.8	0.54	14.99
FeNiMnGa	181	38.18	137.23	231.91	155.55	97.61	0.54	18.32
Mn_2NiGa	116	-13.75	108	97.67	125.17	59.3	0.51	17.17
$Mn_2(Ni_{0.75}Fe_{0.25})Ga$	117	-2.41	125.1	113.79	118.61	74.1	0.63	-6.49
$Mn_2(Ni_{0.5}Fe_{0.5})Ga$	126	10.42	131.25	139.89	119.05	82.92	0.66	-12.2
$Mn_2(Ni_{0.25}Fe_{0.75})Ga$	136	13.2	135.8	153.6	127.2	86.76	0.64	-8.6
Mn_2FeGa	141	15	127.64	161	131	82.58	0.59	3.36
Mn_2NiGa	116	-13.75	108	97.67	125.17	59.3	0.51	17.17
$Mn_2Ni(Ga_{0.75}Fe_{0.25})$	125	6.44	116.96	133.59	120.71	72.75	0.58	3.75
$Mn_2Ni(Ga_{0.5}Fe_{0.5})$	144	24.56	113.46	176.75	127.63	77.9	0.54	14.17
$Mn_2Ni(Ga_{0.25}Fe_{0.75})$	166	40.66	111	220.21	138.89	82.86	0.5	27.89
Mn_2NiFe	183	52.94	111.12	253.59	147.71	87.85	0.48	36.59
Mn_2NiGa	116	-13.75	108	97.67	125.17	59.3	0.51	17.17
$(Mn_{0.75}Co_{0.25})NiMnGa$	128	4.5	111.71	133.99	125	68.82	0.54	13.29
$(Mn_{0.5}Co_{0.25})NiMnGa$	142	14.21	118.39	160.84	132.43	76.72	0.54	14.04
$(Mn_{0.25}Co_{0.75})NiMnGa$	153	18.11	123.93	176.94	140.73	81.6	0.53	16.8
CoNiMnGa	167	48.27	125.22	231.17	134.62	94.44	0.57	9.4
Mn_2NiGa	116	-13.75	108	97.67	125.17	59.3	0.51	17.17
$Mn_2(Ni_{0.75}Co_{0.25})Ga$	133.7	3.61	124.28	138.51	131.29	76.01	0.57	7.01
$Mn_2(Ni_{0.5}Co_{0.5})Ga$	138.6	21.51	129.61	167.28	124.26	86.37	0.62	-5.35
$Mn_2(Ni_{0.25}Co_{0.75})Ga$	144.6	33.7	128.81	189.54	122.13	90.77	0.63	-6.38
Mn_2CoGa	147.6	44.93	148.18	207.51	117.65	106.88	0.72	-30.53
Mn_2NiGa	116	-13.75	108	97.67	125.17	59.3	0.51	17.17
$Mn_2Ni(Ga_{0.75}Co_{0.25})$	124.9	4.3	112.9	130.63	122.03	69.46	0.56	9.13
$Mn_2Ni(Ga_{0.5}Co_{0.5})$	131.6	23.09	110.28	162.38	116.21	75.4	0.57	5.93
$Mn_2Ni(Ga_{0.25}Co_{0.75})$	149.9	41.29	118.04	204.95	122.37	87.34	0.58	4.33
Mn_2NiCo	171.7	67.36	112.26	261.52	126.79	94.3	0.55	14.53

related to the resistance of the material to plastic deformation and B the bulk modulus. A G_v/B value of 0.57 is considered critical to decide on the brittleness of the compound. Compounds having a Pugh ratio greater than 0.57 are considered more brittle. On the other hand, Cauchy pressure, defined as $C^p = (C_{12} - C_{44})$, provides an insight to the nature of bonding in a material with cubic symmetry [256]. According to this, a positive value of Cauchy pressure indicates the presence of more metallic bonding in the system while a negative value implies a stronger component of covalent bonding. Very recently, Niu *et al.* have shown that the Pugh ratio and Cauchy pressure are well correlated with their ductile-to-brittle transition, matching with the metallic-to-covalent bonding transformation for a number of cubic crystals [140]. In Fig. 4.7, we plot the Pugh ratio versus Cauchy pressure for all the compounds studied here. For better understanding of the trends for each type of substitution, the values of the elastic moduli are given in Table 4.2. The results as displayed in Fig. 4.7 imply that there is a correlation between C^p and (G_v/B) as suggested in Ref. [140] and seen in case of a group of Co_2- and Ni_2-based Heusler alloys [255]. However, the absolute numbers in Table 4.2 suggest that for a given group of systems, that is, systems obtained by gradual substitution of a particular atom at a particular site of Mn_2NiGa, this correlation does not necessarily hold. For example, one can see a linear variation between C^p and (G_v/B) in $(Mn_{2-x}Fe_x)NiGa$ for $x \leq 0.5$ after which C_p increases with almost no variation in (G_v/B). Overall, the results imply that the systems are very close to the ductile-brittle critical limit and that the bonding has more metallic component; the two notable exceptions are when Co or Fe is substituted at the Ni site. As the Ni content in the system decreases, we observe the tendency of the system to be more brittle and the bonding having a more covalent component. Mn_2CoGa has the highest (G_v/B) ratio of 0.72 which is close to Si and Ge [140] along with a large negative C^p. The effect is not as dramatic in the case of $Mn_2(Ni_{1-x}Fe_x)Ga$ although a high value of (G_v/B), 0.66, along with a C^p value -12.2 are obtained for $x = 0.5$. Beyond $x = 0.5$, the system tends to be more metallic and ductile although the numbers for $x = 0.75$ and 1 are closer to the transition lines. Thus, the bonding features in cases of substitutions at the Ni site must be different from the rest.

4.3.4 Electronic structure

The results in the previous two subsections demonstrate that the austenite phase gets gradually stabilized as the concentration of the substituent in any one of the sites of Mn_2NiGa increases. For most of the systems investigated, a concentration (of the substituent) beyond 25% leads to a complete stabilization of the cubic austenite phase. At the same time, one sees that except for substitutions at the Ni site, the bonding remains dominantly metallic in nature. In this subsection we try to understand the reasons behind these trends from the composition-dependent variations of the electronic structures in the substituted Mn_2NiGa systems. To do this, we have plotted the total densities of states of compounds where Fe and Co are substituted in various sites. The results for Fe substitution at different sites are shown in Fig. 4.8 and those for Co substitution at different sites are shown in Fig. 4.9.

In the Hg_2CuTi phase of pristine Mn_2NiGa, there exists a pseudogap in the minority spin band at about 1 eV below the Fermi level. This pseudogap is formed

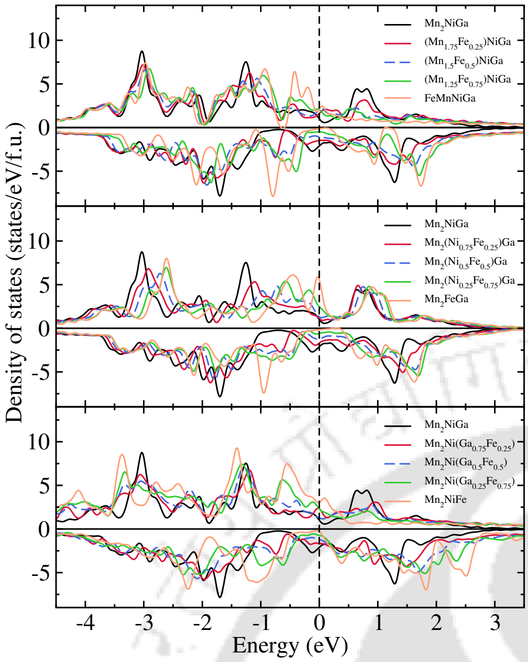

Figure 4.8: Total density of states for Fe substituted at different sites in Mn_2NiGa. The zero of the energy is set at Fermi energy(E_F).

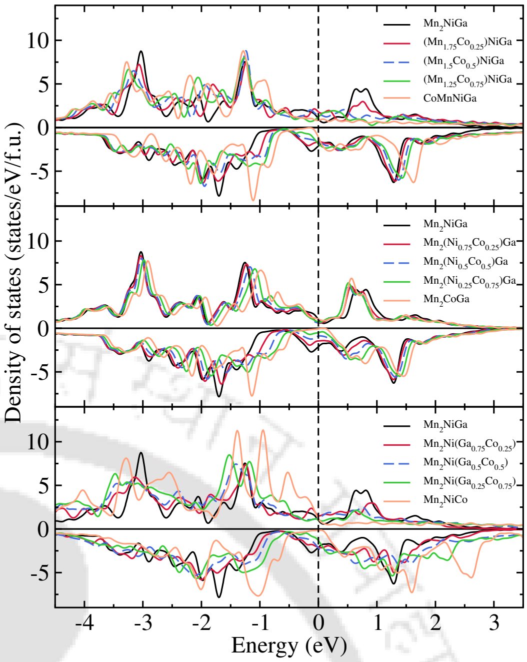

Figure 4.9: Total density of states for Co substituted at different sites in Mn_2NiGa. The zero of the energy is set at Fermi energy(E_F).

mainly due to the hybridizations between the $3d$ states of MnI and Ni which occupy symmetric positions in the Hg_2CuTi lattice and the $4p$ states of Ga. A peak around 0.1 eV below Fermi level, originating from the hybridizations of the same orbitals, results in the Jahn-Teller instability in the system [66, 77, 78] and drives the system towards the martensitic transformations. The stabilities of the martensitic phases as obtained from the total energy calculations, the variations in the elastic moduli, and proposed changes in the strengths of bonding upon substitutions can now be interpreted from the minority spin band densities of states. The elastic constant C' is directly connected to the Jahn-Teller distortion since it is the elastic modulus of tetragonal deformation. Thus, a stronger covalent bond or weaker Jahn-Teller distortion should result in a harder C'.

Figs. 4.8 and 4.9 clearly show that substitutions weaken the Jahn-Teller distortion in Mn_2NiGa as the peak around -0.1 eV gradually gets smeared out, thus stabilizing the Hg_2CuTi structure. This explains the gradual stabilization of the austenite phases with concentrations of the substituents as seen in Fig. 4.3. Irrespective of the site at which the substitution is done, it is either MnI or Ni content that decreases at the 4a and 4b sites weakening the hybridizations between their $3d$ and Ga $4p$ states. The substituents, either Co or Fe cannot restore the hybridization as their $3d$ states in the minority bands lie much deeper. Such weakening of the Jahn-Teller distortion upon substitutions is the reason behind hardening of C' with increasing substituent content in Mn_2NiGa.

As seen from Figs. 4.8 and 4.9, for the $Mn_{2-x}X_xNiGa$ (X=Fe, Co) systems, the pseudogap at about -1 eV in the minority bands gradually becomes narrower and shallower for X=Fe. This happens primarily due to the position of the Fe-d states which are right in the gap. The weakening of the Jahn-Teller distortion gradually pushes the MnI and Ni states towards lower energies, making them hybridize with Fe states within 0.3 eV to 0.75 eV below Fermi level. Thus, initially for $x \leq 0.5$, the covalent bond strength in the system increases and is reflected in the changes in C^p (Table 4.2). Beyond $x = 0.5$, the MnI content reduces weakening the covalent bonding slightly(C^p values increase again along with a decrease in the (G_v/B)). In the case of X=Co, the situation is slightly different. The Co states lie deeper than Fe states, but the hybridizations with Ni and MnI states which are pushed into the pseudogap due to weakening of the Jahn-Teller effect hybridize with the Co states in a way similar to Fe. The only noticeable difference in the two cases is that while the Fe states are more delocalized towards higher energies, the Co states are localized strengthening the covalent components in the bonding. Such stronger covalent bonding in Co-substituted compounds explains the relative stabilities of the Co-substituted and Fe-substituted compounds as depicted in Fig. 4.2. In both cases the pseudogap moves towards higher energies but in the case of the Fe substitution it morphs into a real gap cutting through the Fermi level. A look at the majority spin densities of states can also help in understanding the evolution of the bonding strengths. For the Fe-substituted systems, more states pile up near the Fermi level when $x > 0.5$ due to increased hybridization of MnII, Fe, and Ga states contributing to more metallicity in the bonds. In the case of Co substitution at the MnI site, there is very little changes in the majority band densities of states and thus the evolution in the bonding nature is to be understood from the features in the minority band densities of states.

In the case of $Mn_2Ni(Ga_{1-x}Fe_x)$, the minority band densities of states are dominated by Fe states weakly hybridizing with other atoms. The Fe states are more delocalized except for $x = 0.25$. However, MnI and Ni hybridize strongly for $x = 0.25$ with the strength gradually diminishing. The majority band densities of states have noticeable changes near the Fermi level with increasing x and beyond $x = 0.25$, the major highlight being a peak and larger densities of states at the Fermi level owing to hybridizations of Fe and MnIII states. This explains the more covalent

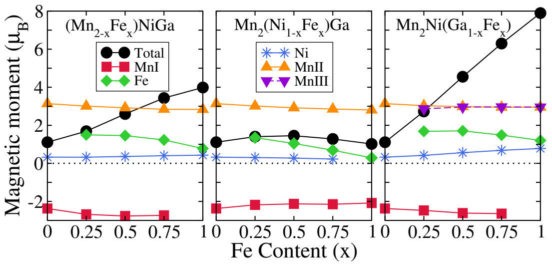

Figure 4.10: The calculated total ($\mu_B/f.u.$) and atomic magnetic moment as a function of Fe content for Fe-substituted Mn_2NiGa.

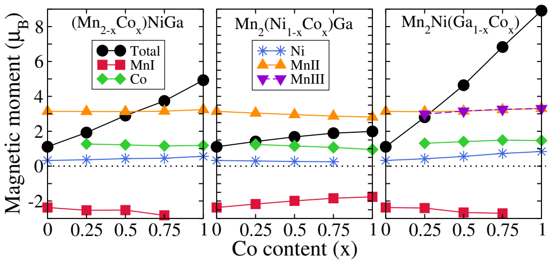

Figure 4.11: The calculated total ($\mu_B/f.u.$) and atomic magnetic moment as a function of Co content for Co-substituted Mn_2NiGa.

nature of the bonds for $x = 0.25$ and more metallic for higher x. In the case of $Mn_2Ni(Ga_{1-x}Co_x)$, there is little change in the majority spin densities of states up to $x = 0.75$. In the minority band, Co has greater contributions but it hybridizes weakly with other atoms while the stronger hybridizations are between Ni and MnI in the intermediate concentrations. This means that the covalent bonding gets strengthened supporting the results of Table 4.2. The absence of MnI atoms at $x = 1$, along with sharp contributions from MnIII near the Fermi level in the majority spin band, weakens the covalent bond strengths and makes the system more metallic.

From Table 4.2, it appears that the substitution at Ni sites makes the covalent bonds stronger and it prevails for Co substitution, in particular. For Co-substituted systems, we find that that there is very little change in the overall features of the majority band densities of states as the Co-content increases. The major changes occur in the minority spin band where Co, MnI, and Ni hybridize. As the Ni content decreases, the hybridizations between Co and MnI (in the range of -1.25 eV to -0.5 eV) gets stronger making the character of the bonds more covalent. In case of Fe substitution the stronger covalent component in their bonds can be explained in a similar way up to $x = 0.5$. However, at $x = 0.75$, a peak appears close to the Fermi level due to Fe-MnI hybridization, which transforms to a large peak exactly at the Fermi level for $x = 1$, thus increasing the metallic contributions to the bonds. This picture is consistent with the results from Table 4.2.

The electronic structures clearly point out a major difference between substituted Ni_2MnGa and Mn_2NiGa systems. The electronic structures of austenite phases of both the compounds, in their pristine forms, have the pseudo-gap indicating covalent bonding and the Jahn-Teller peak coming near or at the Fermi level, both occurring due to hybridizations between the elements occupying the 4a, 4b, and 4d sublattices.

In Ni_2MnGa the hybridization occurs between Ni and Ga while in Mn_2NiGa, Ni, MnI and Ga participate in the bonding. In the case of substitutions in Ni_2MnGa, the Jahn-Teller instability is sustained when substitutions are done at the Ga and Mn sites, which is reflected in the increasing height of the Jahn-Teller peak at the Fermi level [106]. This correlates well with the experimental observation of the increase in T_m with increasing concentration of the substituent. The substitutions at Ni sites in Ni_2MnGa, on the other hand, lead to gradual lowering of the height of the Jahn-Teller peak [106, 245] signifying increasing stability of the austenite phase and subsequent decrease in T_m. The sustaining Jahn-Teller instability for cases where substitutions are done at Ga and Mn sites is due to the fact that Ni is not involved in these cases. The substitutions at the Ni sites weaken the Ni-Ga hybridizations and relive the Jahn-Teller instability. Substitutions at any of the three sites (MnI, Ni and Ga) of Mn_2NiGa diminish the Jahn-Teller effect as all three atoms are involved in producing the peak associated with it. Thus, irrespective of the site of substitution, we see the manifestation of decreasing Jahn-Teller effect by reduction in the peak height at or near the Fermi level with increasing concentration of the substituent. This explains why T_m decreases with substitution at any site in Mn_2NiGa while this is not the case for substituted Ni_2MnGa. Another distinctive outcome of substitutions in Mn_2NiGa is the emergence of a half-metal-like gap which grows as the concentration of the substituent increases and finally cuts through the Fermi level when substitution is complete ($x = 1$) producing materials with high spin polarization, which could be useful in spintronics. This is very different from what is obtained in substituted Ni_2MnGa. While the substitutions in both the systems fill the pseudo-gap in the minority band, thus making it narrow, in the case of Mn_2NiGa, the substitutions diminish the Jahn-Teller peaks considerably as either MnI, Ni, or Ga content is reduced. Along with this, the positions of the substituent levels are deep within the minority band, producing a gap across the Fermi level. This is not the case for substituted Ni_2MnGa.

4.3.5 Total and atomic magnetic moments

In Table 4.1 and Figs. 4.10 and 4.11 we present our results on total and atomic magnetic moments to understand the effects of site substitution in Mn_2NiGa in the Hg_2CuTi phase. Magnetization measurements on $(Mn_{2-x}Fe_x)NiGa$ [239], $Mn_2(Ni_{1-x}Co_x)Ga$, and $Mn_2Ni(Ga_{1-x}Co_x)$ [240] systems showed an increase in magnetization upon Fe and Co substitutions. From our results, we summarize the observations on the total magnetic moments: (i) In almost all cases the total moment increases with the concentration of the substituent. (ii) The rise in the total moment is fastest for $Mn_2Ni(Ga_{1-x}X_x)$, and is slowest for $Mn_2(Ni_{1-x}X_x)Ga$ systems. (iii) The variation of total moment with x is non-linear for $Mn_2(Ni_{1-x}Fe_x)Ga$. It increases for $x \leq 0.5$ and then decreases for higher values of x. However, this is consistent with the substantial changes in the electronic structures discussed in the previous subsection. (iv) All the compounds formed by complete substitution of one of the atoms in the parent compound ($x = 1$) have near-integer moments with the highest being $\sim 9\mu_B$ for Mn_2NiCo.

The calculated results agree very well with the ones available in the literature, obtained either in the magnetic measurements [239, 240] or from the first-principles calculations [85, 208, 241, 248]. For $(Mn_{2-x}Fe_x)NiGa$ ($x = 0.25, 0.5$) compounds, the calculated results of magnetic moments are consistent with experiment [239]. The noticeable disagreements are in the cases of $Mn_2Ni(Ga_{1-x}Co_x)(x = 0.25, 0.5)$ [240], MnCoNiGa [232, 248] and MnFeNiGa [248] compounds. The disagreement in the case of $Mn_2Ni(Ga_{1-x}Co_x)$ could be because of the presence of antisite disorder in the experimental sample or due to the differences between actual composition and the one reported in the experiment [240]. Both the effects can affect the magnetic moment as it is found to be very sensitive to the sublattice composition in Ni-Mn-Ga systems [106]. The cases of MnCoNiGa and MnFeNiGa are quite insightful. DFT calculations on both compounds with a stacking identical to that obtained by replacing MnI with Co or Fe is in excellent agreement with our results, [248] both producing near-integer moments and a half-metal-like gap in the minority band densities of states. However, the magnetization measurements at low temperature obtained saturation moments which are far from being integers [248]. The same compounds can be obtained by substituting Co or Fe at Ni sites in Ni_2MnGa. Magnetization measurements and DFT calculations for Co-substituted Ni_2MnGa compound with equal amounts of Co, Ni, Mn, and Ga reported noninteger magnetic moments [232] with values in excellent agreement with the experimental results reported in Ref. [248]. The origin of such discrepancies, probably, is in the differences in the site preferences if one obtains the same compounds by substitutions in Mn_2NiGa and in Ni_2MnGa. In the case of the former, we have explained why the stacking is Co(4a)-MnII(4c)-Ni(4b)-Ga(4d) in Sec. 4.3.1. This comes out to be the minimum energy stacking for CoNiMnGa [248]. In the case of substitutions of Co at the Ni sites in Ni_2MnGa, the expected stacking would be (Ni-Co)(4a)-Mn(4c)-(Ni-Co)(4b)-Ga(4d). This is because, in Heusler Ni_2MnGa, the Ni sites are crystallographically equivalent, and thus the substituent Co would not prefer one Ni site over the other and would occupy both in equal proportions keeping the symmetry of the lattice intact. The noninteger magnetic moment as obtained experimentally and by DFT calculations [232] must be due to this. This might be true in the case of magnetization measurements in quaternary MnCoNiGa and MnFeNiGa, although they are not obtained by the above-mentioned substitution route. One needs to investigate the energetics associated with different site occupancies in these compounds to resolve the issue. The importance of the observed discrepancy in CoNiMnGa magnetic moment is in establishing that the site substitutions and subsequent properties can be very different in the two pristine compounds.

The changes in the compositions at various sites affect the atomic moments which in turn affect the variations in the total magnetic moments with the concentration of the substituents. From Figs. 4.10 and 4.11, we find the following trends: (i) Like Mn_2NiGa, MnI and MnII atoms couple antiparallel in all compounds where MnI is present. (ii) The moment of MnII atoms undergoes little variation with the composition across all compounds, the general trend being a small decrease with the concentration of the substituent. (iii) The moment associated with the Ni atoms increases with concentration of the substituent except when it is substituted by Fe or Co; the faster increase is in cases of substitutions at Ga sites. (iv) The MnI magnetic moments increase slightly in magnitude making the antiferromagnetic component in the system stronger as the concentration of the substituent increases for all systems except when substitutions are done at Ni sites, where its magnitude decreases signifying increase in the ferromagnetic component in the system; the change is more rapid in the case of Co substitution at the Ni site. (v) For the Ga-substituted systems, MnIII, the Mn atoms at the Ga sites have large ferromagnetic moments, almost equal in magnitude to MnII moments; as the concentration of the substituent increases the concentration of MnI(MnIII) decreases(increases) weakening the antiferromagnetic component in favor of a strong ferromagnetic one. This explains the rapid increase of the total moment for these systems. (vi) The Co moment is larger than the Ni moment and undergoes little change across compositions and the site of substitution while the Fe moment has a general trend of decreasing with increasing Fe concentration. A rapid quenching of Fe moment is observed in the case of Mn_2FeGa, the reason of which will be discussed in the next chapter. The slow increase in the total moment for Ni-substituted systems, thus, can be understood in terms of the losses of MnII and MnI moments concurrently but in opposite directions, leaving the changes to be governed solely by Ni and the

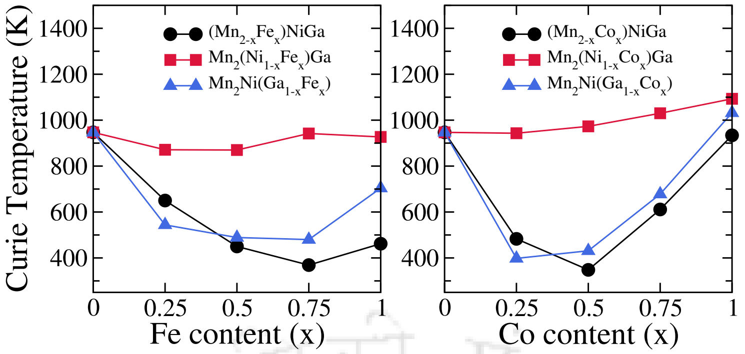

Figure 4.12: Calculated Curie temperatures as a function of substituent (a) Fe concentration and (b) Co concentration for substitutions at different sites in Mn_2NiGa. Calculations are done by the MFA method.

substituent moments, both of which vary slowly across compositions. The linear increase in the total moment of the Mn-substituted system, on the other hand, can be attributed to the gradual loss of contributions of MnI due to its decreasing concentration which boosts the ferromagnetic component in the system with concentration of the substituent.

4.3.6 Magnetic exchange interactions and Curie temperature

In Figs. 4.12 and 4.13, we show the composition dependencies of Curie temperatures (T_c) calculated using the mean-field approximation (MFA) and Monte Carlo simulation (MCS), respectively, for Fe and Co substituted Mn_2NiGa. Since the MFA results typically overestimate the T_c and MCS results are found to be closer to experimental results for a variety of systems, the available experimental results in these compounds are included in Fig. 4.13. The trends in variations of T_c calculated using MFA and MCS are by and large similar. As expected, the MFA results are overestimated in comparison with the MCS results and the experimental values. From the MCS results, we find that all the end compounds obtained by complete substitution of Fe or Co in any of the sites have very high T_c, the largest being close to 900 K for Mn_2NiCo. The qualitative variation of T_c for $Mn_2(Ni_{1-x}Co_x)Ga$ agrees well with the experiment [240, 257] although the MCS results are a little overestimated. The quantitative agreement between the MCS results and the experimental results [239, 248] for $(Mn_{2-x}Fe_x)NiGa$ is better. There is significant disagreement, both qualitatively, and quantitatively for $Mn_2Ni(Ga_{1-x}Co_x)$ systems. The MCS calculations show a sharp decrease in T_c for 25% Co substitution after which the

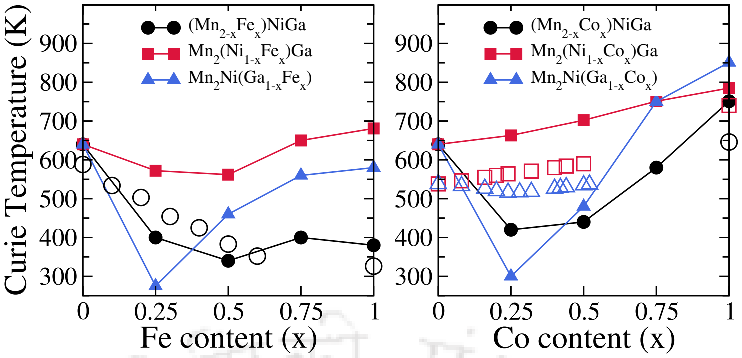

Figure 4.13: Calculated Curie temperatures as a function of substituent (a) Fe concentration and (b) Co concentration for substitutions at different sites in Mn_2NiGa. Calculations are done by the MCS method. Open symbols represent the experimental results which are adopted from Refs. [239, 240, 248, 257].

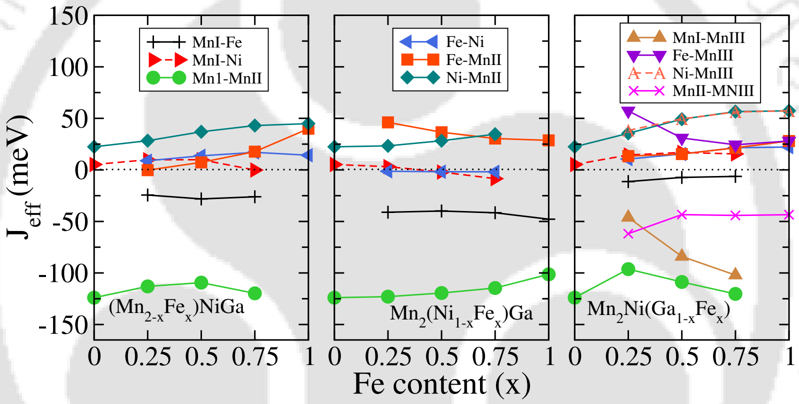

Figure 4.14: Effective exchange coupling constant (J_{eff}) as a function of Fe content at different sites in Mn_2NiGa.

T_c rises sharply with increase in x. For the experiment [240], on the other hand, although a decrease in T_c up to $x = 0.24$ and a rise after that were obtained, the changes were not this substantial. The experimentally obtained T_c decreased from 538 K ($x = 0$) to 517 K for $x = 0.24$ and rose to only 537 K for $x = 0.52$. It may be noted that their T_c for Mn_2NiGa is lower by 50 K in comparison to T_c obtained from other experiments [64, 239]. Such discrepancies could be due to antisite disorder or off-stoichiometric compositions present in the samples used by the authors of Ref. [240]. In fact, we have reported discrepancies in the magnetic moments calculated by us and obtained from their magnetic measurements in the previous subsection. Thus the origin of these discrepancies could be the same. Nevertheless, the agreement between the MCS results and the experiments for the end compounds, wherever available, is remarkable.

In order to understand the trends in the Curie temperature, we have calculated

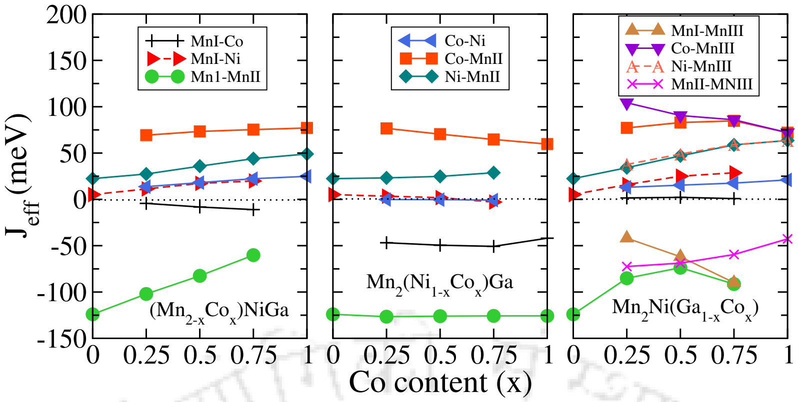

Figure 4.15: Effective exchange coupling constant (J_{eff}) as a function of Co content at different sites in Mn_2NiGa.

the inter-atomic magnetic effective exchange coupling(J_{eff}), presented in Figs. 4.14 and 4.15 for Fe and Co substituted Mn_2NiGa, respectively. The J_{eff} are calculated as $J^{\mu\nu}_{eff} = \sum_j J^{\mu\nu}_{0j}$, 0 fixed to sub-lattice μ and the sites j belonging to sublattice ν. We find that the dominant J_{eff}s remain either antiferromagnetic or ferromagnetic across compositions. The dominant antiferromagnetic J_{eff} is due to the MnI-MnII pairs while the other dominant inter-sublattice J_{eff} s are ferromagnetic. For the $(Mn_{2-x}Co_x)NiGa$ system, the strength of antiferromagnetic $J^{MnI-MnII}_{eff}$ decreases with x while the strength of the largest ferromagnetic effective exchange interaction, $J^{Co-MnII}_{eff}$, increases with x. This is because of the increasing hybridizations between nearest-neighbor Co and MnII which couple parallel resulting in the weakened antiferromagnetic nearest-neighbor MnI-MnII exchange interaction as the system gradually becomes MnI deficient (Co excess). The increasing ferromagnetic exchange interaction between nearest-neighbor Ni and MnII and next-nearest-neighbor Ni-MnI and Ni-Co gives rise to an increase in the overall ferromagnetic interaction. Up to $x = 0.25$, there is a competition between the ferromagnetic and antiferromagnetic interactions which brings T_c down. Beyond $x = 0.25$, the ferromagnetic components overwhelm the antiferromagnetic interactions resulting in the rise of T_c for higher values of x. In contrast, for $(Mn_{2-x}Fe_x)NiGa$, the $J^{MnI-MnII}_{eff}$ remains nearly constant with x. The strength of the ferromagnetic Fe-MnII, Fe-Ni, and MnI-Ni in these compounds is weaker in comparison to those in $(Mn_{2-x}Co_x)NiGa$ with the Ni-MnII exchange interaction having nearly the same strength and larger than the Fe-MnII one, exactly opposite to the Co-substituted compound. Such weaker ferromagnetic interactions might be the result of weaker Fe-MnII hybridizations. This weak interaction of MnII with one of the components in the 4a site keeps the strength of the interaction with the other component, MnI, at the same site intact across compositions although the concentration of MnI decreases gradually. This manifests itself in bringing down the T$_c$ considerably in (Mn$_{2-x}$Fe$_x$)NiGa for low x and keeping it almost like that as x increases.

For Mn$_2$(Ni$_{1-x}$Co$_x$)Ga and Mn$_2$(Ni$_{1-x}$Fe$_x$)Ga, we find the variations in the exchange interactions quite similar, qualitatively and quantitatively. The antiferromagnetic MnI-MnII interactions remain largely unaffected across compositions as the substitutions are not done in either of these sites. The inter-sublattice antiferromagnetic MnI-Fe and MnI-Co second-neighbor interactions are found to be substantial and identical in strengths. The strongest ferromagnetic interaction in the Co-substituted system is that of Co-MnII pairs while the strength of the Ni-MnII interaction is considerably weaker across the concentration range. In the case of Fe-substituted system, though the strongest ferromagnetic interaction is due to Fe-MnII pairs for smaller x values, the strength of Ni-MnII interactions quickly catches up with it. Thus, the initial decrease in T$_c$ for Mn$_2$(Ni$_{1-x}$Fe$_x$)Ga is due to weakening of the overall ferromagnetic interactions, primarily due to weak Fe-MnII hybridizations. For higher x, the $J_{eff}^{Ni-MnII}$ compensates for the $J_{eff}^{Fe-MnII}$, strengthening the ferromagnetic interactions in the system leading to an increase in T$_c$ with x. For Mn$_2$(Ni$_{1-x}$Co$_x$)Ga, the strong ferromagnetic exchange interactions for all x values lead to an increase in T$_c$ with x.

In systems with substitutions done at Ga sites, a greater number of interactions compete with each other as Mn atoms are present at three different sites. The antiferromagnetic interactions are due to nearest neighbor MnI-MnII and MnI-MnIII and second neighbor MnII-MnIII. The ferromagnetic components in the exchange interactions are due to nearest neighbors X-MnIII (X=Co, Fe), X-MnII, Ni-MnII, and Ni-MnIII and second neighbor Ni-MnI. For X=Co, that is, when Ga is replaced with Co, the antiferromagnetic MnI-MnII interaction loses its strength as does the second-neighbor antiferromagnetic MnII-MnIII interaction while the nearest-neighbor MnIII-MnI interaction becomes more antiferromagnetic as concentration of Co increases. Among the ferromagnetic interactions, except for Co-MnIII which decreases with concentration of Co, the other three increase. Strong hybridizations of Co with MnII and MnIII atoms are responsible for the strong ferromagnetic interactions in this system. This was predicted earlier [240] without explicit computations of the exchange interactions. Our calculation corroborates this with quantitative estimates. The antiferromagnetic exchange interactions behave the same way in systems with X=Fe. The ferromagnetic components for Fe-substituted systems are much weaker than those for Co-substituted systems. In fact, although Fe-MnIII was the strongest ferromagnetic interaction initially, it drops fast giving way to Ni-MnII and Ni-MnIII. As Fe concentration increases, the Fe majority spin states move towards higher energies in comparison with MnII/MnIII states, thus making the hybridizations weaker. The weaker ferromagnetic components in Fe-substituted systems explain their smaller T_c values, in comparison to Co-substituted systems, particularly for higher x values. In both systems, the sharp decrease at $x = 0.25$ is due to relatively stronger antiferromagnetic interactions. As x increases, the ferromagnetic interactions build up, effecting an increase in T_c.

4.4 Conclusions

In this chapter, we have performed an in depth investigations of the effects of Fe and Co substitutions in magnetic shape memory system Mn_2NiGa using first-principles density functional theory based calculations. We study the site preferences of the substituents, the stabilities of the substituted compounds, and their various properties in order to understand different aspects of substitutions in Mn_2NiGa, which in combination with available results on the Ni_2MnGa systems with similar substitutions can provide a consistent picture of the effects of such substitution in Ni-Mn-Ga alloys. We perform investigations mostly in the Hg_2CuTi structure which represents the high-temperature austenite phase of Mn_2NiGa. Regarding site preferences and stability of the compounds formed by substitutions at different sites, we find that the substituents prefer the sites of substituting atoms when Ni or Mn is being substituted. In the case of substitution of Ga, the substituents prefer to occupy the 4a sites in the Hg_2CuTi lattice, displacing the original constituent to the 4d site. This is in contrast with substituted Ni_2MnGa where site preferences sensitively depend upon the substituting site and the substituent. We also find that the Co substitution in Mn_2NiGa makes the system more stable in comparison to Fe-substituted Mn_2NiGa.

The patterns in the site occupancies lead to a gradual stabilization of the austenite phase of Mn_2NiGa irrespective of the site of substitution and the substituent, in agreement with experimental observations. [239, 240] This uniform trend is an artifact of progressive weakening of the Jahn-Teller distortion that drives martensitic transformation in Mn_2NiGa. The Jahn-Teller instability in the Hg_2CuTi phase of Mn_2NiGa is due to the hybridizations between the d states of constituents at the 4a and 4b positions(MnI and Ni, respectively) and the p states of Ga in the minority band. Since the substitution of another transition-metal element such as

Fe or Co in Mn_2NiGa invariably replaces the elements at the 4a and 4b positions, the hybridizations leading to the Jahn-Teller instability, gradually vanish with the increase in concentration of the substituent. The deep-lying states of Fe and Co cannot restore the Jahn-Teller instability, but rather contribute to its decline. The fact that the strengthening (weakening) of the Jahn-Teller distortion upon substitution can explain the gradual stabilization of the martensite (austenite) phase is also seen in the case of substituted Ni_2MnGa. [106, 245] However, the differences in the electronic structures in the two substituted systems, stemming from the differences in the stacking sequence of the atoms in their respective austenite phases, lead to different trends in the stabilizations of the austenite phases as a function of substituent concentration. Thus, the site preferences of the substituents along with the positions of their states inside the minority spin bands can help understand the trends in the phase stability of Ni-Mn-Ga alloys over a large composition range.

The results on elastic moduli provide two useful pieces of information: (i) the tetragonal shear modulus C' can be considered as a predictor of the martensitic transformation and (ii) a correspondence between the ductile-to-brittle and metallic-to-covalent bonding transition can be curved out for substituted Mn_2NiGa. We find that the weakening of the Jahn-Teller instability largely correlates with the strengthening of the covalent bonds, due to hybridizations of the minority spin states of the substituents with either of the elements in 4a and 4b positions along with Ga at the 4d sites. The substitution at Ni sites renders the systems more covalent as well as more brittle, while the rest of the systems are, by and large, more metallic and ductile.

An immediate consequence of the disappearance of the Jahn-Teller distortion and the positions of the energy levels of the substituents which are deeper into the occupied parts of the minority spin bands of Mn_2NiGa, is the opening of an energy gap in the minority band cutting through the Fermi level. This gap is like a half-metallic gap with spin polarizations of the substituted Mn_2NiGa reaching near 100% when the substitution is complete. We find that all the compounds formed by 100% substitution have nearly integer magnetic moment and nearly follow the Slater-Pauling rule of $M = N_v - 24$, [258, 259], with M the total magnetic moment and N_v the number of valence electrons. Thus Fe and Co substitutions, although leaving Mn_2NiGa unsuitable for shape-memory applications except at low concentrations of the substituents, produce compounds which are potentially useful for other magnetic applications. This is in contrast to the substituted Ni_2MnGa, where Fe and Co substitutions at Mn and Ni sites lead to compounds Ni_2CoGa,

Ni_2FeGa, NiCoMnGa and NiFeMnGa; the first two are shape-memory materials and the last two are normal metals.

The magnetic properties of Mn_2NiGa, in general improve, with more presence of the substituents. This is because of increasing ferromagnetic exchange interactions between the substituents and other magnetic atoms, and subsequent weakening of the dominant MnI-MnII antiferromagnetic interaction. The magnetic moments increase with concentration of the substituents as a result of this, the highest rise being in the case of substitutions at the Ga sites, where an uncommon pattern of site occupancy magnifies ferromagnetic exchange interactions. Thus, we find a stable magnetic material Mn_2NiCo with a moment as high as $\sim 9\mu_B/f.u.$ The magnification of ferromagnetic exchange interactions elevates the Curie temperatures in these systems with T_c of Mn_2NiCo as high as $\sim$ 900 K. This material is in the league of newly discovered magnets in the Heusler family having only $3d$ transition metals as their components [260]. The presence of competing antiferromagnetic and ferromagnetic exchange interactions in all the compounds studied here gives rise to nonmonotonic variations in T_c, in stark contrast to substituted Ni_2MnGa compounds where T_c varies rather monotonically with the concentration of the substituents. [232, 261] Such monotonic variations in substituted Ni_2MnGa are due to the fact that unlike substituted Mn_2NiGa, the dominant exchange interactions are ferromagnetic, and thus the T_c is controlled by the variations in particular ferromagnetic interactions with concentration of the substituents.

In conclusion, this work has explored the interrelations between the site occupancy, martensitic phase stability, bonding picture, and mechanical and magnetic properties of Fe and Co substituted Mn_2NiGa. The results demonstrate that the same analytical approach can be used for substituted Ni_2MnGa and Mn_2NiGa and thus the effects of substitution of another transition metal in the Ni-Mn-Ga system over a wide range of composition can be easily predicted. However, knowledge of the physical mechanisms in substituted Ni_2MnGa can not be rigidly applied to predict the trends in properties of substituted Mn_2NiGa compounds as there are significant differences between the two pristine compounds starting with their crystal structures. This work is a comprehensive investigation of the similarities and differences between the impacts of substitutions in these two systems and analysis of them from a microscopic point of view. An important and somewhat unexpected outcome of this work is the emergence of highly spin-polarizable, nearly half-metallic compounds with high Curie temperatures upon complete substitution. The material Mn_2NiCo shows promise with its very high moment, spin polarization and T_c. These results can motivate experimentalists to explore such materials. This work also acts as a guide to researchers on the choice of suitable substituent and composition to improve functional properties of Ni-Mn-Ga systems.

Chapter 5

Structural phase stability and magnetic order in various structural phases of Mn_2FeGa

5.1 Introduction

In the earlier chapter, we have shown that complete substitution of Fe at the Ni site in Mn_2NiGa leads to a new compound Mn_2FeGa as a member of the series Mn_2YZ. At low temperature, Mn_2FeGa crystallize in a tetragonal structure. A tetragonal structure is required for obtaining a high perpendicular magnetocrystalline anisotropy(PMA), a key requirement for spin-transfer torque(STT) and permanent magnet applications [50]. Among various Mn_2YZ compounds, the Mn_3Ga is a well studied system which is found to crystallise in different structures; a cubic Cu_3Au-like [59], a hexagonal DO_{19} [60] and a tetragonal DO_{22} phase [70, 71], resulting in a high perpendicular magnetocrystalline anisotropy in the DO_{22} phase and a large Exchange Bias in the DO_{19} phase, which are useful for STT-MRAM [70] and magnetic tunnel junction [60] applications, respectively. First-principles Density Functional Theory (DFT) calculations predicted another Heusler-like metastable structure in Mn_3Ga with a half-metallic gap, which transforms to the DO_{22} structure [85, 86]. This phase, however, has not yet been synthesised experimentally. Comprehensive DFT calculations inferred that the phase transition from DO_{19} to DO_{22}, as observed in the experiments [59], happens via the Heusler-like phase [108]. First-principles computations of the magnetic exchange interactions [262] and the magnetic anisotropy [70] concluded that the novel magnetic properties of Mn_3Ga in

---

The contents of this chapter are published in Intermetallics **93**, 209-216 (2018)

DO_{19} and DO_{22} structures are due to non-collinear magnetic structures arising out of frustrations due to geometry as well as competing exchange interactions between in-plane and out-of-plane Mn atoms.

Inspite of enough promises towards a variety of magnetism related applications, Mn_3Ga has low saturation magnetisations originating from the predominantly antiferromagnetic interactions between the Mn atoms. The low saturation magnetisation in Mn_3Ga limits its applicability in potential permanent magnet applications, inspite of having strong uniaxial magnetic anisotropy and large Curie temperature. Attempts have, therefore, been made to combat the dominant antiferromagnetic interactions in these systems by replacing one of the Mn with ferromagnetic elements like Co and Fe. Complete replacement of one Mn atom by Fe, resulting in the compound Mn_2FeGa, was expected to circumvent the problems. Synthesis of Mn_2FeGa, however, exhibited several important aspects of structure-property relationship. Various crystallographic phases with possible magnetic structures were observed and predicted experimentally. Gasi *et al.* [61] reported an inverse tetragonal Heusler structure with a low saturation magnetic moment and a high Curie temperature for samples annealed at 400^0C. The system behaved like an exchange spring which was attributed to the distribution of Fe atoms among the Mn sites resulting in two different magnetic states of Fe. A Cu_3Au-like structure was observed when the system was annealed at 800^0C. A giant tuneable Exchange Bias was later obtained in the inverse tetragonal structure with a saturation magnetisation as low as 0.09 μ_B/f.u. [72] suggesting a near compensation of moments from Mn and Fe atoms. DFT calculations, like Mn_3Ga, predicted a meta-stable inverse Heusler phase for Mn_2FeGa, which transforms to the inverse tetragonal structure observed in the experiments [85, 86]. The electronic structure of inverse Heusler Mn_2FeGa revealed a pronounced instability associated with the minority spin band [86]. However, unlike Mn_2NiGa, the transformation from inverse Heusler to inverse tetragonal phase didn't turn out to be volume conserving, implying the possibility of absence of shape memory effect in this system. Investigations into sputter deposited thin films of Mn_2FeGa [263] find that the system crystallises either in inverse tetragonal or in the Cu_3Au-like cubic phase. Mossbauer spectroscopy on epitaxial thin films suggested that Fe might be statistically distributed among the two Mn sites leading to a low spin moment in the inverse tetragonal phase [264]. Heteroepitaxially grown thin films of Mn-Fe-Ga with composition near that of Mn_2FeGa also exhibited strong perpendicular anisotropy and moderate coercivity suggesting that this system can be used in mid-range permanent magnet applications [265]. Like Mn_3Ga, this system could also be synthesised in DO_{19}-type hexagonal structure which yielded a giant Exchange Bias field upto 1.32 kOe [62]. The large Exchange Bias was attributed to the presence of substantial ferromagnetic matrix due to Fe-Mn pairs in an antiferromagnetic host.

The experimental observations clearly indicate that investigations into the phase stability, sub-lattice occupancy and magnetic properties of Mn_2FeGa would be insightful. The following issues, in particular, are worth looking into, in order to understand the physics associated with Fe substitution in either Mn_3Ga or in Mn_2NiGa, the two compounds having very different functional aspects: (i) the energetics of various phases observed experimentally or are predicted theoretically but not observed experimentally, (ii) the magnetic interactions among three different magnetic atoms and their dependencies on the sub-lattice occupancies of the atoms in different structural phases. This can be particularly relevant in the hexagonal phase where the Fe atom has more than one choice of the crystallographic site it can occupy, and (iii) the effect of anti-site disorder on the magnetic properties. In this chapter, we have undertaken a DFT based comprehensive investigation into the structural and magnetic properties of the four crystallographic phases of Mn_2FeGa, the Cu_3Au-like, the hexagonal DO_{19}-like, the inverse Heusler and the inverse tetragonal. Emphasis has been given on identifying the magnetic structure in the hexagonal phase as it is supposed to be most complex in this phase as was observed in Mn_3Ga. We have computed the magnetic exchange interactions in each structural phase in order to understand the magnetic structures. The electronic structures of the structural phases are computed and analysed in order to provide a possible picture of the phase transformations. The elastic constants and the phonon dispersion relations for select phases are computed to supplement the analysis from the energetics and the electronic structures. In this work, we have not incorporated anti-site disorder in order to avoid dealing with prohibitively large number of possible configurations, in particular for the hexagonal structure. In absence of concrete quantitative estimate of the anti-site disorder from the experiments, this is justified.

5.2 Calculational details

All calculations were performed with spin-polarised density functional theory (DFT) based projector augmented wave(PAW) method [120] as implemented in Vienna Ab-initio Simulation Package (VASP) [177, 178]. Perdew-Burke-Ernzerhof (PBE96) implementation of Generalised Gradient Approximation (GGA) for exchange and correlation [179] part in the Hamiltonian was used throughout. An energy cut-off of 500 eV and a Monkhorst-Pack [180] $25 \times 25 \times 25$ k-mesh for Cu_3Au-like and inverse Heusler structures , a $15 \times 15 \times 13$ k-mesh for the tetragonal structure and a $13 \times 13 \times 11$ k-mesh for the hexagonal structure were used for self consistent calculations. Larger k-meshes were used for the densities of states calculations of all the structures. The k-meshes used were $29 \times 29 \times 29$ for Cu_3Au-like and inverse Heusler, $19 \times 19 \times 17$ for tetragonal and $15 \times 15 \times 13$ for hexagonal structures. For all calculations, the total energy convergence criteria and the force convergence criteria were set to 10^{-6} eV and to 10^{-2} eV/Å respectively. The elastic constants were calculated from the second derivatives of the total energies with respect to the strain tensors [130].

The magnetic pair exchange parameters were calculated with multiple scattering Green function formalism as implemented in SPRKKR code [141] and as discussed in chapter 2. In order to calculate the total energy, full potential spin polarised scalar relativistic Hamiltonian with angular momentum cut-off $l_{max} = 3$ is used along with a converged k-mesh for Brillouin zone integration. The Green's functions are calculated for 32 complex energy points distributed on a semi-circular contour. The energy convergence criterion is set to 10^{-5} eV for the self-consistency. The equilibrium lattice parameters and optimised atomic positions as obtained from the PAW calculations are used to obtain the self-consistent potentials in the multiple scattering Green's function method.

5.3 Results and Discussions

5.3.1 Structural parameters and magnetic structures in various crystallographic phases

Experimentally, Mn_2FeGa has been observed to crystallise in three different phases, the Cu_3Au-like, the tetragonal DO_{22} like and the hexagonal DO_{19} [61, 62], depending on the annealing temperature. DFT calculations predicted a inverse Heusler phase [85, 86, 253], yet undetected in experiments. In these investigations, the possible site-specific magnetic structures associated with different structural phases have been indicated through indirect evidences. In this subsection, we present results on the structural properties and possible ground state magnetic structures, along with atomic moments for all four structural phases of Mn_2FeGa. Throughout the manuscript, the Cu_3Au-like phase, the hexagonal phase, the inverse Heusler

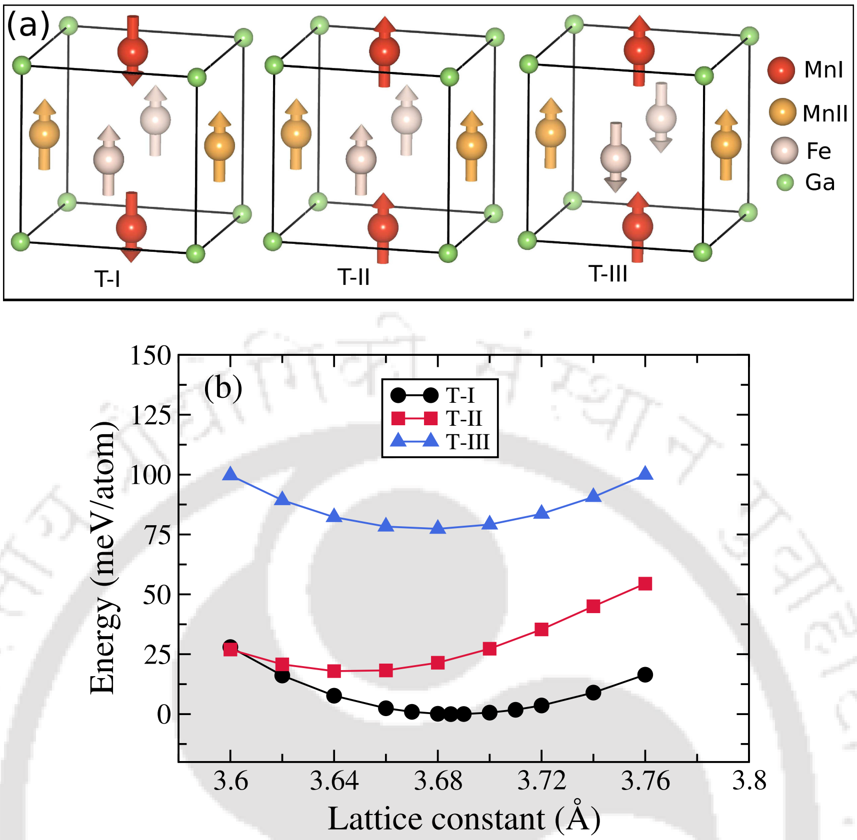

Figure 5.1: (a) Possible magnetic configurations in Cu_3Au phase of Mn_2FeGa. (b) Total energy as a function of lattice constant for different magnetic configurations in Cu_3Au phase of Mn_2FeGa.

phase and the inverse tetragonal phase are referred to as the Cu_3Au, the DO_{19}, the X_a and the $L1_0$ phases respectively. The results are summarised in Table 5.1.

Cu_3Au phase: In the ordered Cu_3Au structure of Mn_2FeGa, the Ga atom occupies the corners of the cubic unit cell while the two Mn, MnI and MnII, along with the Fe, occupy the face centres (Fig. 5.1(a)). Depending upon the relative orientations of the moments of the three magnetic atoms, three inequivalent collinear spin configurations are possible in this structure as shown in Fig. 5.1(a). Our total

Table 5.1: The calculated lattice parameters(in Å), total(M) and atomic magnetic moments(M_X)(in μ_B per formula unit) of Mn_2FeGa in Cu_3Au, X_a, $L1_0$ and DO_{19} phases. The results from experiments and other DFT calculations are given in parenthesis

Structure	Lattice parameter a	Lattice parameter c	M	M_{MnI}	M_{MnII}	M_{Fe}	M_{Ga}
Cu_3Au	3.69(3.7526 [61])	3.69	0.68	-3.08	2.55	1.28	-0.03
X_a	5.78(5.80 [253],5.79 [85])	5.78	1.04(1.03 [85])	-2.07	2.80	0.29	0.01
$L1_0$	3.68(3.7915 [61],3.68 [86])	7.29(7.1858 [61],7.29 [86])	-0.80(0.96 [50],-0.78 [86])	-2.43	2.96	-1.41	0.04
DO_{19}	5.25(5.3151 [62])	4.20(4.3050 [62])	1.22(1.26 [62])	-2.84	2.54	1.55	-0.03

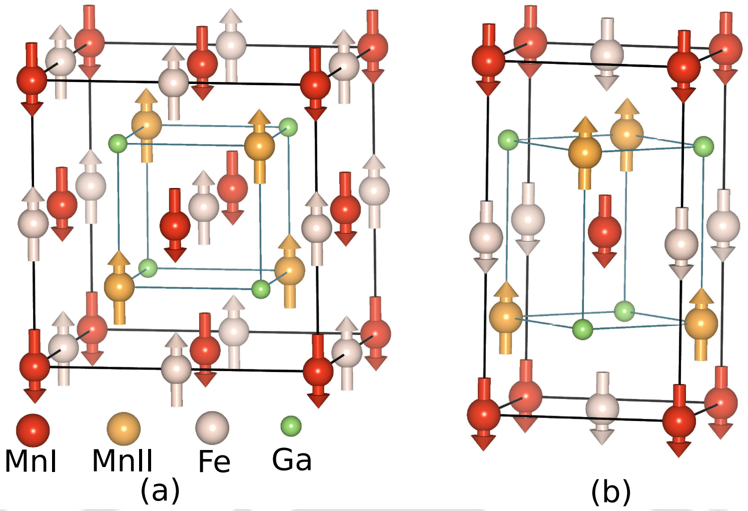

Figure 5.2: (a) The X_a structure and (b) the $L1_0$ structure of Mn_2FeGa. The spin configurations shown are the ground state configurations obtained from our calculations.

energy calculations show that the energetically lowest configuration is T-I where the two Mn atoms orient anti-parallel (Fig. 5.1(b)). The calculated lattice parameter agrees well with experimental reported one (Table I). The total magnetic moment is only 0.68 $\mu_B/f.u.$, with MnI having a larger moment among the two Mn atoms. The Fe moment is only 1.28 μ_B, much less than that in its elemental solid phase. Mossbauer spectra of Mn_2FeGa, annealed at 800°C [61], confirmed the Cu_3Au-like structure but the measurements of hyperfine field distributions suggested that the average moment at the Fe site is only $0.5\mu_B$ as Fe may occupy Mn sites as well. Since we have not included the anti-site disorder, that is mixing of Fe and Mn atoms at all crystallographic sites, the discrepancy with the experimental results is natural. Since the experimental measurements did not indicate any possibility of non-collinearity in the magnetic structure, our consideration of the collinear magnetic structure is justified, and thus, our results provide the possible ground state magnetic configuration if Mn_2FeGa crystallises in a perfectly ordered Cu_3Au phase. A comparison with Mn_3Ga in the ordered Cu_3Au phase [59] shows that replacing one Mn atom by Fe has led to a reduction of the total moment of the system. In Mn_3Ga, the MnI and MnII moments were -2.93 μ_B and 2.24 μ_B respectively, leading to a total moment of 1.55 μ_B per formula unit. The atomic moments in Mn_2FeGa, as obtained here, suggest that the Mn moments have not changed significantly, but the reduction in the total moment, in comparison to Mn_3Ga, happens due to weaker exchange splitting associated with the Fe atoms.

X_a phase: DFT calculations predict a Hg_2CuTi or inverse Heusler structure for Mn_2FeGa [85, 253]. In this structure, also known as X_a structure, the MnI and MnII atoms occupy 4a and 4c Wyckoff positions respectively. The 4b and 4d Wyckoff positions are occupied by Fe and Ga atoms respectively. The X_a structure of Mn_2FeGa is shown in Fig. 5.2(a). The equilibrium lattice constant (Table 5.1) obtained in this work is consistent with the reported results [85, 253]. The calculated magnetic moment is close to 1.0 $\mu_B/f.u$, in very good agreement with the existing DFT results. The atomic moments (Table 5.1) show that the Fe moment is quenched substantially, and that the low total moment arises due to anti-parallel alignment of the two Mn atoms. The ground state magnetic configuration in this structure is consistent with that of Mn_2NiGa [77], in which Fe substitution at the Ni site gives rise to the present compound under investigation. Interestingly, the total and the atomic moments of Mn_2FeGa in this structural phase are very similar to Mn_2NiGa. In contrast, there is substantial differences between the total and the atomic moments of Mn_2FeGa and Mn_3Ga in this phase. In Mn_3Ga, the total moment is nearly zero in this phase [85]. This is due to the fact that unlike Mn_2FeGa, Mn_3Ga has a Heusler like coordination (space group 225) and thus the Mn moments at 4a and 4b sites compensate the moment at 4c sites associated with the other Mn aligning anti-parallel. The alteration in the coordination in Mn_2FeGa, thus, introduces magnetic interactions, very different from those in Mn_3Ga.

$L1_0$ phase: The tetragonal L_{10} phase of Mn_2FeGa (Fig. 5.2(b)) has been synthesised [61, 264] and been the subject of intense investigations due to the possible PMA and high coercivity in this structure. Investigations into the magnetic structure concluded that the system has a ferrimagnetic order, and unlike Mn_3Ga [70], the spins are collinear. The magnetisation measurement on polycrystalline samples at 10 T field yielded a non-saturating magnetisation of about 1.5 μ_B [61]. Using results from magnetometry, Betto *et. al.* [264] estimated the atomic magnetic moments and the spin structure (Fig. 5.2(b)). Their estimation of atomic moments, based upon magneto-optical sum rules resulted in equal moments on MnI and Fe sites with MnII sites having a 30% less moment. Incorporation of Fe anti-sites in their calculations increased the moment at MnII sites resulting in nearly equal moments at all three sites, which would result in a very small net moment in the system. This was in contrast to Mn_3Ga, where the estimated moments associated with the MnI and MnII were 2.67 μ_B and 4.74 μ_B respectively, producing a net moment of about 0.6 μ_B per formula unit [70]. DFT calculations by Wollmann *et al.* [86], on the other hand, obtained unequal magnetic moments at MnI and MnII sites, along with a moment at the Fe site which is nearly 50% of the moment which is larger among the two Mn moments, producing a net moment of about 0.8 μ_B per formula unit. Our results in Table 5.1 are in excellent agreement with those of Wollmann *et al.* Particularly interesting is the gain in Fe moment in comparison to the X_a phase, and the change in its orientation with respect to the Mn sub-lattices. Such behaviour of the atomic moments, in particular of Fe in Mn_2FeGa, is in stark contrast to that of Ni in Mn_2NiGa. In prototype shape memory alloys like Ni_2MnGa and in Mn_2NiGa, the systems undergo martensitic transformations from $L2_1$ Heusler and X_a structures, respectively to $L1_0$ structures, conserving their volumes with little changes in their atomic and total magnetic moments. The very different behaviour of the atomic magnetic moments in X_a and $L1_0$ phases of Mn_2FeGa indicate that the physics associated with the system in these phases would be different from those of shape memory Ni_2MnGa and Mn_2NiGa.

In order to elucidate this point, we have optimised the structural parameters in the $L1_0$ phase of Mn_2FeGa by computing the total energy as a function of the tetragonal deformation, represented by the c/a ratio, keeping the volume fixed at that of the X_a phase. The results are presented in Fig. 5.3. The energetics of Ni_2MnGa and Mn_2NiGa are presented for comparison. We find a local energy minima at $c/a = 1.0$ and a global energy minima at $c/a = 1.40$. For Mn_2FeGa, the energy surface looks very different compared to those of Mn_2NiGa and Ni_2MnGa. We further computed the total energies for the $L1_0$ structure by varying the volume. The results are shown in the inset of Fig. 5.3. We clearly see that the optimised volume of the $L1_0$ phase is higher by 2.54% than the volume of X_a structure which indicates that the X_a to $L1_0$ transformation in this system is not a volume conserving one and the system would not exhibit shape-memory effect. The optimised structural parameters, presented in Table 5.1 are in good agreement with the results obtained from experiments and previous DFT calculations.

DO_{19} phase: The hexagonal DO_{19} phase of Mn_2FeGa has been synthesised only recently [62] after annealing the polycrystalline sample to 600^0C. In the hexagonal (DO_{19}) structure(space group no. 194; $P6_3/mmm$) there are two formula units of atoms (8 atoms) arranged in two different planes of the unit cell. (T1, T2, T3, T4) and (B1, B2, B3, B4) are the lattice sites in top and bottom planes respectively, as shown in Fig. 5.4(a). The atomic positions at top plane are: T1(1/6, 1/3, 3/4), T2(2/3, 5/6, 3/4), T3(1/6, 5/6, 3/4), T4(2/3, 1/3, 3/4), and at bottom plane are: B1(1/3, 1/6, 1/4), B2(5/6, 2/3, 1/4), B3(5/6, 1/6, 1/4), B4(1/3, 2/3, 1/4). In hexagonal Mn_3Ga, the Ga atoms occupy T4 and B4 sites in two different

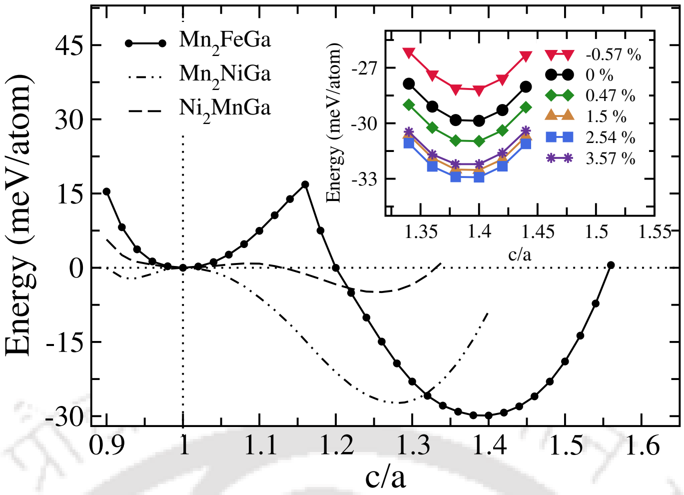

Figure 5.3: Total energy as a function of tetragonality(c/a) for Mn$_2$FeGa in the L1$_0$ phase. The total energy curves of Ni$_2$MnGa and Mn$_2$NiGa are presented for comparison. The zero energy is taken to be the energy corresponding to the X$_a$ phase(c/a=1). Total energy of Mn$_2$FeGa as a function of c/a for different volumes in L1$_0$ phase are shown in inset. Each curve in the inset represents the percentage change in volume with respect to the equilibrium volume in the X$_a$ phase.

layers of the unit cell. The Mn atoms occupy other six positions in the unit cell. Such a geometry inherently produces a frustrated magnetic structure in Mn$_3$Ga. Accordingly, different non-collinear spin configurations were investigated to obtain the ground state magnetic configuration in the system by DFT calculations [108]. The configuration with the lowest energy was found to be a triangular structure with a 120^0 mutual orientations of the neighbouring Mn atoms in the same plane as well as of the neighbours in the adjacent planes. This was in confirmation with the results of Neutron diffraction [107]. Subsequently, the magnetic moment came out to be nearly zero with the moment at Mn site to be $\sim 2.5\ \mu_B$ [107, 108]. The magnetisation measurements on DO$_{19}$ Mn$_2$FeGa obtained a saturation moment of 1.26 μ_B per formula unit [62]. The authors proposed that this is an effect of increasing Fe-Mn local ferromagnetic matrix in otherwise antiferromagnetic host as Fe can occupy Mn sites either in a single layer or across the layers of the hexagonal planes. If hexagonal Mn$_2$FeGa is considered to be formed out of hexagonal Mn$_3$Ga by replacing one Mn atom with Fe, in the DO$_{19}$ unit cell, two Mn atoms out of six are to be replaced by Fe atoms. Since these Fe atoms can occupy any two positions out of the six inequivalent sites among the two planes (keeping the position of Ga atoms fixed), many inequivalent combinations of site occupancy are possible in this phase. Consideration of symmetry, however, reduces the possible number of configurations to only seven which are given in Table 5.2. Due to the geometrical frustration arising

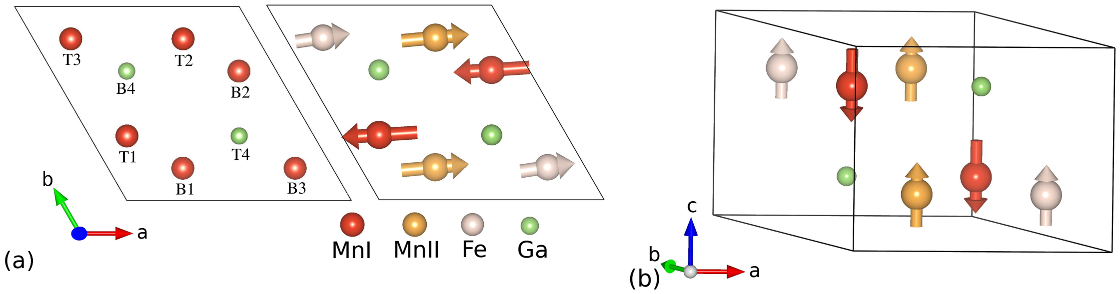

Figure 5.4: (a) Left: Hexagonal(DO_{19}) structure of Mn_3Ga. The atomic sites marked T and B correspond to sites in the top and the bottom planes respectively. (a) Right: The DFT calculated magnetic structure of Mn_2FeGa. (b) The magnetic structure of Mn_2FeGa in DO_{19} phase modelled after the actual one shown in (a), with the magnetisation axis along z-direction.

out of triangular networks in the DO_{19} structure, consideration of non-collinear spin structures as the starting point of the calculations are necessary. In absence of any experimental information regarding the spin structure of this system in DO_{19} phase, we started our calculations with the reported spin configuration of Mn_3Ga in the literature [108]. We optimised the magnetic structures and calculated the formation enthalpies of all seven configurations. The calculated formation enthalpy and the corresponding magnetic moments are presented in Table 5.2. The results suggest that the configuration with configuration number 4 in Table 5.2 has the lowest formation enthalpy. The corresponding magnetic structure is shown in Fig. 5.4(a). The calculated total magnetic moment for this configuration is 1.30 $\mu_B/f.u.$ which agrees very well with the experimental magnetisation value of 1.26 $\mu_B/f.u.$ [62]. The optimised magnetic structure corresponding to other configurations are shown in Fig. 5.5. The calculated total magnetic moment for these configurations are deviating from the experimental measured value except for the configuration-3. Though, these configurations are energetically higher, but possible to form as is obvious from the negative values of the formation enthalpies (Table 5.2).

Contrary to the expectations, our calculations show the minimum energy configuration of the spins to be one where they are confined to the planes and pointing either along the a-direction or against it, a collinear arrangement when observed in the $a - b$ plane. Since the magnetic arrangement is like a collinear one, we calculated the total energy of this configuration by aligning the spins along the z-direction. The corresponding magnetic structure is shown in Fig. 5.4(b). The differences in energies of the two configurations turned out to be less than 1 meV per formula unit. The magnetic moment of the configuration with spins directed

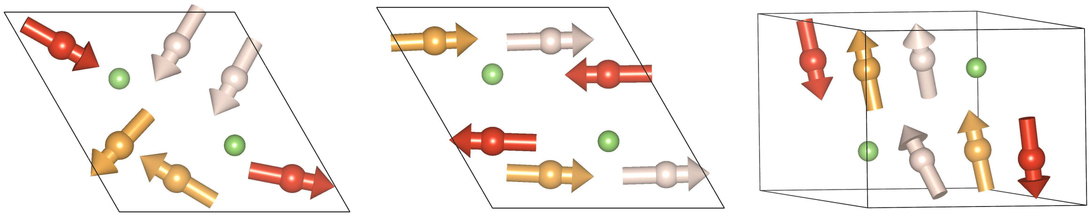

(a) Configuration-1 (b) Configuration-2 (c) Configuration-3

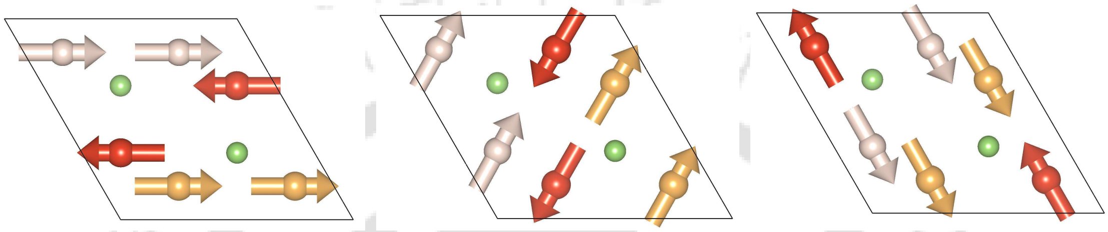

(d) Configuration-5 (e) Configuration-6 (f) Configuration-7

Figure 5.5: The optimized magnetic structures for the configurations given in Table 5.2. The color code corresponding to each atom are shown in Fig. 5.4.

either along or against z-direction is 1.22 μ_B per formula unit (Table 5.1), very close to that obtained for the minimum energy configuration with spins in the $a - b$ plane (Table 5.2). This justifies using the collinear configuration with z-axis the easy axis for further calculations. The lattice parameters obtained by optimising these configurations, presented in Table 5.1, agree quite well with the experiments. Thus, the presence of Fe in the system appears to have taken care of the frustration in the system and produces a collinear kind of magnetic structure which explains the significant non-zero magnetisation of Mn_2FeGa in this phase.

5.3.2 Stabilities of various phases: analysis from energetics, electronic structure and elastic constants

Figure 5.6 shows the variations in the total energies with volume for the four phases of Mn_2FeGa. We relaxed all the structural parameters to obtain the most stable structure in a given phase. The tetragonal phase comes out to be energetically the most stable phase while the Cu_3Au phase is having the highest total energy. The hexagonal, and the X_a phases lie in between with the X_a phase having a total energy in between the hexagonal and the tetragonal phase. The relative energies of these phases obtained this way agrees with the experiments in a way as the tetragonal phase is observed to be the low temperature phase [61] while annealing to a high

Table 5.2: The possible configurations due to different site occupancy patterns in DO_{19} phase of Mn_2FeGa. E_f(eV/f.u.) is the formation enthalpy for a given configuration. $M_{tot}(\mu_B/f.u.)$ is the calculated total magnetic moment in a given configuration.

	Sites and occupancies									
No.	T1	T2	T3	T4	B1	B2	B3	B4	E_f	M_{tot}
1	Mn	Fe	Mn	Ga	Mn	Fe	Mn	Ga	-0.460	3.03
2	Mn	Fe	Mn	Ga	Mn	Mn	Fe	Ga	-0.459	1.63
3	Mn	Fe	Mn	Ga	Fe	Mn	Mn	Ga	-0.504	1.28
4	Mn	Mn	Fe	Ga	Mn	Mn	Fe	Ga	-0.509	1.30
5	Mn	Fe	Fe	Ga	Mn	Mn	Mn	Ga	-0.456	1.46
6	Fe	Mn	Fe	Ga	Mn	Mn	Mn	Ga	-0.456	1.46
7	Fe	Fe	Mn	Ga	Mn	Mn	Mn	Ga	-0.456	1.45

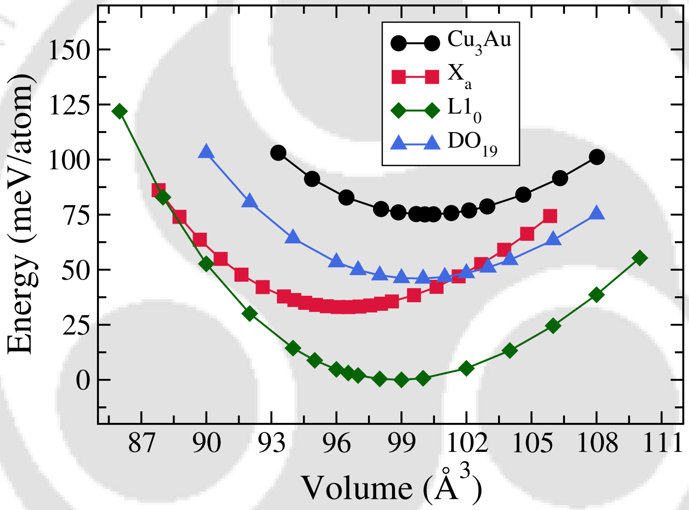

Figure 5.6: Total energy as a function of unit cell volume for different structural phases of Mn_2FeGa.

temperature stabilises the Cu_3Au phase; the hexagonal phase being obtained only when the sample is annealed at temperatures in between the annealing temperatures to obtain the $L1_0$ and the Cu_3Au phases. The other interesting feature of the relative energetics is that the DO_{19} and the X_a phases are energetically very close near the equilibrium volume of the DO_{19} phase. Since there is no possibility of a direct DO_{19} to $L1_0$ transformation due to symmetry constraints [108], and that a transformation between the X_a and DO_{19} is possible, as illustrated in case of Mn_3Ga [108], our results imply that the phase transformation from DO_{19} to $L1_0$ can take place via the X_a phase. Thus, although the X_a phase has not yet been obtained experimentally, possibly due to requirement of growth by non-equilibrium methods as it appears to be metastable (Fig. 5.3), its presence is very important to understand the stabilities

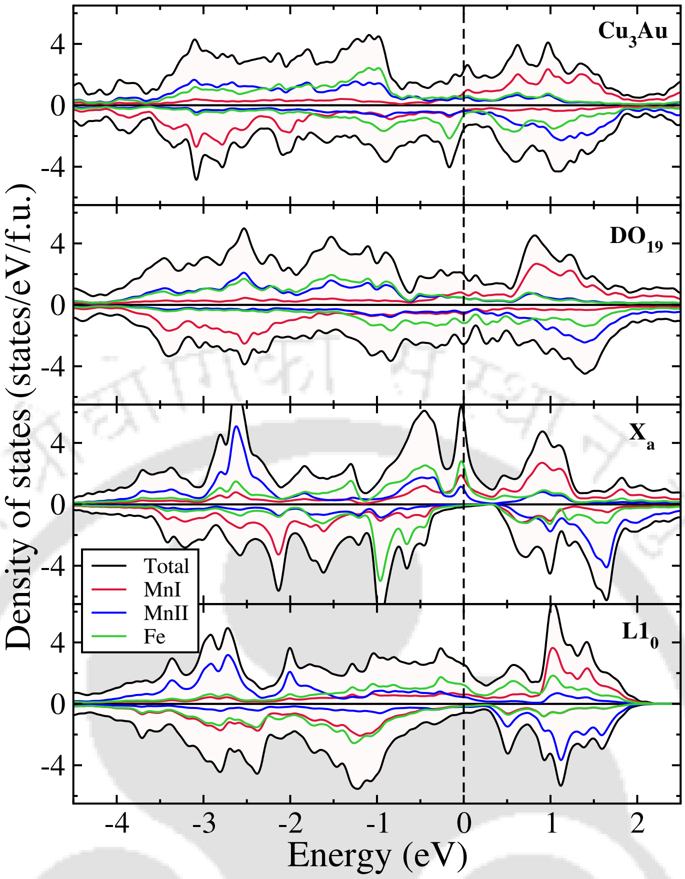

Figure 5.7: Spin polarised total and atom-projected densities of states of Mn_2FeGa in various structural phases.

of the DO_{19} and the $L1_0$ phases and the possible path of transformation between the two phases. The DFT total energies obtained at T=0 K can only provide a qualitative understanding of various phases. In order for a quantitative idea regarding phase transitions, particularly for phases obtained by annealing the sample to a high temperature, one needs to compute the free energy incorporating the effects of vibrational, magnetic and configurational entropies. Such computationally intensive study is beyond the scope of the present work. The importance of the results contained in Fig. 5.6, thus, lies in providing us with the energetic hierarchies of the various phases coming solely from the electronic effect.

In order to gain further insight into the stabilities of these phases in Mn_2FeGa, we take a look at their electronic structures. In Fig. 5.7, we show the total and atom-projected densities of states of Mn_2FeGa in various structural phases. These also help us understanding the behaviour of atomic magnetic moments in each phase. Across all the structures, we find that the minority(majority) band of MnI is nearly full(nearly empty) while the opposite is true for MnII bands. This explains the anti-parallel orientation of the moments associated with the two Mn atoms. For Cu_3Au and DO_{19} phases, there is strong hybridisation and delocalisation of the MnII and Fe bands in the majority spin channel, while they are more localised in the X_a and $L1_0$ phases. In the minority spin channel, the hybridisations between MnI and Fe bands are minimal for Cu_3Au, DO_{19} and X_a phases while it is substantial in the $L1_0$ phase. In spite of less hybridisation, both MnI and Fe minority states in the Cu_3Au and DO_{19} phases are delocalised while they are more localised in the X_a phase. Thus, the densities of states in the X_a phase stand out in contrast to the other three phases; the highlights being more localised atomic densities of states and thus more structured total densities of states in comparison to relatively structureless total densities of states in other phases. The other major difference observed in the densities of states in the X_a phase is a sharp peak at the Fermi level in the majority band and a half-metallic gap in the minority band. The peak at the fermi level is due to hybridisation of MnI and Fe t_{2g} states while the gap in the minority band is flanked by the well separated t_{2g} and the e_g states of mainly Fe atom. The peak in the majority band densities of states implies instability in this structure which triggers the tetragonal distortion and subsequent stabilisation of the $L1_0$ phase. The t_{2g} states at the Fermi level in the X_a phase now splits into three non-degenerate states due to the lowering of the symmetry, thus washing away the peak. The symmetry lowering gets rid of the half-metallic gap too as the system stabilises by filling in the gap, that is by re-distributing the states into the lower energy states. The delocalisation and strong hybridisation of the MnI and Fe minority states in $L1_0$ structure is the outcome of this. The quenching of the Fe moment in the X_a structure can also be understood from the electronic structure. The nearly full Fe states in both spin channels reduces the exchange splitting associated with Fe. When the system tetragonally distorts towards the $L1_0$ structure, the Fe states fill out significant part of the occupied region in the minority band, while the spectral weight associated with the Fe states in the majority band shifts towards the unoccupied region, thus recovering the exchange splitting observed in the Cu_3Au and DO_{19} phases. The MnII states in the majority bands associated with the Cu_3Au and DO_{19} structures are distributed in a nearly identical way, providing an explanation to the almost equal MnII moments in these two phases. The proximity of the MnI moments in these two phases also emerge due to the nearly identical minority spin densities of states of MnI which implies nearly same exchange splitting associated with the MnI atoms. The Fe moments are also nearly equal in these phases which can be explained in a similar way as Fe hybridises with both Mn in relevant spin channels. The moments associated with

MnII in these two phases are less than that of MnI. The relatively less exchange splitting associated with the MnII atoms can be understood as the effect of stronger hybridisation with the Fe states. In the X_a and $L1_0$ states, the exchange splitting of MnII is more than that of MnI. This happens due to appearance of more localised MnII and Fe states in the majority spin band, thus reducing hybridisations.

The densities of states imply that Cu_3Au, DO_{19} and $L1_0$ phases are stable as was observed experimentally. The strong hybridisations between Mn and Fe states in either spin channels are found to be responsible behind it. The reduced hybridisations can be correlated with the instability in the X_a phase as implied by the large densities of states at the Fermi level. In order to understand the origin of this instability and to predict whether this phase can ever be synthesised, we first check the mechanical stability by computing the elastic constants. The elastic constants for all four phases are given in Table 5.3.

The calculated elastic constants satisfy all the stability criteria for Cu_3Au, X_a, DO_{19} and $L1_0$ phases [130, 266]. Among all, the shear modulus($C' = (C_{11} - C_{12})/2$) gives an insight to the stability of all the structures with respect to the shear(for hexagonal, $C_{66} = C'$). For all the structures, C' is positive and indicate the relative mechanical stability of the structure against shear. The C' value of tetragonal structure is higher than other structures which might indicate that it is the most stable structure against shear instability. For the X_a structure, however, the value of C' is sufficiently small, in comparison to C_{44}. The elastic anisotropy ratio $A\,(= C^{44}/C')$ is a measure of the stability of a crystal with cubic symmetry against stress along (110) planes [267]. In the X_a phase of Mn_2FeGa, this ratio is 8.66, indicating that the system can be unstable against anisotropic stress. In order to gain further insight into the possible consequences of it, and thus understand the mechanism of the X_a to $L1_0$ transformation in this system, we have computed the phonon dispersion relations in X_a phase, shown in Fig. 5.8. The dispersion relations indicate dynamical stability in the X_a phase. None of the acoustic modes in the X_a phase were imaginary, or

Table 5.3: The calculated elastic constants (in GPa) of Mn_2FeGa in Cu_3Au, X_a, $L1_0$ and DO_{19} phases.

Structure	B	C_{11}	C_{12}	C_{13}	C_{33}	C_{44}	C_{66}	C'
Cu_3Au	131.3	141.6	126.1	-	-	33.9	-	7.8
X_a	147.2	166.8	137.4	-	-	127.3	-	14.7
$L1_0$	140.2	292.2	0.56	124.2	179.5	100.2	11.6	145.8
DO_{19}	126.3	210.8	40.8	27.2	224.4	55.2	84.9	85

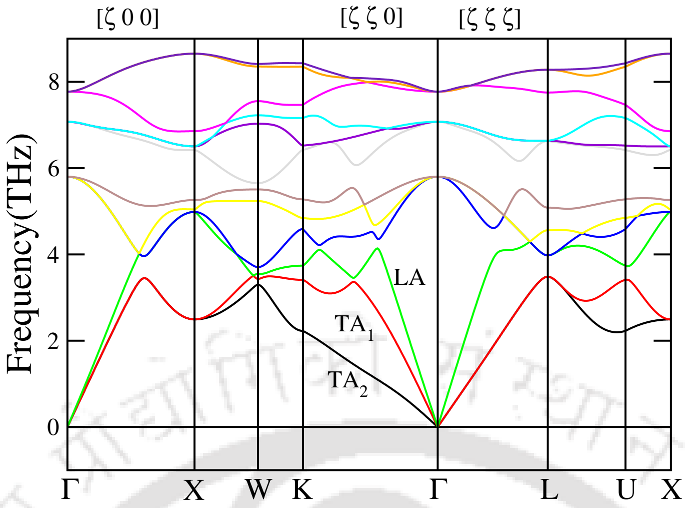

Figure 5.8: Phonon dispersion curves for the X_a structure of Mn_2FeGa along various high symmetry directions in the Brillouin zone.

produced any pronounced softening. These indicate that the transformation from X_a to $L1_0$ phase is not phonon driven as was the case for Mn_2NiGa in chapter 3. Thus, the phase transition from X_a to $L1_0$ can be considered due to the well known Jahn-Teller effect.

5.3.3 Magnetic exchange interactions

In order to understand the origin of the magnetic structures in various phases as depicted in subsection 5.3.1, we now look at the results of various inter-atomic and intra-atomic exchange interactions for the X_a, $L1_0$ and DO_{19} phases. Since the $L1_0$ and DO_{19} phases are the most promising ones from applications point of view and the X_a phase has strong connection with the $L1_0$ phase as has been established in the previous subsections, we have investigated the exchange interactions for these three phases. The results for the X_a and the $L1_0$ phases are presented in Fig. 5.9(a) and (b), respectively. For both phases, the nearest neighbour strong antiferromagnetic and ferromagnetic interactions between two different pairs of atoms dominate the scene. The higher neighbour interactions are too small to influence the magnetic structure, which would be collinear. In case of the tetragonal DO_{22} phase of Mn_3Ga, neutron diffraction experiments [70] found a small canting of Mn spins occupying the 2b sites (the sites occupied by Fe in Fig. 5.2 (b)). The calculated exchange parameters established frustration associated with that particular Mn site, which together with the in-plane magnetic anisotropy at that site, was used to explain the spin canting at that site. In the present case, we do not see any such possibility

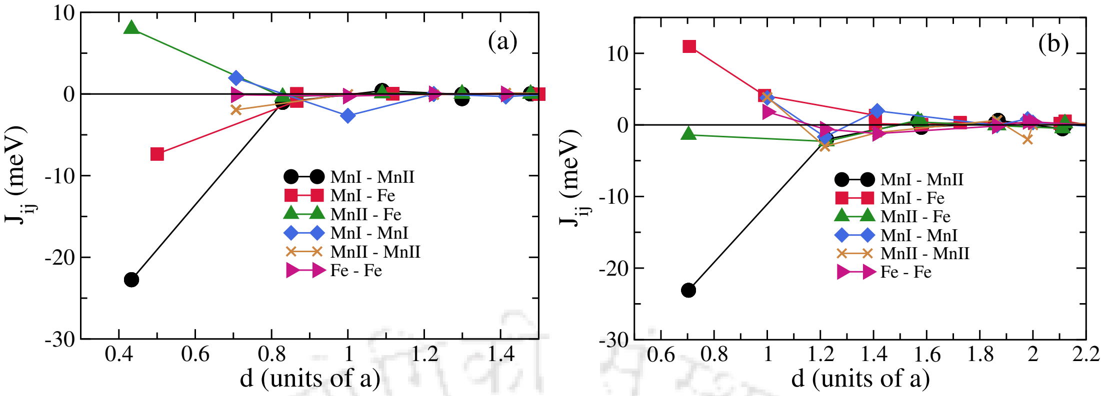

Figure 5.9: Magnetic exchange interaction(J_{ij}) of Mn_2FeGa as a function of interatomic distance(d) in (a) X_a and (b) $L1_0$ phases.

arising out of the qualitative and quantitative nature of the three major inter-atomic parameters associated with MnI-MnII, Fe-MnI and Fe-MnII pairs. For all three of them, at least the first two nearest neighbour exchange parameters are either ferromagnetic or antiferromagnetic, thus ruling out possibility of magnetic frustration. In Both X_a and $L1_0$ structures, the overwhelmingly dominating interaction is the antiferromagnetic MnI-MnII. Same was the case for DO_{22} Mn_3Ga. The qualitative difference between Mn_2FeGa and Mn_3Ga magnetic interactions is observed in cases of the exchange parameters involving Fe. In the X_a phase, the first neighbour antiferromagnetic Fe-MnI exchange parameter is of the same magnitude as that of the first neighbour ferromagnetic Fe-MnII one although the former pair is at a larger distance. In the $L1_0$ phase, we observe a role reversal of these two interactions: the Fe-MnI is now strongly ferromagnetic in the first neighbour, the interaction being ferromagnetic even for higher neighbours, while the Fe-MnII exchange is now weakly antiferromagnetic. This role reversal can be explained from the structural deformation of X_a that leads to the $L1_0$. The contraction in the basal plane now reduces the Fe-MnI distances along with a subsequent increase in the Fe-MnII distance due to elongation in the [001] direction. This increase in the Fe-MnII distances weaken the exchange interactions between this pair and makes it weakly antiferromagnetic, while the opposite happens for the Fe-MnI pairs which are now closer. The presence of strong ferromagnetic and antiferromagnetic components in the first neighbour exchange interactions of Mn_2FeGa in the X_a and $L1_0$ phases along with weak higher neighbour interactions are the reasons behind the collinear ferrimagnetic structure in these phases. Thus, the presence of Fe in the system inflicts a significant ferromagnetic component in the magnetic interactions, in comparison to Mn_3Ga.

The collinear-like magnetic configuration obtained in the DO_{19} phase of Mn_2FeGa,

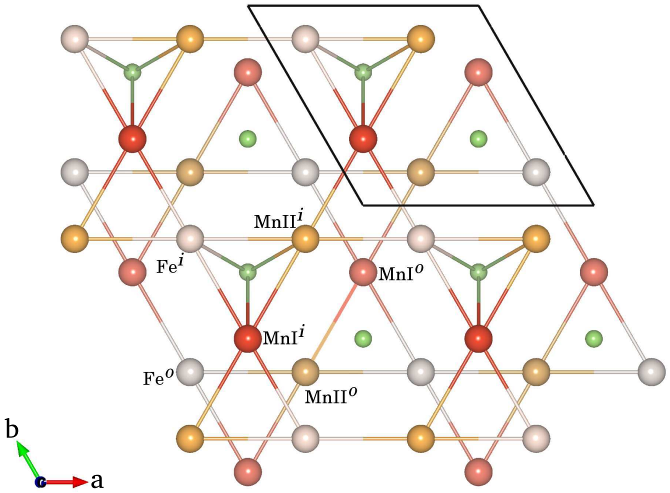

Figure 5.10: The nearest neighbour Mn-Mn and Mn-Fe bonds in DO_{19} structure of Mn_2FeGa are shown(a view from c axis). Network with two adjacent basal planes(the unit is shown on the top right corner with black border) are shown. Atoms marked 'i' and 'o' correspond to whether they are in plane or out of plane, respectively. The relatively darker circles associated with each colour are at the top kagome plane and the relatively lighter circles are at the bottom kagome plane. The colour codes are the ones used in other figures.

as opposed to the non-collinear magnetic structure in Mn_3Ga where the neighbouring atoms (both in-plane and out-of plane) align themselves in a triangular structure with an angle of 120^0 between them indicates that Fe plays a vital role. The substantial magnetisation obtained in the measurements [62] on the DO_{19} phase of Mn_2FeGa was connected with the possibility of creation of Fe-Mn ferromagnetic matrix in the system. The magnetic exchange interactions calculated for this phase of Mn_2FeGa and presented in Fig. 5.11 helps understanding the origin of the collinear like magnetic structure obtained from the total energy calculations. The network of the nearest neighbour magnetic atoms in the two neighbouring planes in the DO_{19} structure is shown in Fig. 5.10. It is clear from the structure that there are two types of triangular networks in the basal planes-one with the shared Ga neighbours and one without. Consequently, the strengths of the interactions between the same pair of species at the same distance would be different in two networks. This was found out to be the case for Mn_3Ga where the in-plane interaction between Mn atoms with shared Ga was comparable to the interaction without shared Ga, which ensured the 120^0 orientation between the Mn neighbours belonging to different networks [262]. In the present case of Mn_2FeGa, we find that the in plane exchange parameters

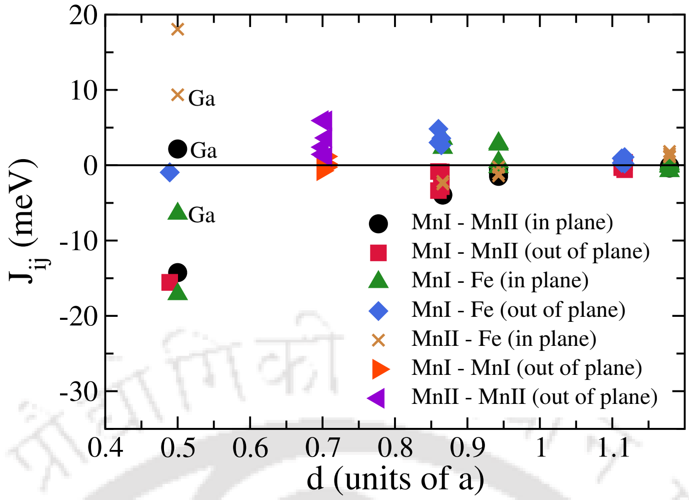

Figure 5.11: Magnetic exchange interaction(J_{ij}) of Mn_2FeGa as a function of inter atomic distance(d) in the DO_{19} phase.

for the three pairs of magnetic atoms are heterogeneous. While the MnI-MnII and MnI-Fe first neighbour interactions without shared Ga are strongly antiferromagnetic, the MnII-Fe interactions are strongly ferromagnetic with magnitudes of the three interactions comparable. The same qualitative features are observed for the interactions with networks having Ga atoms in between, although the strength of the interactions are reduced, yet non-negligible. These ensure that the frustration in the system is destroyed and we obtain a collinear like magnetic structure. The out-of-planes interactions too fail to induce any frustration as the dominating second neighbour out-of-plane ferromagnetic interactions are about 3 times smaller than the first neighbour out of plane antiferromagnetic interaction. Thus, the presence of Fe in the system indeed introduces substantial Fe-Mn ferromagnetic interactions in the system getting rid of the possible frustration as was conjectured [62].

5.4 Conclusions

The presented investigation of the structural and magnetic properties of four different structural phases of Mn_2FeGa in the framework of same first-principles method enables us to understand the microscopic physics associated with different physical aspects as well as the similarities and differences with the prototype Mn_3Ga from which the system under present investigation can be derived, and which is having similar promising applications in the area of spintronics. We find striking similarity between the two systems with regard to relative stabilities of the structural phases. Particularly important was to investigate the importance of the X_a phase which has not been synthesised experimentally. We find that the X_a phase provides an important connection between the hexagonal DO_{19} and the tetragonal $L1_0$ phase. However, we find that the phase is mechanically unstable to anisotropic stress. The origin of the electronic instability associated with this phase appears to be Jahn-Teller effect. The analysis of the electronic structures reveal that the significant hybridisations between Mn and Fe atoms are responsible for the stabilities and atomic magnetism of the other three phases investigated. While Mn_2FeGa has substantial similarities with Mn_3Ga in these aspects, there are significant qualitative differences in the magnetic structures. Unlike the tetragonal DO_{22} phase of Mn_3Ga, where a canted spin structure associated with one of the Mn sites was observed, the tetragonal $L1_0$ phase of Mn_2FeGa has a collinear magnetic structure. The results of magnetic exchange interactions clearly showed that the equally strong ferromagnetic Fe-Mn interactions and antiferromagnetic Mn-Mn interactions are responsible for the collinear ferrimagnetic structure in this phase as well as in the X_a phase. The magnetic structure in the hexagonal DO_{19} phase is where we observe substantial impact of the presence of Fe in the system. The non-collinear magnetic structure in Mn_3Ga, which was an artefact of the geometric frustrations and magnetic frustrations due to Mn-Mn exchange interactions now gives way to a collinear like magnetic structure with spins confined to $a-b$ plane, which is energetically almost degenerate to a collinear configuration with z-axis as the easy axis. The origin of this is found to be strong ferromagnetic Fe-Mn components in an antiferromagnetic host as was suggested in the experiment [62].

Chapter 6

Site occupancy, composition and magnetic structure dependencies of martensitic transformation in $\mathbf{Mn}_2\mathbf{Ni}_{1+x}\mathbf{Sn}_{1-x}$

6.1 Introduction

Larger martensitic transformation temperature (T_m) and Curie temperature (T_c) of Mn_2NiGa in comparison to the prototype and intensely studied Ni_2MnGa as well as high cost of Ga motivated researchers to explore Mn_2NiZ alloys with Z other than Ga. Subsequently, first-principles Density Functional Theory (DFT) calculations were performed on Mn_2NiZ (Z=Al, In, Sn) systems [65, 66, 77]. From the total energy surfaces and insignificant changes in their volumes upon a tetragonal distortion of their high temperature cubic phases, these studies concluded that all of them undergo volume-conserving martensitic transformations at low temperatures and thus could be suitable for shape memory applications. However, there were no experimental evidences to back this claim. The only available experimental investigation on this series of compounds was on Mn_2NiSn [251, 268] which found no evidence of structural transformation in this system. However, Mn_2NiSn drew attention because of a high value of magnetisation and a Curie temperature of 530 K. The high value of magnetisation was surprising since the DFT calculations [75–77] and experimental measurements [64, 65] revealed that the magnetic moments of

---

The contents of this chapter are published in J. Phys.: Condens. Matter **30**, 015401 (2018). Necessary permission to use the material in this thesis has been obtained from the journal.

Mn_2NiZ compounds are rather low ($\approx 1\mu_B$), contrary to the expectation; the reason being the anti-parallel coupling of the two Mn atoms. The high magnetisation value in Mn_2NiSn was attributed to the presence of Mn-Ni antisites [251]. Another DFT based investigation [78] subsequently established the correlation between presence of antisites and jump in magnetisation in these systems. Thus, it appeared that there is a significant connection between the site occupancies and magnetism in Mn-excess Mn-Ni-Sn system.

With a motivation to explore the possibility of a martensitic transformation in Mn-excess Mn-Ni-Sn system, a series of experiments were recently performed by varying the composition ratio of Ni and Sn in Mn_2NiSn compound. It may be noted that martensitic transformations could be observed in Ni_2MnSn and Ni_2MnIn systems only when the ratio of Mn to Sn(In) contents were varied [269–272]. The same trend was observed in the experiments on $Mn_2Ni_{1+x}Sn_{1-x}$ alloys. The eluding martensitic transformation was observed for low Sn content compounds. More importantly, the results indicated intricate relationships between the martensitic stability, composition, atomic ordering and magnetic order. Martensitic transformations were observed only for the compositions $0.56 \leq x \leq 0.92$ [79, 80, 82, 273, 274]. The magnetic states of the compounds in this composition range offered interesting perspective regarding the role of magnetism in martensitic stability. The martensitic transformation temperature, which was having a very high value ($\sim$ 800 K) for $x = 0.92$ was found to decrease with decreasing x bringing it down below room temperature at $x = 0.64$. Giant exchange bias was also observed for systems with $x = 0.56 - 0.68$ [79, 80, 83] in their martensitic phases indicating that there are competing ferromagnetic and antiferromagnetic domains possibly due to distribution of Mn atoms at different sites. The magnetic structure in the martensitic phase for $x > 0.64$ was considered to be paramagnetic by Ma *et al.* [82], while ordered magnetic phases were inferred from experimental results for $x \leq 0.64$. The phase diagram [82] suggested that in the range $0.52 \leq x \leq 0.6$, where martensitic and magnetic transitions occur below room temperature, both the austenite and martensite phases are magnetically ordered. The martensite phase was found to be losing stability with the increasing order of the magnetic state finally stabilising a magnetically ordered austenite phase at low temperature for $x < 0.56$. Large changes in the magnetisation across the martensitic transformation for $x = 0.6$ hinted at the changes in magnetic order along with changes in the crystal structure leading to magneto-structural effects [82]. The particular alloy $Mn_2Ni_{1.6}Sn_{0.4}$ was subsequently investigated by many researchers [275–279]. In a nutshell, the results demonstrated that the composition, site ordering and the magnetic order are coupled with the stability of the martensitic phase in this system. However, there has been no investigation yet to understand this interrelation from a fundamental point of view.

In this chapter, we make such an attempt with the help of first-principles DFT based methods. We look at the effects of composition, site occupancies and magnetic order on the martensitic stability of $Mn_2Ni_{1+x}Sn_{1-x}$ by changing each one of them in a systematic way. We evolve a qualitative picture of the fundamental physics associated with the various factors influencing the phase stability in this system from the results on energetics, magnetic moments and the electronic structures. We put special emphasis on the system $Mn_2Ni_{1.6}Sn_{0.4}$ since all the factors affecting martensitic stability may be at play for this particular system.

6.2 Computational Methods

Electronic structure calculations were performed with spin-polarized density functional theory (DFT) based projector augmented wave (PAW) method as implemented in Vienna Ab-initio Simulation Package (VASP) [120, 177, 178]. For all calculations, we have used Perdew-Burke-Ernzerhof implementation of Generalised Gradient Approximation (GGA) for exchange-correlation functional [179]. An energy cut-off of 450 eV and a Monkhorst-Pack [180] $11 \times 11 \times 11$ k-mesh were used for self consistent calculations. A larger k-mesh of $15 \times 15 \times 15$ was used for the calculations of the electronic structures. The convergence criteria for the total energies and the forces on individual atoms were set to 10^{-6} eV and 10^{-2} eV/Å respectively.

In order to calculate the magnetic moment and density of states (DOS) for a off-stoichiometric compound, close to experimental composition, we used the multiple scattering Green function formalism as implemented in SPRKKR code [141] by employing the coherent potential approximation (CPA) [127]. For self consistent calculations by the SPRKKR code, the full potential spin polarised scalar relativistic Hamiltonian with angular momentum cut-off $l_{max} = 3$ is used along with a converged k-mesh for Brillouin zone integrations. The Green's functions are calculated for 32 complex energy points distributed on a semi-circular contour. The energy convergence criterion was set to 10^{-6} eV for the self-consistency cycles. The experimental lattice parameters were used in these calculations for comparison with experiments.

6.3 Results and Discussions

Like Mn_2NiGa, the high temperature austenite phase of stoichiometric Mn_2NiSn is Hg_2CuTi or Inverse Heusler structure as described in chapter 1. The Sn atom occupy the 4d Wyckoff position as Ga in case of Mn_2NiGa [76, 251]. The same crystal structure is observed in the experiments on $Mn_2Ni_{1+x}Sn_{1-x}$. However, with Ni-excess, Sn-deficient systems, the occupancies at various sites change. Experimental observations predict that instead of the excess Ni atoms occupying the empty Sn-sites, the excess Ni atoms occupy the MnI sites which are crystallographically equivalent, thus displacing the MnI atoms to the empty Sn sites [79, 80, 280]. This site-occupancy pattern is consistent with the observed one in Heusler alloys where constituents with higher valence electrons occupy symmetric positions (4a and 4b) [55, 56, 251]. Accordingly, we have modelled the $Mn_2Ni_{1+x}Sn_{1-x}$ system with a 16 atom conventional cubic cell where each Wyckoff position corresponding to the Hg_2CuTi structure has four sub-lattices. However, any arbitrary composition can't be modelled with the cell of this size. Only compositions with $x = 0, 0.25, 0.5, 0.75, 1$ can be modelled. Modelling with any arbitrary value of x within the framework of DFT-PAW formalism as implemented in VASP requires very large supercells which is computationally demanding. Due to this limitation, we have focused on understanding the trends in properties with compositional changes, rather than working in a significantly narrow composition range and look for quantitative accuracy. After fixing the site occupancies in line with the experimental prediction and the empirical rule based on valence electron numbers, we look for the possible magnetic configurations. For $Ni_2Mn_{1+x}Z_{1-x}$ systems, it was found out that the magnetic ground state is dependent on the site preferences of the magnetic atoms [281, 282]. For stoichiometric Mn_2NiSn, the Mn atoms (MnI and MnII) are anti-parallely coupled [76]. For $Mn_2Ni_{1+x}Sn_{1-x}$, though the MnI and MnII still couple anti-parallely, the MnII and MnIII (The Mn atoms occupying the 4d positions, originally held by Sn in Mn_2NiSn) can be coupled parallely or anti-parallely depending upon their inter-atomic distances. One can find the ground state by comparing energies of the system (with a fixed site occupancy pattern) between the possible magnetic configurations [282].

In Fig. 6.1, the variations in calculated lattice parameters of $Mn_2Ni_{1+x}Sn_{1-x}$ in the austenite phase, as a function of x, are shown for both FM (MnII and MnIII align parallel) and AFM (MnII and MnIII align anti-parallel) magnetic configurations. We find that irrespective of the magnetic configuration, the lattice parameter decreases with x. This can be correlated to the smaller size of Ni (atomic radius 1.35 Å) in

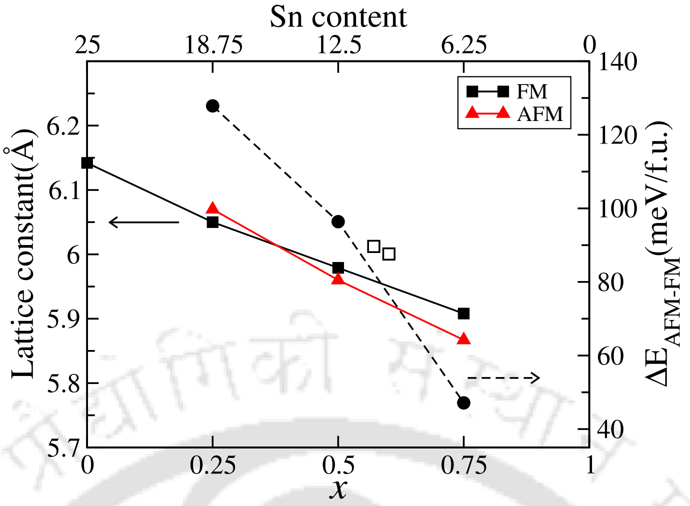

Figure 6.1: The solid lines correspond to the calculated lattice parameters in the austenite phase of $Mn_2Ni_{1+x}Sn_{1-x}$ with FM and AFM configurations (see text for FM and AFM). The dashed line corresponds to the energy differences between AFM and FM configurations as a function of x, in the austenite phase. A positive ΔE indicates the FM configurations have lower energy. Open symbols represent the experimental lattice parameters [279]. The top x-axis represent the Sn content in $Mn_{50}Ni_{50-y}Sn_y$.

comparison with Sn (atomic radius 1.45 Å). Better agreement with the experimental measurements [82, 279] are obtained for the calculated lattice parameters in the FM configuration, as is clear from Fig. 6.1. To find the ground state magnetic configuration in the cubic phase, we calculated the energy difference (ΔE_{AFM-FM}) between AFM and FM configurations. The positive value of ΔE_{AFM-FM} for all x, indicates that the FM states are energetically favourable (Fig. 6.1) throughout the composition range in the austenite phase.

The martensitic transformation in $Mn_2Ni_{1+x}Sn_{1-x}$ is observed for x between 0.56 and 1. With the cell size used in this work, it is not possible to scan the entire concentration range $x = 0.56 - 1.0$. However, it is possible to investigate the trends in the martensitic transformation by calculating total energies for $x = 0.25, 0.5, 0.75$ after distorting the cubic structure along c-axis. In what follows, we have calculated the total energy as a function of c/a for both FM and AFM configurations. The results are shown in the Fig. 6.2. In the austenite phase ($c/a = 1$), the lowest energy magnetic configuration is FM across compositions. Also, we do not see any energy minima corresponding to a (c/a) in the FM configuration except a shallow one at $x = 0.5$. A stable martensitic phase is observed at a $c/a > 1$ in this composition but with AFM magnetic configuration. The energy difference between this AFM tetragonal and the FM cubic phase is about 33 meV/atom. For $x = 0.5$, the AFM

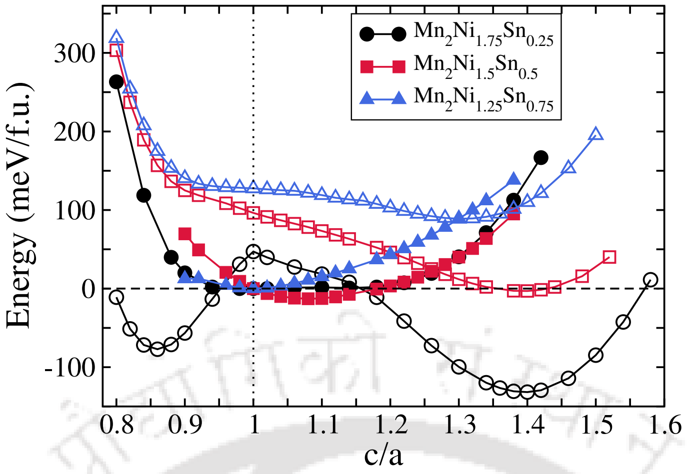

Figure 6.2: The variation of total energy as a function of tetragonal distortion (c/a) for $Mn_2Ni_{1+x}Sn_{1-x}$ (x=0.75, 0.5, 0.25) with FM and AFM configurations. The zero energy is the energy of the FM austenite ($c/a = 1$) phase for all the compositions. Open symbols represent the AFM configurations.

configuration produces a tetragonal ($c/a > 1$) phase which is energetically lower than the FM configuration for the system with same x, but the energy difference between this tetragonal phase and the global minima in the cubic phase is only about 1 meV per atom. For the system with $x = 0.25$, the energy of the tetragonal ($c/a > 1$) phase with AFM configuration is much higher than the global minima in the cubic phase. The results, therefore suggest that the martensitic transformation temperature T_m will decrease as the Sn content(x) increases(decreases) since the energy difference between the AFM tetragonal phase and the global FM cubic phase decreases. For $x = 0.75$, the global minima in the tetragonal phase occurs in the AFM configuration and is energetically lower than the global minima in the cubic phase which has a FM configuration. For $x = 0.5$, a composition, almost at the edge of the composition range where martensitic transformation is observed experimentally, the energy of the tetragonal phase is almost same as that of the cubic global minima. This signifies that the martensitic phase is nearly de-stabilised at this composition. Further increase in Sn content ($x = 0.25$) clearly shows that the energy of the tetragonal phase, with AFM configuration, is significantly higher than the energy of the global minima in the cubic phase obtained with the FM configuration. These results are qualitatively in agreement with the experimental observations [82]. Moreover, the following general qualitative picture regarding the effects of site occupancy, composition and the magnetic order on martensitic transformations in $Mn_2Ni_{1+x}Sn_{1-x}$ emerges out of these results: (i) the increase in Sn content at the expense of Ni destabilises the martensitic phase. Ni has played a crucial role in stabilising the martensitic phases in Ni-Mn-Ga systems [189]. We see the same being repeated in the case of the present system, (ii) the site occupancies are important for the occurrence or disappearance of martensitic phase in this system. Previous DFT calculations on Mn_2NiSn [77, 78] showed a lower total energy in a tetragonal phase ($c/a > 1$) than that in the cubic phase. Inspite of introducing antisites in 4a and 4b sites, it remained so. The results in Fig. 6.2 imply that the energy in the tetragonal phase will remain much higher than the global minimum energy in the cubic phase when $x = 0$ that is for the compound Mn_2NiSn. This will be in agreement with the experimental observations. The key to this will be the site occupancy pattern. In earlier DFT calculations, the 4d site was considered to be fully occupied by Sn. In this work, we see the systematic de-stabilisation of the martensitic phase, evidenced by increasing higher total energy in this phase, when the 4d site is always occupied by Mn atoms. We can, thus, infer that even in Mn_2NiSn, the 4a and 4d sites will have Mn-Sn binary alloy, (iii) the magnetic configuration in the martensitic phase would be different from that in the austenite phase. The reason behind this can be traced to the distance between the MnII and MnIII atoms. The tetragonal distortion brings these two atoms closer than they were in the austenite phases, introducing antiferromagnetic interaction between them and stabilising the AFM configuration in the martensitic phase.

A physically measurable and important quantity in magnetic compounds that is very sensitive to the site ordering and magnetic structure is the magnetisation. In case of Mn_2NiZ alloys, earlier DFT calculations have clearly shown this [76, 78]. In case of $Mn_2Ni_{1.6}In_{0.4}$ MSMA, a very high value of saturation magnetisation in the austenite phase was attributed to the co-existence of different magnetic domains-one with usual Mn(4a), Mn(4c), Ni(4b), In-Ni(4d) stacking while the other with Mn-Ni(4a),Mn(4b),Ni(4c), Mn-In(4d) stacking, thus, having both anti-parallel (Mn(4c)-Mn(4a)) and parallel (Mn(4c)-Mn(4d)) alignments among Mn atoms [283]. Similarly, in $Mn_2Ni_{1+x}Sn_{1-x}$ systems, the magnetisation can be sensitively dependent upon the site occupancy induced magnetic couplings among Mn atoms. Since the magnetisation measurements have not been done on any of the compounds with $x = 0.25, 0.5, 0.75$, we investigate the influence of site occupancy on magnetic moment for $Mn_2Ni_{1.6}Sn_{0.4}$ whose magnetisation has been investigated by various groups [82, 274, 279, 284]. The magnetisation measurements by various groups suggest that it will saturate only at very high field; the measured value at a high field of 13 Tesla is 3.37 μ_B per formula unit [82]. Using KKR-CPA method as implemented in the SPRKKR code, we have calculated the magnetic moment per formula unit

Table 6.1: The configurations associated with different site occupancy patterns in the austenite phase of Mn$_2$Ni$_{1.6}$Sn$_{0.4}$ (x=0.6), their total energies (E$_{tot}$) in $meV/f.u.$ and total magnetic moment (M$_s$) in $\mu_B/f.u.$

	Sites and occupancies					
Config.	4a	4b	4c	4d	E$_{tot}$	M$_S$
C$_1$	Mn	Ni	Mn	Ni$_{0.6}$Sn$_{0.4}$	0	0.14
C$_2$	Mn$_{0.9}$Ni$_{0.1}$	Ni	Mn	Mn$_{0.1}$Ni$_{0.5}$Sn$_{0.4}$	-70.791	1.06
C$_3$	Mn$_{0.8}$Ni$_{0.2}$	Ni	Mn	Mn$_{0.2}$Ni$_{0.4}$Sn$_{0.4}$	-165.755	1.97
C$_4$	Mn$_{0.7}$Ni$_{0.3}$	Ni	Mn	Mn$_{0.3}$Ni$_{0.3}$Sn$_{0.4}$	-285.681	2.88
C$_5$	Mn$_{0.6}$Ni$_{0.4}$	Ni	Mn	Mn$_{0.4}$Ni$_{0.2}$Sn$_{0.4}$	-428.402	3.80
C$_6$	Mn$_{0.5}$Ni$_{0.5}$	Ni	Mn	Mn$_{0.5}$Ni$_{0.1}$Sn$_{0.4}$	-590.361	4.71
C$_7$	Mn$_{0.4}$Ni$_{0.6}$	Ni	Mn	Mn$_{0.6}$Sn$_{0.4}$	-782.417	5.60

Table 6.2: Possible site occupations of Mn$_2$Ni$_{1+x}$Sn$_{1-x}$ ($x = 0, 0.25, 0.5, 0.75$) in the 16 atom supercell and their physical properties. a$_0^{\rm FM}$ and a$_0^{\rm AFM}$ are the equilibrium lattice constants with FM and AFM configurations in the austenite phase respectively. M$_{tot}^{\rm FM}$ is the calculated total magnetic moment with the FM configuration.

	Sites and occupancies							
Systems	4a	4b	4c	4d	system name	a$_0^{\rm FM}$(Å)	a$_0^{\rm AFM}$(Å)	M$_{tot}^{\rm FM}$($\mu_B/f.u.$)
Mn$_8$Ni$_4$Sn$_4$ (Mn$_2$NiSn)	Mn$_4$	Ni$_4$	Mn$_4$	Sn$_4$	Sn4	6.142	-	0.57
Mn$_8$Ni$_5$Sn$_3$ (Mn$_2$Ni$_{1.25}$Sn$_{0.75}$)	Mn$_4$	Ni$_4$	Mn$_4$	Sn$_3$Ni$_1$	Sn3Ni1	6.060	-	0.30
	Mn$_3$Ni$_1$	Ni$_4$	Mn$_4$	Sn$_3$Mn$_1$	Sn3Mn1	6.052	6.064	2.44
Mn$_8$Ni$_6$Sn$_2$ (Mn$_2$Ni$_{1.5}$Sn$_{0.5}$)	Mn$_4$	Ni$_4$	Mn$_4$	Sn$_2$Ni$_2$	Sn2Ni2	5.956	-	0.14
	Mn$_3$Ni$_1$	Ni$_4$	Mn$_4$	Sn$_2$Mn$_1$Ni$_1$	Sn2Mn1Ni1	5.965	5.969	2.04
	Mn$_2$Ni$_2$	Ni$_4$	Mn$_4$	Sn$_2$Mn$_2$	Sn2Mn2	5.979	5.960	4.28
Mn$_8$Ni$_7$Sn$_1$ (Mn$_2$Ni$_{1.75}$Sn$_{0.25}$)	Mn$_4$	Ni$_4$	Mn$_4$	Sn$_1$Ni$_3$	Sn1Ni3	5.845	-	0.14
	Mn$_3$Ni$_1$	Ni$_4$	Mn$_4$	Sn$_1$Mn$_1$Ni$_2$	Sn1Mn1Ni2	5.856	5.860	2.08
	Mn$_2$Ni$_2$	Ni$_4$	Mn$_4$	Sn$_1$Mn$_2$Ni$_1$	Sn1Mn2Ni1	5.878	5.866	4.22
	Mn$_1$Ni$_3$	Ni$_4$	Mn$_4$	Sn$_1$Mn$_3$	Sn1Mn3	5.908	5.867	6.44

of Mn$_2$Ni$_{1.6}$Sn$_{0.4}$ by varying the occupancies of 4a and 4d sites. The results of total energies and magnetic moments for seven possible configurations are given in Table 6.1. When excess Ni completely occupies the 4d site, the energy of the system is highest and the moment is almost quenched due to compensating anti-aligned moments of MnI and MnII. On the other hand, when excess Ni completely occupies 4a site pushing equal amount of MnI to 4d site, the system has the lowest total energy and the highest magnetic moment. This high magnetic moment is due to the ferromagnetic coupling between MnII and MnIII atoms.

Inspite of having the lowest total energy, the magnetic moment of configuration C$_7$ disagrees with the measured saturation magnetisation significantly. On the other hand, the measured value of saturation magnetisation lies in between the values calculated in the configurations C$_4$ and C$_5$ which have Ni content of 30% and 20% at 4d site respectively. The gradual decrease of magnetic moment with increasing

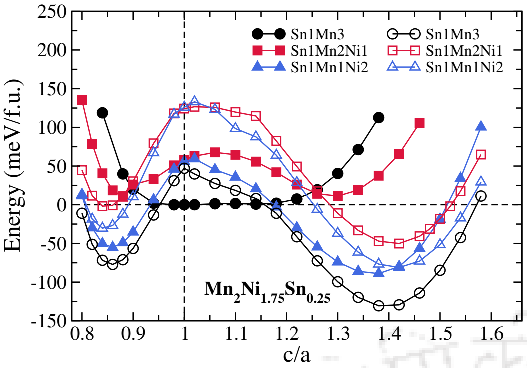

Figure 6.3: The variation of total energy as a function of c/a ratio for $Mn_2Ni_{1.75}Sn_{0.25}$ with possible configurations given in Table. 6.2. The zero energy is the energy of the Sn1Mn3 system in the FM austenite phase. Open symbols represent the AFM states.

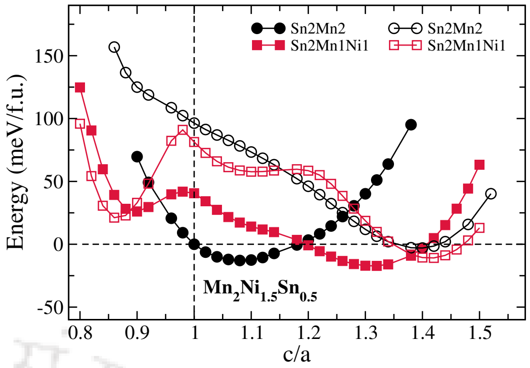

Figure 6.4: The variation of total energy as a function of c/a ratio for $Mn_2Ni_{1.5}Sn_{0.5}$ with possible configurations given in Table. 6.2. The zero energy is the energy of the Sn2Mn2 system in the FM austenite phase. Open symbols represent the AFM states.

Ni content at 4d site is the result of progressive weakening of MnII-MnIII ferromagnetic component and subsequent strengthening of MnI-MnII antiferromagnetic component. Based upon these results, we conclude that there can be a mixture of domains with different site occupancy patterns in the polycrystalline sample used for magnetic measurements.

The question now remains is whether site occupancy patterns with some Ni at the 4d site can reproduce the trend with regard to martensitic stability as a function of composition as observed experimentally and is explained through Fig. 6.2. To understand the effect of site occupancy on the stability of the martensitic phases, we have calculated the total energies as a function of c/a for $Mn_2Ni_{1+x}Sn_{1-x}$ ($x = 0.5, 0.75$) with different occupancies of the 4a and 4d sites for each of FM and AFM magnetic configurations. The results are shown in Fig. 6.3 and 6.4. The configurations considered for each x are given in Table 6.2. The system name against each site occupancy pattern is given in column 6 of Table 6.2. In the results presented in Fig. 6.3 and 6.4, we have not included the cases where no Mn atom occupies the 4d sites (systems Sn1Ni3 and Sn2Ni2). This is because the magnetic moments calculated in these configurations are extremely low (Table 6.2), clearly in severe disagreement with the experiments as is seen in case of $x = 0.6$ (Table 6.1). Moreover, for any x, such configurations always produced lowest total energies for a $c/a \neq 1$, indicating a energetically favourable martensitic phase at low temperature irrespective of the Ni (Sn) content in the system which is in contradiction to the experimental observations.

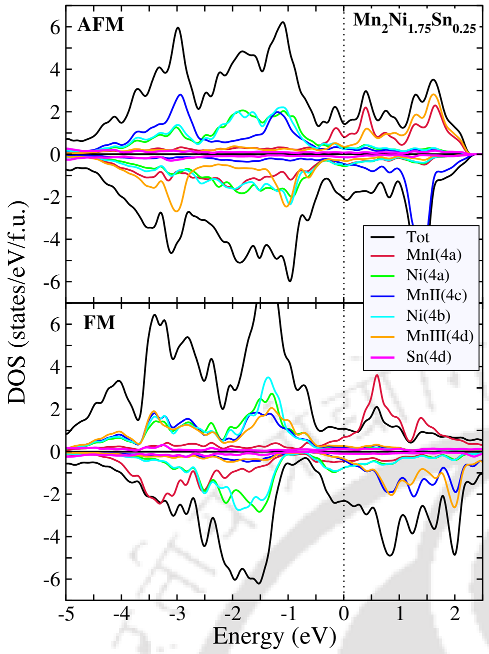

Figure 6.5: Total and atom projected density of states of $Mn_2Ni_{1.75}Sn_{0.25}$ (Sn1Mn3) system with FM and AFM configurations in the austenite phase. The zero of the energy is set at Fermi level (E_F).

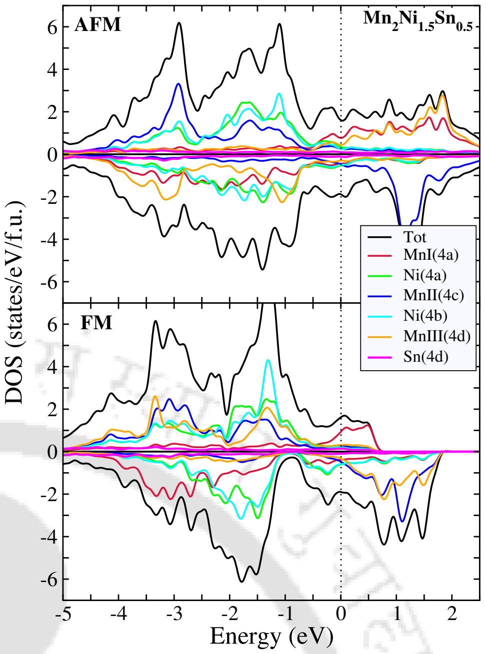

Figure 6.6: Total and atom projected density of states of $Mn_2Ni_{1.5}Sn_{0.5}$ (Sn2Mn2) system with FM and AFM configurations in the austenite phase. The zero of the energy is set at Fermi level (E_F).

In case of $Mn_2Ni_{1.75}Sn_{0.25}$, the FM magnetic structure provides the lowest total energy for the austenite phase ($c/a = 1$) when the 4d site has Mn and Sn only (the system Sn1Mn3). The total energy curve does not imply any possibility of a martensitic transformation with FM structure in this system. When a fraction of Ni atoms starts occupying the Sn site (Sn1Mn2Ni1 and Sn1Mn1Ni2), a tetragonal phase produces lower total energy in the FM structure indicating a martensitic transformation (Fig. 6.3). When 4d site has 50% of Ni, the tetragonal phase with $c/a > 1$ is energetically lower than the global minimum for the austenite phase ($c/a = 1$). With the AFM magnetic structure, all site occupancies stabilise the martensitic phases as can be understood from total energies being lower in the tetragonal phases than the global minimum in the austenite phase. Two things, therefore, emerge: (i) at this composition, the anti-ferromagnetic interaction between MnII and MnIII atoms stabilise the martensitic phase, irrespective of the site occupancies at the 4a and 4d sites, and (ii) the presence (absence) of more Ni (Mn) at the 4d site stabilises the martensitic phase irrespective of the magnetic structure. Thus we see comparable total energies in the FM and AFM configurations for the tetragonal phases of the system Sn1Mn1Ni2 (50% of Ni at 4d site) near their respective energy minima. For $Mn_2Ni_{1.5}Sn_{0.5}$, irrespective of whether Ni occupies 4d site or not, shallow minima at a $c/a \neq 1$ are obtained in the FM configuration. For the AFM configurations, although the total energies in the tetragonal phases are much lower than those in the respective cubic phases, they are comparable to the global minimum in the austenite phase. This implies that at this composition, the martensitic stability is almost insensitive to the site occupancy as long as Mn occupies 4a, 4b and 4d sites. In fact, the shallow minima of the tetragonal structure for all magnetic configurations and all site occupancies suggest that the system has a tendency towards stabilising the austenite phase at the low temperature; the magnetic configuration being the FM and the best stability is achieved for 4d site having Mn and Sn only.

In order to understand the connection between the preferred magnetic state and the stability of the martensitic phase from a microscopic point of view, we present the densities of states (DOS) of austenite phases of $Mn_2Ni_{1.75}Sn_{0.25}$ and $Mn_2Ni_{1.5}Sn_{0.5}$, with FM and AFM configurations. The results are shown in Fig. 6.5 and 6.6, respectively. The densities of states are calculated with Sn1Mn3 and Sn2Mn2 systems (Table 6.2) for $Mn_2Ni_{1.75}Sn_{0.25}$ and $Mn_2Ni_{1.5}Sn_{0.5}$, respectively. In case of FM configuration of $Mn_2Ni_{1.75}Sn_{0.25}$ (Fig. 6.5), a pseudogap is observed at -0.75 eV in the minority DOS which results from hybridizations between Sn-p and Ni-, MnI-d states. This pseudogap indicates a strong covalent bonding in the FM states [282, 285, 286] resulting in the stability of the austenite structure with FM magnetic configuration. In case of AFM magnetic configuration, the pseudogap disappears due to the additional states of MnIII in the minority DOS around the same energy. In this case, the $d-d$ hybridization becomes stronger resulting in weaker covalent bonding as compared to the FM case. Thus the austenite phase with AFM configuration has less stability. This corroborates the trends in the energetics presented in Fig. 6.2. Another noteworthy feature is that in the AFM configuration, the Fermi energy cuts through a small peak in the minority DOS. This peak is associated with the Jahn-Teller distortion leading to the stability of the martensitic phase. The competitive effect of the strong covalent bonding in the occupied part of the minority DOS giving rise to a pseudogap and the Jahn-Teller effect near the Fermi level giving rise to a peak very near or at the Fermi level has been used to explain the martensitic stability in a number of Ni-Mn-Z systems [281, 282]. In the AFM configuration of the present case, the simultaneous disappearing of the pseudogap and emergence of the Jahn-Teller peak at the Fermi level explains the stability of the martensitic phase with this magnetic configuration. For $Mn_2Ni_{1.5}Sn_{0.5}$, the pseudogap in the

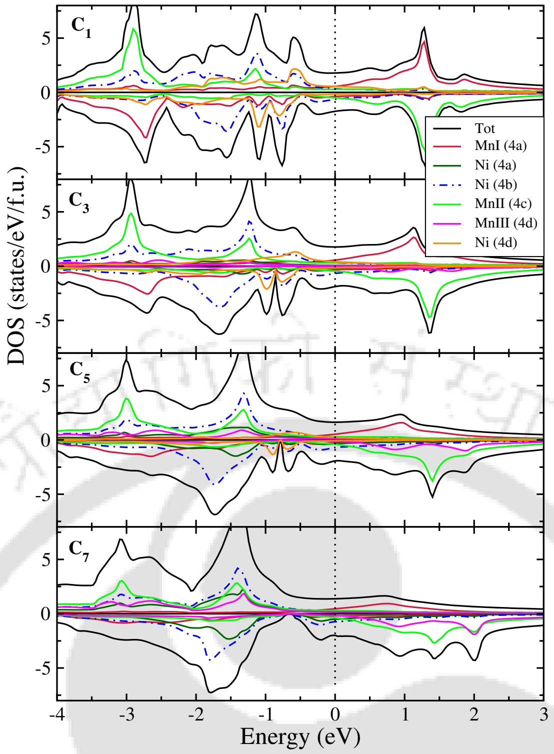

Figure 6.7: Total and atom projected density of states of $Mn_2Ni_{1.6}Sn_{0.4}$ system with FM configuration in the austenite phase and with different site occupations as presented in Table 6.1. The zero of the energy is set at Fermi level (E_F).

minority DOS for FM configuration is deeper indicating a stronger covalent bonding leading to a greater stability of the austenite phase with FM configuration at low temperature in comparison to $Mn_2Ni_{1.75}Sn_{0.25}$. For the AFM magnetic configuration, we once again see the filling of the pseudogap due to MnIII states and simultaneous weakening of the covalent bonding giving way to the Jahn-Teller effect. Thus, the electronic structures demonstrate the correlation between the stability of a particular phase with the magnetic configuration. The MnIII states clearly play the decisive role in all the compounds.

After understanding the role of MnIII atoms in stabilising the austenite phase in the FM magnetic configuration, we attempt fundamental understanding of the role of site ordering and stability by analysing the changes in the electronic structures with changes in the composition at the 4d site. For this purpose, we have calculated the DOS of $Mn_2Ni_{1.6}Sn_{0.4}$ as several configurations with both Ni and Mn at the 4d sites had been considered for this system, making it suitable to observe the changes in a finer range. The results with four different configurations taken from Table 6.1 are shown in Fig. 6.7. All calculations are done in the austenite phase with FM configuration. We find significant changes in the minority DOS as more and more Ni occupy 4d sites. The pseudogap near -0.75 eV which is prominent in the configuration C_7 (No Ni in 4d site) starts getting narrower and shallower as more and more Ni occupies 4d sites, due to the states of these Ni. Finally when the 4d site contains only Ni and Sn, the pseudogap almost disappears. The gradual weakening of the covalent bond manifested in disappearance of the pseudogap destabilises the cubic phase with FM configuration. The decrease in the magnetic moment from configurations C_7 to C_1 (Table 6.1) can be understood from these features as well. The gradual reduction of the MnIII atoms from the system weakens the ferromagnetic part in the magnetic interaction which was mostly due to MnII and MnIII atoms, resulting in the loss of total moment with increase of Ni at the 4d sites. These features provide explanations for the trends in the total energies and magnetic moments given in Table 6.1.

6.4 Conclusions

Using first principles density functional based calculations, we have investigated the interrelations between composition, site occupancy, magnetic structure and martensitic stability in $Mn_2Ni_{1+x}Sn_{1-x}$ systems and interpreted the results from their electronic structures. We find that the ferromagnetic interaction among the Mn atoms at the 4c sites and at the 4d sites stabilise the austenite phases while the anti-ferromagnetic interactions among them due to shortening of their bond distances under a tetragonal distortion stabilise the martensitic phases. The covalent bonding between the MnI, Ni and Sn minority states stabilises the austenite phases when MnII-MnIII interactions are ferromagnetic while the presence of MnIII states in the minority bands when MnII-MnIII anti-align reduces this stability. Subsequently, the anti-alignment of MnII and MnIII atoms strengthens the competing Jahn-Teller effect leading to the stability of the martensitic phases. Apart from the MnIII atoms, the Ni atoms at the 4d sites also play significant roles in the stability of the martensitic phases in this system. The Ni atoms at the 4d sites, unlike the Ni atoms at the 4b sites, weaken the covalent bonding by filling the pseudogap in the minority bands, de-stabilising the austenite phase. Thus, a delicate balance of Ni and Mn atoms in the 4d sites decides the magnetism and the phase stability of $Mn_2Ni_{1+x}Sn_{1-x}$ system. The results presented in this work, therefore, interpret the experimental observations by pinpointing the role of a number of factors like the site ordering, the composition and the magnetic interactions, which has not been done yet from a microscopic point of view. This study also provides us with a wider scope of interpreting the experimental results for similar systems like Mn-Ni-In where such interesting interrelations between a number of factors seem to be existing.

Chapter 7

Conclusions and scopes for future work

7.1 Conclusions

In this thesis, we have investigated the structural and magnetic properties of stoichiometric Mn_2NiGa and Mn_2FeGa, Fe and Co substituted Mn_2NiGa and the off-stoichiometric Mn_2NiSn alloys. These systems exhibit different functional properties leading to state of the art technologies. These different functional properties are related to their structural phase stability and magnetic orders. Using sophisticated *ab initio* techniques, we have provided microscopic pictures addressing the interrelations between structural phases, site ordering, compositions and magnetic structures in these materials

In the first chapter, the concepts relevant to the investigated Mn_2YZ compounds, such as martensitic transformation, magnetic shape memory effect, half-metallicity and exchange bias are given in detail along with possible technological applications. Various functional aspects of Mn_2YZ compounds and the research made on these materials so far are also discussed paving the way for justifications behind the problems addressed in this thesis.

In the next chapter, the theoretical methods that have been used in this thesis are discussed. A brief introduction of density functional theory (DFT) along with its different implementations are first presented. Approaches to compute physical properties like the ground state elastic properties and the finite temperature magnetic properties, that are used in this thesis, are then explained.

In the following chapter, we have performed comprehensive study of the structural and electronic properties of the different modulated variants in the martensitic phase of Mn_2NiGa. Our calculations confirm the existence of the experimentally observed 14M modulated martensite phases with two different symmetries. They also reveal the possible existence of other modulated martensites, 6M and 10M with orthorhombic symmetry and 10M($3\bar{2}$) with monoclinic symmetry. Using the total energy results, we have explained the structural phase transformation pathway and relative stability of different modulated structures which correspond well to the fact that the complementary phonon calculations in the cubic phase show that the dynamical instability in the high temperature cubic structure can be mapped onto a 6M modulated structure. The origin of the modulated phases in this system are explained from the nesting features of the Fermi surfaces and the calculations of electronic susceptibilities. The results presented in this chapter elucidate the similarities and differences between Mn_2NiGa and Ni_2MnGa, the prototype magnetic shape memory system.

In chapter 4, we have investigated the effects of Fe and Co substitutions on the stability of the martensitic phase, and mechanical, electronic and magnetic properties of Mn_2NiGa. The evolution of these aspects upon substitution of Fe and Co at different crystallographic sites is investigated by computing the electronic structure, mechanical properties (tetragonal shear constant, Pugh ratio and Cauchy pressure) and magnetic exchange parameters. We find that the site occupancy of the substituents plays a significant role in affecting the phase stability and other physical properties. For both Fe and Co substitutions, the austenite phase of Mn_2NiGa gradually stabilizes with increase in concentration of Fe/Co due to the weakening of the minority spin hybridization of Ni and Mn atoms occupying crystallographically equivalent sites. From the composition dependence of elastic constants, we find that the elastic shear modulus C' can be considered as a predictor of composition dependence of martensitic transformation temperature T_m in substituted Mn_2NiGa. From the correlated variation of Cauchy pressure and Pugh ratio, we have determined the strength of the covalent bonding in a given system which is well correlated with the electronic structures. Another interesting outcome of this work is that the magnetic and electronic properties of Mn_2NiGa change significantly when the Fe/Co is substituted at Ga or Mn sites. In case of complete substitution at any of the sites, the Jahn-Teller distortion (covalent bonding) in the minority spin densities of states become weaker (stronger), leading to a half-metallic-like gap in these compounds resulting in materials with high spin-polarization. Thus, multiple functionalities can be obtained in substituted Mn_2NiGa, depending upon the compositions, which makes these materials attractive. Our calculations predict that the substitutions at the Ga site result in two new compounds Mn_2NiFe and Mn_2NiCo which have very high magnetic moments and Curie temperatures.

In chapter 5, we have investigated the structural and magnetic properties of four different structural phases of Mn_2FeGa, each of which is related to a desirable functional property. We found that hitherto experimentally unobserved cubic Heusler phase provides an important connection between the hexagonal and the tetragonal phase. The cubic Heusler phase is mechanically unstable to anisotropic stress and the origin of the electronic instability of this phase appears mainly due to Jahn-Teller effect. The analysis of the electronic structures reveals that the significant hybridisations between Mn and Fe atoms are responsible for the stabilities and atomic magnetism of the different phases investigated. For the hexagonal phase, we have obtained a collinear like magnetic structure unlike the non-collinear magnetic structure in prototype Mn_3Ga. We investigate the inter atomic magnetic exchange interactions for all the phases and have found that the strong ferromagnetic Fe-Mn interactions and antiferromagnetic Mn-Mn interactions are responsible for the collinear ferrimagnetic structure.

In chapter 6, we investigate the interrelations between composition, site occupancy, magnetic structure and martensitic stability in $Mn_2Ni_{1+x}Sn_{1-x}$ systems. We find that the ferromagnetic interaction among the Mn atoms at the 4c and the 4d sites stabilises the austenite phases while the antiferromagnetic interactions among them due to shortening of their bond distances under a tetragonal distortion stabilise the martensitic phases. The covalent bonding between the MnI, Ni and Sn minority states stabilises the austenite phases when MnII-MnIII interactions are ferromagnetic while the presence of MnIII states in the minority bands when MnII-MnIII anti-align reduces this stability. Subsequently, the anti-alignment of MnII and MnIII atoms strengthens the competing Jahn-Teller effect leading to the stability of the martensitic phases. Apart from the MnIII atoms, the Ni atoms at the 4d sites also play significant role in the stability of the martensitic phases in this system. The Ni atoms at the 4d sites, unlike the Ni atoms at the 4b sites, weaken the covalent bonding by filling the pseudogap in the minority bands, de-stabilising the austenite phase. Thus, a delicate balance of Ni and Mn atoms in the 4d sites decides the magnetism and the phase stability of $Mn_2Ni_{1+x}Sn_{1-x}$ system.

7.2 Scopes for future work

Many different extensions of the work presented in the thesis have been left for the future. In our first work, we have extensively investigated the different modulated variants of Mn_2NiGa in the martensitic phase and their relative phase stability from the total energy calculation at 0 K. However, a full free energy calculation including contributions due to lattice vibrations and magnetic excitations would enable one to construct the structural phase diagram, and provide us with the required thermodynamic parameters to completely characterize the modulated phases.

Different experimental groups have reported the existence of site disorder in different structural phases of Mn_2FeGa. Thus the investigations of the free energy landscape can be done for Mn_2FeGa. These investigations including site disorder effect, can give a complete picture of different phases and their stability at finite temperatures. Also, the mechanism behind the structural transformations is not investigated in detail for this system. Extensions can be in these directions.

Fe and Co substitution in Mn_2NiGa produced some interesting results and useful insights into the physics of substitution in Mn_2NiGa system as discussed in chapter 4. One of the important results of this chapter is the prediction of two new half-metals Mn_2NiFe and Mn_2NiCo with very high magnetic moments and Curie temperatures. However, since experiments to corroborate this are not available, extensive computational studies on the possible crystal structures in which these two compounds can form and whether the half-metallicity and high magnetic parameters can be sustained in these structures need to be done in order to catch the attention of the experimentalists. This, thus, can be another direction to extend the work of the present thesis.

The investigation of site occupancy, composition and magnetic structure dependencies of martensitic transformation in off-stoichiometric Mn_2NiSn is done in chapter 6. This system has exhibited significant magnetocaloric effect for compositions close to the room temperature martensitic transformation. The present knowledge on this system as discussed in chapter 6 can be extended to investigate the magnetocaloric effect in this system.

Bibliography

[1] C. M. Wayman, *Introduction to the crystallography of martensitic transformations*, Macmillan, New York, 1964.

[2] H. Bhadeshia, Institute of Materials, London (2001).

[3] G. V. Kurdjumov and G. Sachs, Z. Phys. **64**, 325 (1939).

[4] E. C. Bain and N. Dunkirk, trans. AIME **70**, 25 (1924).

[5] H. K. D. H. Bhadeshia, Martensite in steels, http://www.msm.cam.ac.uk/phase-trans/2000/C9/lectures45.pdf.

[6] K. Otsuka and C. M. Wayman, *Shape memory materials*, Cambridge university press, 1999.

[7] T. W. Duerig, K. Melton, and D. Stöckel, *Engineering aspects of shape memory alloys*, Butterworth-Heinemann, 2013.

[8] A. Ölander, J. Am. Chem Soc **54**, 3819 (1932).

[9] A. B. Greninger and V. G. Mooradian, Trans. Amer. Inst. min. (metall.) Engrs **128**, 337 (1938).

[10] A. B. Greninger and V. G. Mooradian, Trans. Amer. Inst. min. (metall.) Engrs **133**, 204 (1939).

[11] L. Chang and T. Read, Trans. AIME **191**, 47 (1951).

[12] W. J. Buehler, J. Gilfrich, and R. Wiley, J. Appl. Phys. **34**, 1475 (1963).

[13] F. E. Wang, W. J. Buehler, and S. J. Pickart, J. Appl. Phys. **36**, 3232 (1965).

[14] J. M. Sater, Smart structures and materials 1997: Industrial and commercial applications of smart structures technologies, in *Smart Structures and Materials 1997: Industrial and Commercial Applications of Smart Structures Technologies*, volume 3044, 1997.

[15] K. E. Wilkes and P. K. Liaw, JOM **52**, 45 (2000).

[16] V. A. Chernenko, *Advances in magnetic shape memory materials : special topic volume with invited peer reviewed papers only*, Trans Tech Publications Ltd, Kreuzstrasse 10, Switzerland, 2011.

[17] A. Planes, L. Mañosa, and M. Acet, J. Phys.: Condens. Matter **21**, 233201 (2009).

[18] K. Ullakko, Journal of materials Engineering and Performance **5**, 405 (1996).

[19] S. J. Murray, M. Marioni, S. M. Allen, R. C. OHandley, and T. A. Lograsso, Appl. Phys. Lett. **77**, 886 (2000).

[20] A. Sozinov, A. Likhachev, N. Lanska, and K. Ullakko, Appl. Phys. Lett. **80**, 1746

(2002).

[21] A. Sozinov, A. Likhachev, and K. Ullakko, IEEE Trans. Magn. **38**, 2814 (2002).

[22] R. Tickle, R. James, T. Shield, M. Wuttig, and V. Kokorin, IEEE Transactions on Magnetics **35**, 4301 (1999).

[23] Q. Pan and R. James, J. Appl. Phys. **87**, 4702 (2000).

[24] Y. Lai, N. Scheerbaum, D. Hinz, O. Gutfleisch, R. Schäfer, L. Schultz, and J. McCord, Appl. Phys. Lett. **90**, 192504 (2007).

[25] A. Hubert and R. Schäfer, *Magnetic domains: the analysis of magnetic microstructures*, Springer Science & Business Media, 2008.

[26] R. C. O'handley, *Modern magnetic materials: principles and applications*, Wiley, 2000.

[27] C. Felser and G. H. Fecher, *Spintronics: from materials to devices*, Springer Science & Business Media, 2013.

[28] S. Murakami, N. Nagaosa, and S.-C. Zhang, Science **301**, 1348 (2003).

[29] E. Saitoh, M. Ueda, H. Miyajima, and G. Tatara, Appl. Phys. Lett. **88**, 182509 (2006).

[30] W. J. Gallagher, J. H. Kaufman, S. S. P. Parkin, and R. E. Scheuerlein, Magnetic memory array using magnetic tunnel junction devices in the memory cells, 1997, US Patent 5,640,343.

[31] K. Sin, S. Funada, H. C. Hiner, and X. Shi, Spin-dependent tunneling sensor suitable for a magnetic memory, 2002, US Patent 6,418,048.

[32] C. D. Mee and E. D. Daniel, *Magnetic recording; Vol. II: computer data storage*, McGraw-Hill, Inc., 1988.

[33] R. Coleman and A. Isin, J. Appl. Phys. **37**, 1028 (1966).

[34] M. N. Baibich et al., Phys. Rev. Lett. **61**, 2472 (1988).

[35] R. von Helmolt, J. Wecker, B. Holzapfel, L. Schultz, and K. Samwer, Phys. Rev. Lett. **71**, 2331 (1993).

[36] T. Miyazaki and N. Tezuka, J. Magn. Magn. Mater. **139**, L231 (1995).

[37] J. S. Moodera, L. R. Kinder, T. M. Wong, and R. Meservey, Phys. Rev. Lett. **74**, 3273 (1995).

[38] J. Åkerman, Science **308**, 508 (2005).

[39] S. Bhatti, R. Sbiaa, A. Hirohata, H. Ohno, S. Fukami, and S. Piramanayagam, Materials Today **20**, 530 (2017).

[40] J.-M. Hu, Z. Li, L.-Q. Chen, and C.-W. Nan, Nature communications **2**, 553 (2011).

[41] J. C. Sankey, Y.-T. Cui, J. Z. Sun, J. C. Slonczewski, R. A. Buhrman, and D. C. Ralph, Nature Physics **4**, 67 (2008).

[42] D. C. Ralph and M. D. Stiles, J. Magn. Magn. Mater. **320**, 1190 (2008).

[43] F. Radu, *Fundamental Aspects of Exchange Bias Effect in AF/F Bilayers and Multilayers*, PhD thesis, PhD thesis, Ruhr-Universität Buchum, 2005.

[44] W. H. Meiklejohn and C. P. Bean, Phys. Rev. **105**, 904 (1957).

[45] R. Morales, Z.-P. Li, J. Olamit, K. Liu, J. M. Alameda, and I. K. Schuller, Phys.

Rev. Lett. **102**, 097201 (2009).

[46] I. K. Schuller, R. Morales, X. Batlle, U. Nowak, and G. Güntherodt, J. Magn. Magn. Mater. **416**, 2 (2016).

[47] M. Khan, I. Dubenko, S. Stadler, and N. Ali, J. Appl. Phys. **102**, 113914 (2007).

[48] A. Nayak, M. Nicklas, S. Chadov, C. Shekhar, Y. Skourski, J. Winterlik, and C. Felser, Physical review letters **110**, 127204 (2013).

[49] K. Ullakko, J. K. Huang, C. Kantner, R. C. OHandley, and V. V. Kokorin, Appl. Phys. Lett. **69**, 1966 (1996).

[50] J. Winterlik et al., Adv. Mater. **24**, 6283 (2012).

[51] S. Singh et al., Phys. Rev. Lett. **109**, 246601 (2012).

[52] T. Kubota, S. Tsunegi, M. Oogane, S. Mizukami, T. Miyazaki, H. Naganuma, and Y. Ando, Appl. Phys. Lett. **94** (2009).

[53] S. Ouardi, G. H. Fecher, C. Felser, and J. Kübler, Phys. Rev. Lett. **110**, 100401 (2013).

[54] T. Graf, C. Felser, and S. S. Parkin, Progress in solid state chemistry **39**, 1 (2011).

[55] G. Liu, X. Dai, H. Liu, J. Chen, Y. Li, G. Xiao, and G. Wu, Phys. Rev. B **77**, 014424 (2008).

[56] H. Kandpal, G. Fecher, and C. Felser, J. Phys. D: Appl. Phys. **40**, 1507 (2007).

[57] Y. Feng et al., Phys. Rev. B **63**, 165109 (2001).

[58] T. Burch, T. Litrenta, and J. Budnick, Phys. Rev. Lett. **33**, 421 (1974).

[59] P. Kharel, Y. Huh, N. Al-Aqtash, V. Shah, R. F. Sabirianov, R. Skomski, and D. J. Sellmyer, J. Phys.: Condens. Matter **26**, 126001 (2014).

[60] H. Kurt, K. Rode, H. Tokuc, P. Stamenov, M. Venkatesan, and J. Coey, Appl. Phys. Lett. **101**, 232402 (2012).

[61] T. Gasi, A. K. Nayak, J. Winterlik, V. Ksenofontov, P. Adler, M. Nicklas, and C. Felser, Appl. Phys. Lett. **102**, 202402 (2013).

[62] Z. Liu, Y. Zhang, H. Zhang, X. Zhang, and X. Ma, Appl. Phys. Lett. **109** (2016).

[63] P. J. Webster, K. R. A. Ziebeck, S. L. Town, and M. S. Peak, Phil. Maga. B **49**, 295 (1984).

[64] G. Liu et al., Appl. Phys. Lett. **87**, 262504 (2005).

[65] G. D. Liu et al., Phys. Rev. B **74**, 054435 (2006).

[66] S. Barman and A. Chakrabarti, Phys. Rev. B **77**, 176401 (2008).

[67] S. Singh, S. Esakki Muthu, A. Senyshyn, P. Rajput, E. Suard, S. Arumugam, and S. Barman, Appl. Phys. Lett. **104**, 051905 (2014).

[68] S. Singh, M. Maniraj, S. W. DSouza, R. Ranjan, and S. R. Barman, Appl. Phys. Lett. **96** (2010).

[69] P. J. Brown, T. Kanomata, K. Neumann, K. U. Neumann, B. Ouladdiaf, A. Sheikh, and K. R. A. Ziebeck, J. Phys.: Condens. Matter **22**, 506001 (2010).

[70] K. Rode et al., Phys. Rev. B **87**, 184429 (2013).

[71] H. Kurt, K. Rode, M. Venkatesan, P. Stamenov, and J. M. D. Coey, Phys. Rev. B **83**, 020405 (2011).

[72] A. K. Nayak et al., Nature materials **14**, 679 (2015).

[73] M. Meinert, J.-M. Schmalhorst, C. Klewe, G. Reiss, E. Arenholz, T. Böhnert, and K. Nielsch, Phys. Rev. B **84**, 132405 (2011).

[74] Y. Zhang, G. Li, E. Liu, J. Chen, W. Wang, F. Meng, and G. Wu, Physica B: Condensed Matter **454**, 1 (2014).

[75] A. Chakrabarti and S. Barman, Appl. Phys. Lett. **94**, 161908 (2009).

[76] S. Paul and S. Ghosh, J. Phys.: Condens. Matter **23**, 206003 (2011).

[77] S. Paul and S. Ghosh, J. Appl. Phys. **110**, 063523 (2011).

[78] S. Paul, A. Kundu, B. Sanyal, and S. Ghosh, J. Appl. Phys. **116**, 133903 (2014).

[79] H. Xuan, Q. Cao, C. Zhang, S. Ma, S. Chen, D. Wang, and Y. Du, Appl. Phys. Lett. **96**, 202502 (2010).

[80] L. Ma, W. Wang, J. Lu, J. Li, C. Zhen, D. Hou, and G. Wu, Appl. Phys. Lett. **99**, 182507 (2011).

[81] H. Xuan, S. Ma, Q. Cao, D. Wang, and Y. Du, J. Alloys Compds. **509**, 5761 (2011).

[82] L. Ma et al., J. Appl. Phys. **112**, 083902 (2012).

[83] J. Sharma and K. Suresh, Appl. Phys. Lett. **106**, 072405 (2015).

[84] D. Lobo, K. Priolkar, A. Koide, and S. Emura, J. Appl. Phys. **121**, 053902 (2017).

[85] L. Wollmann, S. Chadov, J. Kübler, and C. Felser, Phys. Rev. B **90**, 214420 (2014).

[86] L. Wollmann, S. Chadov, J. Kübler, and C. Felser, Phys. Rev. B **92**, 064417 (2015).

[87] P. Hohenberg and W. Kohn, Phys. Rev. **136**, B864 (1964).

[88] W. Kohn and L. J. Sham, Phys. Rev. **140**, A1133 (1965).

[89] R. M. Martin, *Electronic structure: basic theory and practical methods*, Cambridge university press, United Kindom, 2004.

[90] J. Korringa, Physica **13**, 392 (1947).

[91] W. Kohn and N. Rostoker, Phys. Rev. **94**, 1111 (1954).

[92] D. J. Singh and L. Nordstrom, *Planewaves, Pseudopotentials, and the LAPW method*, Springer Science & Business Media, 2006.

[93] P. Blaha, K. Schwarz, P. Sorantin, and S. Trickey, Computer Physics Communications **59**, 399 (1990).

[94] J. C. Slater, Phys. Rev. **51**, 846 (1937).

[95] J. Slater, Advances in quantum chemistry **1**, 35 (1964).

[96] J. Kubler, K.-H. Hock, J. Sticht, and A. Williams, Journal of Physics F: Metal Physics **18**, 469 (1988).

[97] L. Sandratskii, Advances in Physics **47**, 91 (1998).

[98] L. Nordström and D. J. Singh, Phys. Rev. Lett. **76**, 4420 (1996).

[99] D. Hobbs, G. Kresse, and J. Hafner, Phys. Rev. B **62**, 11556 (2000).

[100] S. Y. Savrasov, Phys. Rev. B **54**, 16470 (1996).

[101] S. Baroni, S. De Gironcoli, A. Dal Corso, and P. Giannozzi, Reviews of Modern Physics **73**, 515 (2001).

[102] I. Turek, V. Drchal, J. Kudrnovskỳ, M. Sob, and P. Weinberger, *Electronic structure of disordered alloys, surfaces and interfaces*, Springer Science & Business Media, 2013.

[103] R. McCormack and D. De Fontaine, Phy. Rev. B **54**, 9746 (1996).

[104] Q.-M. Hu, C.-M. Li, R. Yang, S. E. Kulkova, D. I. Bazhanov, B. Johansson, and L. Vitos, Phys. Rev. B **79**, 144112 (2009).

[105] C.-M. Li, H.-B. Luo, Q.-M. Hu, R. Yang, B. Johansson, and L. Vitos, Phys. Rev. B **82**, 024201 (2010).

[106] C.-M. Li, H.-B. Luo, Q.-M. Hu, R. Yang, B. Johansson, and L. Vitos, Phys. Rev. B **84**, 024206 (2011).

[107] E. Krén and G. Kádár, Solid State Communications **8**, 1653 (1970).

[108] D. Zhang, B. Yan, S.-C. Wu, J. Kübler, G. Kreiner, S. S. Parkin, and C. Felser, J. Phys.: Condens. Matter **25**, 206006 (2013).

[109] M. Born and R. Oppenheimer, Annalen der Physik **389**, 457 (1927).

[110] L. H. Thomas, The calculation of atomic fields, in *Mathematical Proceedings of the Cambridge Philosophical Society*, volume 23, pages 542–548, Cambridge University Press, 1927.

[111] E. Fermi, Rend. Accad. Naz. Lincei **6**, 32 (1927).

[112] D. R. Hartree, The wave mechanics of an atom with a non-coulomb central field. part i. theory and methods, in *Mathematical Proceedings of the Cambridge Philosophical Society*, volume 24, pages 89–110, Cambridge University Press, 1928.

[113] V. Fock, Zeitschrift für Physik A Hadrons and Nuclei **61**, 126 (1930).

[114] J. P. Perdew, P. Ziesche, and H. Eschrig, *Electronic structure of solids 91*, volume 11, Akademie Verlag, Berlin, 1991.

[115] J. P. Perdew, K. Burke, and M. Ernzerhof, Physical review letters **77**, 3865 (1996).

[116] J. P. Perdew and W. Yue, Phys. Rev. B **33**, 8800 (1986).

[117] D. Vanderbilt, Phys. Rev. B **41**, 7892 (1990).

[118] K. Laasonen, R. Car, C. Lee, and D. Vanderbilt, Phys. Rev. B **43**, 6796 (1991).

[119] K. Laasonen, A. Pasquarello, R. Car, C. Lee, and D. Vanderbilt, Phys. Rev. B **47**, 10142 (1993).

[120] P. E. Blöchl, Phys. Rev. B **50**, 17953 (1994).

[121] G. Kresse and J. Hafner, Phys. Rev. B **47**, 558 (1993).

[122] G. Kresse and J. Hafner, Phys. Rev. B **49**, 14251 (1994).

[123] G. Kresse and J. Furthmüller, Physical review B **54**, 11169 (1996).

[124] S. Cottenier, Instituut voor Kern-en Stralingsfysica, KU Leuven, Belgium **4**, 41 (2002).

[125] G. Kresse et al., *Vienna ab-initio simulation package (VASP)*, Vienna University, Vienna, Austria, 2001.

[126] H. Ebert et al., *The Munich SPR-KKR package, version 6.3*, University of Munich, Munich, Germany, 2012.

[127] P. Soven, Phys. Rev. **156**, 809 (1967).

[128] D. W. Taylor, Phys. Rev. **156**, 1017 (1967).

[129] B. L. Gyorffy, Phys. Rev. B **5**, 2382 (1972).

[130] L. Vitos, *Computational quantum mechanics for materials engineers: the EMTO method and applications*, Springer Science & Business Media, 2007.

[131] F. Murnaghan, Proc. Natl. Acad. Sci. USA **30**, 244 (1944).

[132] G. Grimvall, *Thermophysical properties of materials*, Elsevier, 1999.
[133] E. Ziambaras and E. Schröder, Phys. Rev. B **68**, 064112 (2003).
[134] S. O. Kart and T. Cagın, J. Alloys Compds. **508**, 177 (2010).
[135] W. Voigt, Ann. Phys. (NY) **274**, 573 (1889).
[136] A. Reuss, Z. Angew. Math. Mech. **9**, 49 (1929).
[137] R. Hill, Proceedings of the Physical Society. Section A **65**, 349 (1952).
[138] R. Hill, Journal of the Mechanics and Physics of Solids **11**, 357 (1963).
[139] S. Pugh, Philo. Mag. **45**, 823 (1954).
[140] H. Niu, X. Chen, P. Liu, W. Xing, X. Cheng, D. Li, and Y. Li, Sci. Rep. **2**, 718 (2012).
[141] H. Ebert, D. Koedderitzsch, and J. Minar, Rep. Prog. Phys. **74**, 096501 (2011).
[142] A. Liechtenstein, M. Katsnelson, V. Antropov, and V. Gubanov, J. Magn. Magn. Mater. **67**, 65 (1987).
[143] M. Methfessel and J. Kubler, Journal of Physics F: Metal Physics **12**, 141 (1982).
[144] E. Şaşıoğlu, L. M. Sandratskii, and P. Bruno, Phys. Rev. B **70**, 024427 (2004).
[145] D. Landau and K. Binder, in *A Guide to Monte Carlo simulations in Statistical Physics*, Cambridge University Press, 2000.
[146] E. Şaşıoğlu, L. M. Sandratskii, P. Bruno, and I. Galanakis, Phys. Rev. B **72**, 184415 (2005).
[147] V. V. Sokolovskiy, V. D. Buchelnikov, M. A. Zagrebin, P. Entel, S. Sahoo, and M. Ogura, Phys. Rev. B **86**, 134418 (2012).
[148] K. Binder et al., Computers in Physics **7**, 156 (1993).
[149] N. Metropolis, A. W. Rosenbluth, M. N. Rosenbluth, A. H. Teller, and E. Teller, J. Chem. Phys. **21**, 1087 (1953).
[150] N. Singh, E. Dogan, I. Karaman, and R. Arróyave, Phys. Rev. B **84**, 184201 (2011).
[151] W. Frank, C. Elsässer, and M. Fähnle, Phys. Rev. Lett. **74**, 1791 (1995).
[152] G. Kresse, J. Furthmüller, and J. Hafner, EPL (Europhysics Letters) **32**, 729 (1995).
[153] K. Parlinski, Calculation of phonon dispersion curves by the direct method, in *AIP Conference Proceedings*, volume 479, pages 121–126, AIP, 1999.
[154] D. Alfe, Computer Physics Communications **180**, 2622 (2009).
[155] D. Alfè, G. D. Price, and M. J. Gillan, Phys. Rev. B **64**, 045123 (2001).
[156] V. A. Chernenko, C. Seguí, E. Cesari, J. Pons, and V. V. Kokorin, Phys. Rev. B **57**, 2659 (1998).
[157] P. Brown, J. Crangle, T. Kanomata, M. Matsumoto, K. Neumann, B. Ouladdiaf, and K. Ziebeck, J. Phys.: Condens. Matter **14**, 10159 (2002).
[158] J. Pons, R. Santamarta, V. A. Chernenko, and E. Cesari, J. Appl. Phys. **97**, 083516 (2005).
[159] L. Righi, F. Albertini, L. Pareti, A. Paoluzi, and G. Calestani, Acta Mater. **55**, 5237 (2007).
[160] L. Righi et al., Acta Mater. **56**, 4529 (2008).
[161] S. Singh, V. Petricek, P. Rajput, A. H. Hill, E. Suard, S. R. Barman, and D. Pandey, Phys. Rev. B **90**, 014109 (2014).

[162] S. Mariager, T. Huber, and G. Ingold, Acta Mater. **66**, 192 (2014).

[163] L. Straka et al., Acta Mater. **59**, 7450 (2011).

[164] A. Diestel, A. Backen, U. K. Rößler, L. Schultz, and S. Fähler, Appl. Phys. Lett. **99**, 092512 (2011).

[165] P. Müllner, V. Chernenko, and G. Kostorz, J. Magn. Magn. Mater. **26**, 325 (2003).

[166] S. Kaufmann, U. K. Rößler, O. Heczko, M. Wuttig, J. Buschbeck, L. Schultz, and S. Fähler, Phys. Rev. Lett. **104**, 145702 (2010).

[167] P. Müllner and A. H. King, Acta Mater. **58**, 5242 (2010).

[168] Y. Lee, J. Y. Rhee, and B. N. Harmon, Phys. Rev. B **66**, 054424 (2002).

[169] C. Bungaro, K. M. Rabe, and A. Dal Corso, Phys. Rev. B **68**, 134104 (2003).

[170] A. Khachaturyan, S. Shapiro, and S. Semenovskaya, Phys. Rev. B. **43**, 10832 (1991).

[171] J. Pons, V. Chernenko, R. Santamarta, and E. Cesari, Acta Materialia **48**, 3027 (2000).

[172] S. Kaufmann et al., New J. Phys. **13**, 053029 (2011).

[173] R. Niemann, U. K. Rößler, M. E. Gruner, O. Heczko, L. Schultz, and S. Fähler, Adv. Eng. Mater. **14**, 562 (2012).

[174] B. Dutta, A. Çakır, C. Giacobbe, A. Al-Zubi, T. Hickel, M. Acet, and J. Neugebauer, Phys. Rev. Lett. **116**, 025503 (2016).

[175] M. Zelenỳ, L. Straka, A. Sozinov, and O. Heczko, Phys. Rev. B **94**, 224108 (2016).

[176] M. E. Gruner, R. Niemann, P. Entel, R. Pentcheva, U. K. Rössler, K. Nielsch, and S. Fähler, arXiv:1701.01562 (2017).

[177] G. Kresse and J. Furthmüller, Phys. Rev. B **54**, 11169 (1996).

[178] G. Kresse and D. Joubert, Phys. Rev. B **59**, 1758 (1999).

[179] J. P. Perdew, K. Burke, and M. Ernzerhof, Phys. Rev. Lett. **77**, 3865 (1996).

[180] M. Methfessel and A. T. Paxton, Phys. Rev. B **40**, 3616 (1989).

[181] P. Entel, V. D. Buchelnikov, M. E. Gruner, A. Hucht, V. V. Khovailo, S. K. Nayak, and A. T. Zayak, Mater. Sci. Forum **583**, 21 (2008).

[182] M. Siewert et al., Adv. Eng. Mater. **14**, 530 (2012).

[183] T. Roy and A. Chakrabarti, J. Magn. Magn. Mater. **423**, 395 (2017).

[184] A. T. Zayak, P. Entel, J. Enkovaara, A. Ayuela, and R. M. Nieminen, J. Phys.: Condens. Matter **15**, 159 (2003).

[185] A. Zayak, W. A. Adeagbo, P. Entel, and V. D. Buchelnikov, Phase Transitions **78**, 259 (2005).

[186] L. Righi et al., J. Solid State Chem. **179**, 3525 (2006).

[187] H. Luo, C. Li, Q. Hu, S. Kulkova, B. Johansson, L. Vitos, and R. Yang, Acta Mater. **59**, 5938 (2011).

[188] A. T. Zayak and P. Entel, Mater. Sci. Eng. A **378**, 419 (2004).

[189] A. T. Zayak, P. Entel, K. M. Rabe, W. A. Adeagbo, and M. Acet, Phys. Rev. B **72**, 0541113 (2005).

[190] P. Entel et al., J. Phys. D: Appl. Phys. **39**, 865 (2006).

[191] T. Hickel, M. Uijttewaal, B. Grabowski, and J. Neugebauer, Mater. Res. Soc. Symp. Proc. **1050E**, 1050 (2008).

[192] S. O. Kart, M. Uludoğan, I. Karaman, and T. Çağin, phys. stat. sol. (a) **205**, 1026 (2008).

[193] T. Hickel, M. Uijttewaal, A. Al-Zubi, B. Dutta, B. Grabowski, and J. Neugebauer, Adv. Eng. Mater. **14**, 547 (2012).

[194] A. Çakir, L. Righi, F. Albertini, M. Acet, M. Farle, and S. Aktürk, J. Appl. Phys. **114**, 183912 (2013).

[195] N. Xu et al., Appl. Phys. Lett. **100**, 084106 (2012).

[196] J. Bai, N. Xu, J.-M. Raulot, C. Esling, X. Zhao, and L. Zuo, Int. J. Quant. Chem. **113**, 847 (2013).

[197] M. E. Gruner, S. Fähler, and P. Entel, phys. stat. sol. (b) **251**, 2067 (2014).

[198] S. Singh, J. Bednarcik, S. R. Barman, C. Felser, and D. Pandey, Phys. Rev. B **92**, 054112 (2015).

[199] V. Chernenko, M. Chmielus, and P. Müllner, Appl. Phys. Lett. **95**, 104103 (2009).

[200] A. Sozinov, A.A. Likhachev, N. Lanska, O. Söderberg, K. Koho, K. Ullakko, and V.K. Lindroos, J. Phys. IV France **115**, 121 (2004).

[201] V. Soolshenko, A. Lanska, and K. Ullakko, J. Phys. IV, France **112**, 947 (2003).

[202] A. Sozinov, N. Lanska, A. Soroka, and W. Zou, Appl. Phys. Lett. **102**, 021902 (2013).

[203] J. Zhang, W. Cai, Z. Gao, and J. H. Sui, Scr. Mater. **58**, 798 (2008).

[204] W. Cai, J. Zhang, Z. Y. Gao, and J. H. Sui, Appl. Phys. Lett. **92**, 252502 (2008).

[205] S. W. DŚouza, T. Roy, S. R. Barman, and A. Chakrabarti, J. Phys.: Condens. Matter **26**, 506001 (2014).

[206] D. M. Schaefer, I. T. Neckel, I. L. Graff, J. Varalda, W.-H. Schreiner, and D. H. Mosca, J. Phys. D: Appl. Phys. **49**, 465002 (2016).

[207] M. A. Uijttewaal, T. Hickel, J. Neugebauer, M. E. Gruner, and P. Entel, Phys. Rev. Lett. **102**, 035702 (2009).

[208] S. R. Barman, S. Banik, A. K. Shukla, C. Kamal, and A. Chakrabarti, EPL **80**, 57002 (2007).

[209] C. G. Blum et al., Appl. Phys. Lett. **98**, 252501 (2011).

[210] B. Ahuja, G. Ahmed, S. Banik, M. Itou, Y. Sakurai, and S. Barman, Phys. Rev. B **79**, 214403 (2009).

[211] A. T. Zayak, P. Entel, J. Enkovaara, A. Ayuela, and R. M. Nieminen, Phys. Rev. B **68**, 132402 (2003).

[212] S. Ener et al., Phys. Rev. B **86**, 144305 (2012).

[213] S. Paul, B. Sanyal, and S. Ghosh, J. Phys.: Condens. Matter **27**, 035401 (2015).

[214] C. M. Varma and W. Weber, Phys. Rev. Lett. **39**, 1094 (1977).

[215] C. M. Varma and W. Weber, Phys. Rev. B **19**, 6142 (1979).

[216] W. E. Pickett and P. B. Allen, Phys. Rev. B **16**, 3127 (1977).

[217] M.-H. Whangbo, E. Canadell, P. Foury, and J.-P. Pouget, Science **252**, 96 (1991).

[218] M. D. Johannes and I. I. Mazin, Phys. Rev. B **77**, 165135 (2008).

[219] C. P. Opeil et al., Phys. Rev. Lett. **100**, 165703 (2008).

[220] P. Entel, M. E. Gruner, and A. Hucht, Mater. Res. Soc. Symp. Proc. **1050E**, 1050

(2008).
[221] T. D. Haynes et al., New J. Phys. **14**, 035020 (2012).
[222] P. Entel et al., Phase diagrams of conventional and inverse functional magnetic heusler alloys: New theoretical and experimental investigations, in *Disorder and Strain-Induced Complexity in Functional Materials*, edited by T. Kakeshita, T. Fukuda, A. Saxena, and A. Planes, volume 148 of *Springer Series in Materials Science*, page 19, Springer, Berlin, Heidelberg, 2012.
[223] M. I. Katsnelson, I. I. Naumov, and A. V. Trefilov, Phase Transitions **49**, 143 (1994).
[224] O. I. Velikokhatnyi and I. I. Naumov, Fiz. Tverd. Tela **41**, 684 (1999), [Physics of the Solid State **41**, 617 (1999)].
[225] R. J. Gooding and J. A. Krumhansl, Phys. Rev. B **38**, 1695 (1988).
[226] R. J. Gooding and J. A. Krumhansl, Phys. Rev. B **39**, 1535 (1989).
[227] A. Dal Corso, A. Pasquarello, and A. Baldereschi, Phys. Rev. B **56**, R11369 (1997).
[228] H. Eschrig, phys. stat. sol. (b) **56**, 197 (1973).
[229] M. E. Gruner, Habilitation, Universität Duisburg-Essen (2012).
[230] R. C. Pond, B. Muntifering, and P. Müllner, Acta Mater. **60**, 3976 (2012).
[231] D. Soto et al., Phys. Rev. B **77**, 184103 (2008).
[232] T. Kanomata et al., Phys. Rev. B **80**, 214402 (2009).
[233] T. Kanomata, T. Nozawa, D. Kikuchi, H. Nishihara, K. Koyama, and K. Watanabe, International Journal of Applied Electromagnetics and Mechanics **21**, 151 (2005).
[234] A. Gomes, M. Khan, S. Stadler, N. Ali, I. Dubenko, A. Takeuchi, and A. Guimarães, J. Appl. Phys. **99**, 08Q106 (2006).
[235] M. Khan, I. Dubenko, S. Stadler, and N. Ali, J. Appl. Phys. **97**, 10M304 (2005).
[236] T. Kanomata et al., Metals **3**, 114 (2013).
[237] D. Soto-Parra et al., Philosophical Magazine **90**, 2771 (2010).
[238] T. Kanomata et al., Phys. Rev. B **85**, 134421 (2012).
[239] H. Luo et al., J. Appl. Phys. **107**, 013905 (2010).
[240] L. Ma et al., Phys. Rev. B **84**, 224404 (2011).
[241] A. Chakrabarti, M. Siewert, T. Roy, K. Mondal, A. Banerjee, M. E. Gruner, and P. Entel, Phys. Rev. B **88**, 174116 (2013).
[242] E. C. Do, Y.-H. Shin, and B.-J. Lee, Calphad **32**, 82 (2008).
[243] V. Ramamurthy and S. Rajendraprasad, J. Phys. Chem. Solids **47**, 1109 (1986).
[244] D. Winder and C. S. Smith, J. Phys. Chem. Solids **4**, 128 (1958).
[245] M. Zelenỳ, A. Sozinov, L. Straka, T. Björkman, and R. M. Nieminen, Phys. Rev. B **89**, 184103 (2014).
[246] S. Ghosh, L. Vitos, and B. Sanyal, Physica B: Condensed Matter **406**, 2240 (2011).
[247] S. R. Barman et al., Phys. Rev. B **78**, 134406 (2008).
[248] V. Alijani, J. Winterlik, G. H. Fecher, S. S. Naghavi, and C. Felser, Phys. Rev. B **83**, 184428 (2011).
[249] V. Buchelnikov, V. Sokolovskiy, M. Zagrebin, M. Tufatullina, and P. Entel, J. Phys. D: Appl. Phys. **48**, 164005 (2015).
[250] V. V. Sokolovskiy, P. Entel, V. D. Buchelnikov, and M. E. Gruner, Phys. Rev. B

91, 220409 (2015).

[251] R. Helmholdt and K. Buschow, Journal of the Less Common Metals **128**, 167 (1987).

[252] S. Paul, A. Kundu, B. Sanyal, and S. Ghosh, J. Phys.: Condens. Matt. **25**, 236005 (2013).

[253] H. Luo et al., J. Appl. Phys. **103**, 083908 (2008).

[254] T. Roy, M. Gruner, P. Entel, and A. Chakrabarti, J. Alloys Compds. **632**, 822 (2015).

[255] T. Roy, D. Pandey, and A. Chakrabarti, Phys. Rev. B. **93**, 184102 (2016).

[256] D. Pettifor, Mater. Sci. Tech. **8**, 345 (1992).

[257] K. Minakuchi, R. Umetsu, K. Kobayashi, M. Nagasako, and R. Kainuma, J. Alloys Compds. **645**, 577 (2015).

[258] J. C. Slater, Phys. Rev. **49**, 537 (1936).

[259] L. Pauling, Phys. Rev. **54**, 899 (1938).

[260] S. Sanvito et al., Science Advances **3**, e1602241 (2017).

[261] D. Kikuchi, T. Kanomata, Y. Yamaguchi, H. Nishihara, K. Koyama, and K. Watanabe, J. Alloys Compds. **383**, 184 (2004).

[262] S. Khmelevskyi, A. V. Ruban, and P. Mohn, Phys. Rev. B **93**, 184404 (2016).

[263] A. Niesen, C. Sterwerf, M. Glas, J. M. Schmalhorst, and G. Reiss, IEEE Transactions on Magnetics **52**, 1 (2016).

[264] D. Betto et al., Phys. Rev. B **96**, 024408 (2017).

[265] A. Kalache, A. Markou, S. Selle, T. Hche, R. Sahoo, G. H. Fecher, and C. Felser, APL Materials **5**, 096102 (2017).

[266] S. O. Kart and T. Cagn, J. Alloys Compds. **508**, 177 (2010).

[267] C. Zener, Phys. Rev. **71**, 846 (1947).

[268] N. Lakshmi, A. Pandey, and K. Venugopalan, Bulletin of Materials Science **25**, 309 (2002).

[269] T. Krenke, M. Acet, E. F. Wassermann, X. Moya, L. Mañosa, and A. Planes, Phys. Rev. B **72**, 014412 (2005).

[270] T. Krenke, M. Acet, E. F. Wassermann, X. Moya, L. Mañosa, and A. Planes, Phys. Rev. B **73**, 174413 (2006).

[271] X. Moya et al., Phys. Rev. B **74**, 024109 (2006).

[272] T. Kanomata et al., J. Magn. Magn. Mater. **321**, 773 (2009), Proceedings of the Forth Moscow International Symposium on Magnetism.

[273] R. Coll, L. Escoda, J. Saurina, J. L. Sánchez-Llamazares, B. Hernando, and J. Sunol, Journal of thermal analysis and calorimetry **99**, 905 (2010).

[274] H. Xuan, Y. Zhang, H. Li, P. Han, D. Wang, and Y. Du, physica status solidi (a) **212**, 680 (2014).

[275] H. Tian, J. Lu, L. Ma, H. Shi, H. Yang, G. Wu, and J. Li, J. Appl. Phys. **112**, 033904 (2012).

[276] A. Ghosh and K. Mandal, J. Appl. Phys. **117**, 093909 (2015).

[277] M. K. Ray, K. Bagani, P. Mukhopadhyay, and S. Banerjee, EPL (Europhysics Letters) **109**, 47006 (2015).

[278] T. Fichtner et al., Metals **5**, 484 (2015).
[279] D. Zhao et al., Intermetallics **70**, 68 (2016).
[280] Z. Wu, Z. Liu, H. Yang, Y. Liu, and G. Wu, J. Phys. D: Appl. Phys. **44**, 385403 (2011).
[281] C.-M. Li, Q.-M. Hu, R. Yang, B. Johansson, and L. Vitos, Phys. Rev. B **88**, 014109 (2013).
[282] C.-M. Li, H.-B. Luo, Q.-M. Hu, R. Yang, B. Johansson, and L. Vitos, Phys. Rev. B **86**, 214205 (2012).
[283] Z. Wu, Z. Liu, H. Yang, Y. Liu, and G. Wu, Appl. Phys. Lett. **98**, 061904 (2011).
[284] H. Xuan, Y. Zheng, S. Ma, Q. Cao, D. Wang, and Y. Du, J. Appl. Phys. **108**, 103920 (2010).
[285] C. D. Gelatt, A. R. Williams, and V. L. Moruzzi, Phys. Rev. B **27**, 2005 (1983).
[286] Q. M. Hu, R. Yang, D. S. Xu, Y. L. Hao, D. Li, and W. T. Wu, Phys. Rev. B **68**, 054102 (2003).

List of Publications

1. Souvik Paul, **Ashis Kundu**, Biplab Sanyal, Subhradip Ghosh, *Anti-site disorder and improved functionality of Mn_2NiX (X= Al, Ga, In, Sn) inverse Heusler alloys*, Journal of Applied Physics **116**, 133903 (2014)

2. Bhargab Deka, **Ashis Kundu**, Subhradip Ghosh, A Srinivasan, *Experimental and ab initio studies on sub-lattice ordering and magnetism in $Co_2Fe(Ge_{1-x}Si_x)$ alloys*, Journal of Applied Physics **118**, 133906 (2015)

3. Bhargab Deka, **Ashis Kundu**, Subhradip Ghosh, A Srinivasan, *Effect of electron-electron correlation and site disorder on the magnetic moment and half-metallicity of $Co_2Fe(Ga_{1-x}Si_x)$ alloys*, Materials Chemistry and Physics **177**, 564-569 (2016)

4. **Ashis Kundu**, Srikrishna Ghosh, Rudra Banerjee, Subhradip Ghosh, Biplab Sanyal, *New quaternary half-metallic ferromagnets with large Curie temperatures*, Scientific Reports **7**, 1803 (2017)

5. **Ashis Kundu**, Markus E Gruner, Mario Siewert, Alfred Hucht, Peter Entel, Subhradip Ghosh, *Interplay of phase sequence and electronic structure in the modulated martensites of Mn_2NiGa from first-principles calculations*, Physical Review B **96**, 064107 (2017)*

6. **Ashis Kundu**, Sheuly Ghosh, Subhradip Ghosh, *Effect of Fe and Co substitution on the martensitic stability and the elastic, electronic, and magnetic properties of Mn_2NiGa: Insights from ab initio calculations*, Physical Review B **96**, 174107 (2017)*

Publications marked with * are included in the thesis

7. **Ashis Kundu**, Subhradip Ghosh, *Site occupancy, composition and magnetic structure dependencies of martensitic transformation in* $Mn_2Ni_{1+x}Sn_{1-x}$, J. Phys.: Condens. Matter **30**, 015401 (2018)*

8. **Ashis Kundu**, Subhradip Ghosh, *First principles study of the structural phase stability and magnetic order in various structural phases of* Mn_2FeGa, Intermetallics **93**, 209-216 (2018)*

National Schools/workshops/Conferences attended

1. Asia-Sweden meeting on *understanding functional material from lattice dynamics*, January 9-11 (2014), **IIT Guwagati**, Guwahati, Assam, India.

2. DST-SERC School on *Advanced Functional Magnetic Materials*, February 3-21, (2014), **Goa University**, Goa, India.

3. National conference on *Transport Properties in Low Dimensional Systems: Experiment and Simulation*, (2014), **IASST**, Guwahati, India.

4. A school on *Materials and Processes for Applications in Energy and Environment*, January 15-18, (2015), **JNCASR**, Bangalore, India.

5. *8th USPEX Workshop*, January 20-24, (2015), **Shiv Nadar University**, U.P., India.

6. *Functional Materials for Today and Tomorrow*, October 28-30, (2015), **HHI**, Kolkata, India.

International Visits/Schools attended

1. Visiting Researcher, September 1, (2015) - October 15, (2015), **Department of Physics and Astronomy, Uppsala University**, Uppsala, Sweden.

2. ViCoM Winter School on *Magnetism*, February 20-24, (2017), **Vienna University of Technology**, Vienna, Austria.